

AD-A192 507

1

DTIC FILE COPY

TEC REPORT R-87-015

RESEARCH AND DEVELOPMENT PROGRAM
TO DEVELOP A NONDESTRUCTIVE EVALUATION
INSTRUMENT (X-RAY DIFFRACTION) FOR MEASURING
RESIDUAL STRESSES IN A WIDE RANGE OF
NAVAL AVIATION MATERIAL
SBIR PHASE II - FINAL REPORT

DTIC
SELECTED
MAR 11 1988
S D

DISTRIBUTION STATEMENT A

Approved for public release;
Distribution Unlimited



TECHNOLOGY FOR ENERGY CORPORATION

88 3 09 111

1

TEC REPORT R-87-015

RESEARCH AND DEVELOPMENT PROGRAM
TO DEVELOP A NONDESTRUCTIVE EVALUATION
INSTRUMENT (X-RAY DIFFRACTION) FOR MEASURING
RESIDUAL STRESSES IN A WIDE RANGE OF
NAVAL AVIATION MATERIAL
SBIR PHASE II - FINAL REPORT

DTIC
ELECTE
MAR 11 1988
S D

Prepared For:

Department of the Navy
Naval Air Systems Command
Air 310P
Washington, DC 20361

Contract No. N00019-85-C-0419

DISTRIBUTION STATEMENT A

Approved for public release;
Distribution Unlimited

Contractor:

Technology for Energy Corporation
One Energy Center
Lexington Drive
Knoxville, Tennessee 37932

R. D. Brenner, Project Manager
E. B. Pardue, Principal Investigator

88 3 09 111

B414
329

SECURITY CLASSIFICATION OF THIS PAGE

REPORT DOCUMENTATION PAGE

1a. REPORT SECURITY CLASSIFICATION UNCLASSIFIED		1b. RESTRICTIVE MARKINGS	
2a. SECURITY CLASSIFICATION AUTHORITY		3. DISTRIBUTION/AVAILABILITY OF REPORT Approved for Public Release, Distribution is Unlimited.	
2b. DECLASSIFICATION/DOWNGRADING SCHEDULE		4. PERFORMING ORGANIZATION REPORT NUMBER(S) TEC Report R-87-015	
6a. NAME OF PERFORMING ORGANIZATION Technology for Energy Corporation		6b. OFFICE SYMBOL (If applicable)	7a. NAME OF MONITORING ORGANIZATION Naval Air Systems Command
6c. ADDRESS (City, State, and ZIP Code) One Energy Center Lexington Drive Knoxville, Tennessee 37932		7b. ADDRESS (City, State, and ZIP Code) AIR-931A Naval Air Systems Command Washington, DC 20361	
8a. NAME OF FUNDING/SPONSORING ORGANIZATION Small Business Innovation Research	8b. OFFICE SYMBOL (If applicable)	9. PROCUREMENT INSTRUMENT IDENTIFICATION NUMBER N00019-85-C-0419	
8c. ADDRESS (City, State, and ZIP Code) AIR-9303C Naval Air Systems Command Washington, DC 20361		10. SOURCE OF FUNDING NUMBERS	
		PROGRAM ELEMENT NO.	PROJECT NO.
		TASK NO.	WORK UNIT ACCESSION NO.
11. TITLE (Include Security Classification) Research and Development Program to develop a nondestructive evaluation instrument (X-Ray diffraction) for measuring residual stresses in a wide range of Naval Aviation Material (Phase II) (Unclassified)			
12. PERSONAL AUTHOR(S) Brenner, R. D.; Pardue, E. B.			
13a. TYPE OF REPORT Final	13b. TIME COVERED FROM Mar 86 TO 4/3/87	14. DATE OF REPORT (Year, Month, Day) 1987, April 03	15. PAGE COUNT 137
16. SUPPLEMENTARY NOTATION			
17. COSATI CODES		18. SUBJECT TERMS (Continue on reverse if necessary and identify by block number)	
FIELD	GROUP	residual stresses,	
1106		x-ray ←	
19. ABSTRACT (Continue on reverse if necessary and identify by block number)			
<p>In the Phase II program a prototype stress analysis unit was designed, constructed, tested and delivered to the Navy that was smaller, lighter and easier to use than TEC's existing design. Also large number of residual stress measurements were made on components and materials of interest to Naval Aviation.</p> <p style="text-align: right;"><i>keyed</i></p>			
20. DISTRIBUTION/AVAILABILITY OF ABSTRACT <input checked="" type="checkbox"/> UNCLASSIFIED/UNLIMITED <input type="checkbox"/> SAME AS RPT. <input type="checkbox"/> DTIC USERS		21. ABSTRACT SECURITY CLASSIFICATION	
22a. NAME OF RESPONSIBLE INDIVIDUAL James E. Muller, Jr.		22b. TELEPHONE (Include Area Code) (202) 692-6025	22c. OFFICE SYMBOL AIR-5304

TABLE OF CONTENTS

<u>Section</u>	<u>Page</u>
LIST OF FIGURES	iv
LIST OF TABLES	vi
ACKNOWLEDGMENTS	vii
1.0 Summary	1-1
1.1 Introduction	1-1
1.2 Program Objectives	1-3
1.3 Results	1-5
1.3.1 Task 1 - Prototype Cart	1-5
1.3.2 Task 2 - Residual Stress Measurements	1-5
1.3.3 Task 3 - Analytical Systems	1-7
1.3.4 Task 4 - Communications Link	1-7
2.0 Task 1 - Prototype Cart	2-1
2.1 Size Reduction	2-1
2.2 Weight Reduction	2-4
2.3 Other Design Improvements	2-7
2.3.1 CRT	2-7
2.3.2 Relocation of Printer	2-8
2.3.3 Power Distribution	2-8
2.3.4 Miscellaneous Changes	2-8
3.0 Task 2 - Residual Stress Measurements	3-1
3.1 F-14 Landing Gear	3-1
3.1.1 Preparation of Measurement Procedure	3-1
3.1.2 Service History	3-3
3.1.3 Results	3-3
3.1.4 Conclusions	3-12
3.2 Bearing Raceway Grinding	3-14
3.2.1 Introduction	3-14
3.2.2 Measurements	3-14
3.2.3 Results and Discussion	3-19
3.2.3.1 Inner Ring Raceways	3-19
3.2.3.2 Outer Ring Raceways (J-79 Only)	3-21
3.2.3.3 Comparison to Phase I Results	3-26
3.2.3.4 Evaluation of the Effects of Etching	3-27
3.2.4 Conclusions	3-31
3.3 Compressor and Fan Blades	3-33
3.3.1 Blade Description and Measurement	3-33
3.3.2 Results and Discussion	3-33
3.3.3 Conclusions	3-41
3.4 P-3 Propeller Hub Measurements	3-42
3.4.1 Introduction	3-42
3.4.2 Results	3-42
3.4.3 Conclusions	3-46

3.5	Nickel-Plating Study	3-47
3.5.1	Study of Nickel-Plating Residual Stress Measurements	3-47
3.5.1.1	Introduction	3-47
3.5.1.2	Flat Plate Sample	3-48
	Hard Plating	3-48
	Soft Plating	3-56
3.5.1.3	Rotated Flat Plate Sample	3-57
3.5.1.4	Cr KB Measurements	3-63
	Flat Plate	3-63
	Camshaft	3-63
3.5.2	Conclusions	3-66
3.5.3	Nickel Plated Fatigue Samples	3-70
3.5.3.1	Introduction	3-70
3.5.3.2	Measurements	3-72
3.5.3.3	Results and Discussion	3-72
3.5.4	Conclusions	3-85
4.0	Task Three - Analytical Systems	4-1
4.1	The Effect of Focusing Errors and Other Sample Misalignments on the Accuracy of Residual Stress as Determined by X-Ray Diffraction	4-1
4.1.1	Introduction	4-1
4.1.2	Flat Sample	4-2
4.1.3	Curved Sample	4-12
4.1.4	Conclusions	4-15
4.2	Practical Applications of the Analytical Study of Focusing Errors	4-16
5.0	Task Four - Communications Link	5-1
5.1	Objectives	5-1
5.2	Results	5-1
5.3	Discussion	5-1
5.4	Communication Package Operating Guide	5-6
5.4.1	DEC RT-11 Communications Package	5-6



Accession For	
NTIS CRA&I	<input checked="" type="checkbox"/>
DTIC TAB	<input type="checkbox"/>
Unannounced	<input type="checkbox"/>
Justification	
By _____	
Date: _____	
Approved by _____	
Dist	Special
A-1	

LIST OF FIGURES

<u>Figure</u>		<u>Page</u>
1-1	Photograph of Deliverable Prototype Unit	1-2
2-1	Prototype Cart Design Dimensions	2-2
2-2	Original Cart Design Dimensions	2-3
2-3	Major Structure Element - Prototype	2-6
3-1	Photograph of F-14 Main Landing Gear Piston Barrel	3-2
3-2	Indexing Points for Measurements	3-4
3-3	Residual Stress vs. Measurement Position	3-6
3-4	Residual Stress Level vs. Flight Hours	3-9
3-5	Residual Stress Level vs. Catapulted Launches	3-10
3-6	Residual Stress Level vs. Total Landings	3-11
3-7	J-79 Inner and Outer Bearings	3-15
3-8	TF-34 and F-404 Inner and Outer Bearings	3-16
3-9	J-59 Bearing Inner Raceway	3-18
3-10	Differences in the Diffraction Peak Full Width at Half the Maximum Intensity	3-22
3-11	Linear Plot Associated with High Compressive Stresses in Good Bearing	3-23
3-12	Non-Linear Plot of Low Compressive Stresses in Bad Bearing	3-24
3-13	Non-Linear Plot of Tensile Stresses in Bad Bearing	3-25
3-14	Residual Stress vs. Etching Time for Bearing Raceway J-79 (Good)	3-28
3-15	Photograph of Etched Surface on Bearing Inner Ring Raceway	3-30
3-16	Photograph of Unetched Surface on Bearing Inner Ring Raceway	3-30
3-17	Residual Stress vs. Etching Time for Bearing Race J-79 (Bad) Mating Surface Between the Split Inner Ring Section	3-32
3-18	J-52 Compressor Blades 'A' - 'D' and '1' - '4' Measurement Locations	3-34
3-19	TF-30 Fan Blade Measurement Locations	3-35
3-20	P-3 Propeller Hub Section	3-43
3-21	Top View of P-3 Propeller Hub	3-44
3-22	Ten Residual Stress Measurements on Flat Plate Sample	3-49
3-23	Measurement at Angle of 27° to Horizontal and Symmetric Angle of -27° to Horizontal	3-50
3-24	Measurement with Cu K α Radiation (Hard Plating)	3-53
3-25	Measurement with Co K α Radiation (Hard Plating)	3-54
3-26	Measurement with Cr K α Radiation (Hard Plating)	3-55
3-27	Measurement with Cr K α Radiation (Soft Plating)	3-59
3-28	Measurement with Cu K α Radiation (Rotating Sample)	3-60
3-29	Measurement with Co K α Radiation (Rotating Sample)	3-62

3-30	D-Spacing Versus $\text{Sin}^2\psi$ Plot Showing Anomalous $\text{Sin}^2\psi$ Split	3-68
3-31	D-Spacing Versus $\text{Sin}^2\psi$ Plot for Nickel Plating Using Cr K β Radiation	3-69
3-32	Button Head Dog Bone Samples for Low Cycle Axial Fatigue Testing	3-71
3-33	S/N Curves for All Samples	3-75
3-34	S/N Curves for Standard Grinding Samples	3-76
3-35	S/N Curves for Standard Machining Samples	3-77
3-36	S/N Curves for Abusive Grinding Samples	3-78
3-37	S/N Curves for Abusive Machining Samples	3-79
3-38	Failure Locations for Group A (Standard Grinding)	3-80
3-39	Failure Locations for Group B (Abusive Grinding)	3-81
3-40	Failure Locations for Group C (Standard Machining)	3-82
3-41	Failure Locations for Group D (Abusive Machining)	3-83
4-1	Geometry of Diffractometer	4-3
4-2	Beam Which Makes an Angle α	4-5
4-3	Rays Diffracted by Amount y_1	4-7
4-4	Distance r_{spec} from Center of Goniometer	4-9
4-5	Plot of $\Delta d/d$	4-11
4-6	Sample Curvature	4-13
5-1	SBIR Stress Analyzer Hardware Configuration	5-4

LIST OF TABLES

<u>Table</u>		<u>Page</u>
2-1	Weight Reduction	2-4
3-1	History of Selected F-14 Main Landing Gear Pistons	3-5
3-2	Residual Stresses for F-14 Main Landing Gear Pistons	3-7
3-3	Surface Stresses on Inner Ring Raceway	3-20
3-4	Residual Stresses on Outer Rings (J-79 Only)	3-26
3-5	Residual Stress Summary for J-52 Compressor Blade 1	3-36
3-6	Residual Stress Summary for J-52 Compressor Blade 2	3-36
3-7	Residual Stress Summary for J-52 Compressor Blade 3	3-37
3-8	Residual Stress Summary for J-52 Compressor Blade 4	3-37
3-9	Summary of Measurements on Welded and Blended J-52 Compressor Blade 'A'	3-38
3-10	Summary of Measurements on Welded and Blended J-52 Compressor Blade 'B'	3-38
3-11	Summary of Measurements on Welded and Blended J-52 Compressor Blade 'C'	3-39
3-12	Summary of Measurements on Welded and Blended J-52 Compressor Blade 'D'	3-39
3-13	Summary of Measurements on TF-30 Fan Blades	3-41
3-14	Summary of Measurements on P-3 Propeller Hub	3-45
3-15	Summary of Measurements on P-3 Propeller Hub	3-45
3-16	Residual Stresses for the Flat Plate Sample (Hard Plating)	3-51
3-17	Residual Stresses and Diffraction Peak Intensities for Flat Plate Sample (Soft Plating)	3-58
3-18	Residual Stresses and Diffraction Peak Intensities for the Rotated Flat Plate Sample (Hard Plating)	3-58
3-19	Residual Stresses and Diffraction Peak Intensities for the Flat Plate Sample Using Cr K β Radiation	3-64
3-20	Summary of Residual Stress for Navy Pensacola Nickel-Plated Camshaft 75 ASF	3-64
3-21	Surface Residual Stresses in Nickel-Plated Fatigue Samples	3-73
3-22	Axial Fatigue Data Summary - Nickel-Plated 4340 Steel	3-74

ACKNOWLEDGEMENTS

The success of this Phase II effort was directly influenced by the cooperation, support, and information supplied by the Naval Air Rework Facilities.

The F-14 main landing gear data were provided by Bill Lehmann, Tim Rice and Ken Fizer of NARF - Norfolk. They went through the tedious process of tracking the history for these main landing gears. TEC is grateful for their effort and support.

At NARF - North Island, Mark Koegel, Mike Seybold and Gary Kuhlman selected and prepared the bearings sent for testing. They also supplied valuable information about the grinding operations.

Tom Bly and Dale Klahn of NARF - Alameda supplied the P-3 propeller parts. The P-3 hub was expedited at TEC's request despite the absence of key Alameda personnel.

Lewis Bridges and Gray Simpson of NARF - Cherry Point were able to locate compressor blades at various stages of processing and service. They took the time to explain the processing steps. This explanation helped in the data analysis.

Richard McSwain of NARF - Pensacola supplied the fatigue samples. He worked with TEC to define the types of samples needed for the program. He set up the plating and processing parameters, monitored the progress and sent the samples to TEC in time for their inclusion in the program.

Joe Stewart and Sue Macdougall of Oak Ridge National Laboratory, Oak Ridge, Tennessee, performed the scanning electron microscopy. Their support was invaluable to this work and the authors gratefully acknowledge their contribution.

The efforts of these people are appreciated by TEC. The quality of the SBIR program was directly influenced by their participation.

1.0 SUMMARY

1.1 INTRODUCTION

This report documents the effort undertaken on a Phase II Small Business Innovation Research (SBIR) program funded by the Department of the Navy. This was the follow-on effort to a Phase I SBIR program. Briefly, the purpose of the Phase I program was (1) to determine if x-ray stress analysis could be performed reliably and accurately on a wide range of aircraft components, such as landing gears, bearings, turbine blades, and helicopter transmission components; and (2) to develop the necessary procedures to verify that the x-ray technique is applicable to the various alloys from which these components are made. Phase I was successfully completed and that work led to the development of the Phase II program.

The Phase II program had two major objectives. The first was to design, construct, test and deliver to the Navy a prototype stress analysis unit (Figure 1-1) that was smaller, lighter and easier to use than TEC's existing design. The second was to make a large number of residual stress measurements on components and materials of interest to Naval Aviation.

During the later stages of the program, the Navy had a sudden requirement for two stress analysis units to make measurements on an aircraft component of considerable significance to Naval Aviation. The design effort in Task 1 had progressed to the point that the Company was able to assure the Navy that two units of the new design could be built and delivered on an expedited basis.

LOGY for ENI ON



Figure 1-1
Photograph of Deliverable Prototype Unit

This was accomplished on a separately funded contract. These units are currently being used at the Naval Air Rework Facilities at Jacksonville, Florida and San Diego, California.

Beyond the specific demonstration objectives of a Phase II contract, the principle objective of the SBIR program is to help small companies develop a product that will have a commercial application. This specific contract has been totally successful in that respect because TEC has decided to add the unit built for the Navy to its existing line of x-ray stress analysis systems and offer it in the commercial market. As this contract was being completed, TEC placed orders for material to build five units into inventory for sale as a commercial product. These units, when completed, will represent a value in excess of one million dollars.

1.2 PROGRAM OBJECTIVES

The program's objective as set out in the contract Work Statement reads:

The Contractor shall conduct research and development program to develop a nondestructive evaluation instrument (x-ray) for measuring residual stresses in a wide range of Naval Aviation maintenance environments. Work shall include the following tasks:

TASK 1 - Design, construct, and test a stress analysis instrument suitable for depot-level application. Understand Navy needs and requirements with respect to nondestructive evaluation. The design shall be functionally similar to previous units built by the Contractor (i.e., TEC Series 1600) for the Navy

but shall be smaller, lighter and easier to operate in and around aircraft and aircraft components. The Contractor shall undertake instrument design, instrument assembly, and factory testing.

TASK 2 - Create a database of x-ray residual stress information on Naval aircraft components and processing, measure effects of bearing regrinding, measure residual stress effects in nickel and/or chromium plated parts, and measure other process variables. Where required, the Contractor shall measure selected x-ray elastic constants, conduct residual stress measurements of F-14 main landing gears, and determine the stress states. The Contractor shall attempt to determine the failure mechanism of failed parts. The Contractor shall conduct measurements on jet engine bearings and develop a method of detecting abusive grinding. The Contractor will obtain measurements on nickel-plated parts to determine if and how residual stress measurements can be used to determine whether process parameters used in nickel-plating are satisfactory. Additional studies of other components fabricated from such material as titanium and aluminum shall also be conducted.

TASK 3 - Create analytical systems to maximize the usefulness of x-ray stress analysis measurements, develop additional software programs to enhance the usefulness or simplify the operation of the instrument, or aid in the analysis of acquired data.

TASK 4 - Develop a communications link to give the instrument the capability to communicate over phone lines with other similar instruments or other computer systems.

TASK 5 - Deliver one each prototype x-ray stress analysis instrument suitable for depot-level application. The unit shall be accompanied by all standard hardware, software and documentation modified for use on a DEC LSI

11/23 computer, as normally accompanies the commercial version Model 1630 Laboratory X-ray Stress Analysis System.

1.3 RESULTS

1.3.1 Task 1 - Prototype Cart

A prototype unit was fabricated that has all of the functional capabilities and features of previous instruments built by TEC but the volume was reduced by 30% (16 cubic ft) and the weight was reduced by 45% (930 lbs). Other design improvements included larger wheels for improved mobility, relocation of subsystems for improved access, redesign of the power distribution system so the instrument can be operated from standard 15 amp, 110 volt electrical outlets.

1.3.2 Task 2 - Residual Stress Measurements

A large number of measurements were taken on aircraft components and materials. The measurements form the beginning of a database of information available to the Navy. The program demonstrated that not only could the measurements be taken, but truly useful results could be obtained.

Measurements were able to be made in the chromium runout region of complete F-14 main landing gear piston barrels. In Phase I, measurements were only made on a short section which had the attachment legs removed so it was less of a test of the instrument's capability. A comparison between residual stress and service history (flight hours, catapulted launches, total landings) for nineteen F-14 main landing gear pistons failed to provide any correlation. However, experience with F-14 landing gears and with other carrier bred high

performance aircraft landing gears that are also fabricated from 300M steel, suggests that periodic monitoring of the landing gear be recommended. Failures on F-14 pistons have been attributed to fatigue, stress corrosion cracking, hydrogen embrittlement and a combination of these modes. These modes are typically related to tensile surface stresses; therefore, tensile stresses can be an indication of potential failure.

Measurement of jet engine bearings determined that abusively ground bearing raceways can be distinguished from properly ground bearing raceways using residual stress measurements. Properly ground bearing raceways have high compressive stresses, linear d-spacing versus $\sin^2\psi$ plots and smaller values for full-width half-maximum measurements.

Measurements of J-52 titanium alloy jet engine compressor blades suggest compressive residual stresses imparted to the surface by the glass bead peening portion of the weld repair process become reduced to approximately 50% of their level during service. Data was not available to correlate this with engine run time. Following the welding and blending process, the residual stresses in the weld repair region are substantially increased by beading and peening.

Analysis of an aluminum P-3 propeller hub indicated the presence of uniform compressive surface residual stresses at cracked and uncracked locations. This indicates that the stresses causing cracking in the threaded region do not have their origin at the surface.

Studies of nickel-plated samples determined that using Cr K β radiation gave better results than the more commonly used Cr K α radiation. This is an extremely useful discovery because measurements taken using Cr K β radiation will be easier to interpret and be more accurate. Also, the study determined that s-shaped d-spacing versus $\sin^2\psi$ curves were attributed to preferred orientation of the grains in the nickel-plating. It was also found that {111} planes are oriented parallel to the surface of the plating. A study of nickel-plated test specimens before and after fatigue testing showed that for this set of samples, machined nickel-plated parts have an improved fatigue life compared to ground nickel-plated parts. Residual stress levels, however, were unaffected by fatigue testing.

1.3.3 Task 3 - Analytical Systems

An analysis was made which shows the amount that the deviation of the sample surface from the focusing circle of the goniometer can affect the accuracy of residual stress measurements. These types of errors are increased when the sample surface is curved rather than flat. For most measurements, these errors are sufficiently small as to not affect the results.

1.3.4 Task 4 - Communications Link

A communications capability was developed that permits stress analysis instruments to communicate with each other over normal phone lines. All that is required is a Hayes compatible modem at the location of each instrument and computer programs written by TEC. This important feature has a number of benefits. Data obtained at one location can be sent to another location for

additional analysis. Troubleshooting and diagnostics can be performed from a remote location. Software updates can be sent to users via this communication link and immediately tested.

2.0 TASK 1 - PROTOTYPE CART

The objective of this task was the design, construction and testing of a stress analysis instrument suitable for depot-level application. This analysis unit was to be different in several important ways from the analysis units that the Company had previously built. To be suitable for depot-level applications, the unit needed to be smaller, lighter and easier to move from building to building or within buildings that had uneven floors and obstacles, such as tracks in the floor, that hindered mobility. Design changes that would make the unit easier to operate and maintain were also identified as desirable. These objectives were met with the design of a unit that was 45% lighter and 30% smaller in volume and incorporated a number of features to make the new unit easier to use and maintain.

2.1 SIZE REDUCTION

The result of the design effort has been a substantial reduction in the cart size and weight. The dimensions of the prototype cart design (Figure 2-1) can be compared to the original cart design shown in Figure 2-2. Rearranging the major components made it possible to design a new cart that is 70% of the volume of the original. The reduction in width, from 32 inches to 28 inches, makes it possible to get the cart through narrow doorways which exist in many older facilities. The reduction in length, from 76 to 64 inches, improves the maneuverability of the unit and, with the attendant width reduction, the unit can fit into smaller spaces.

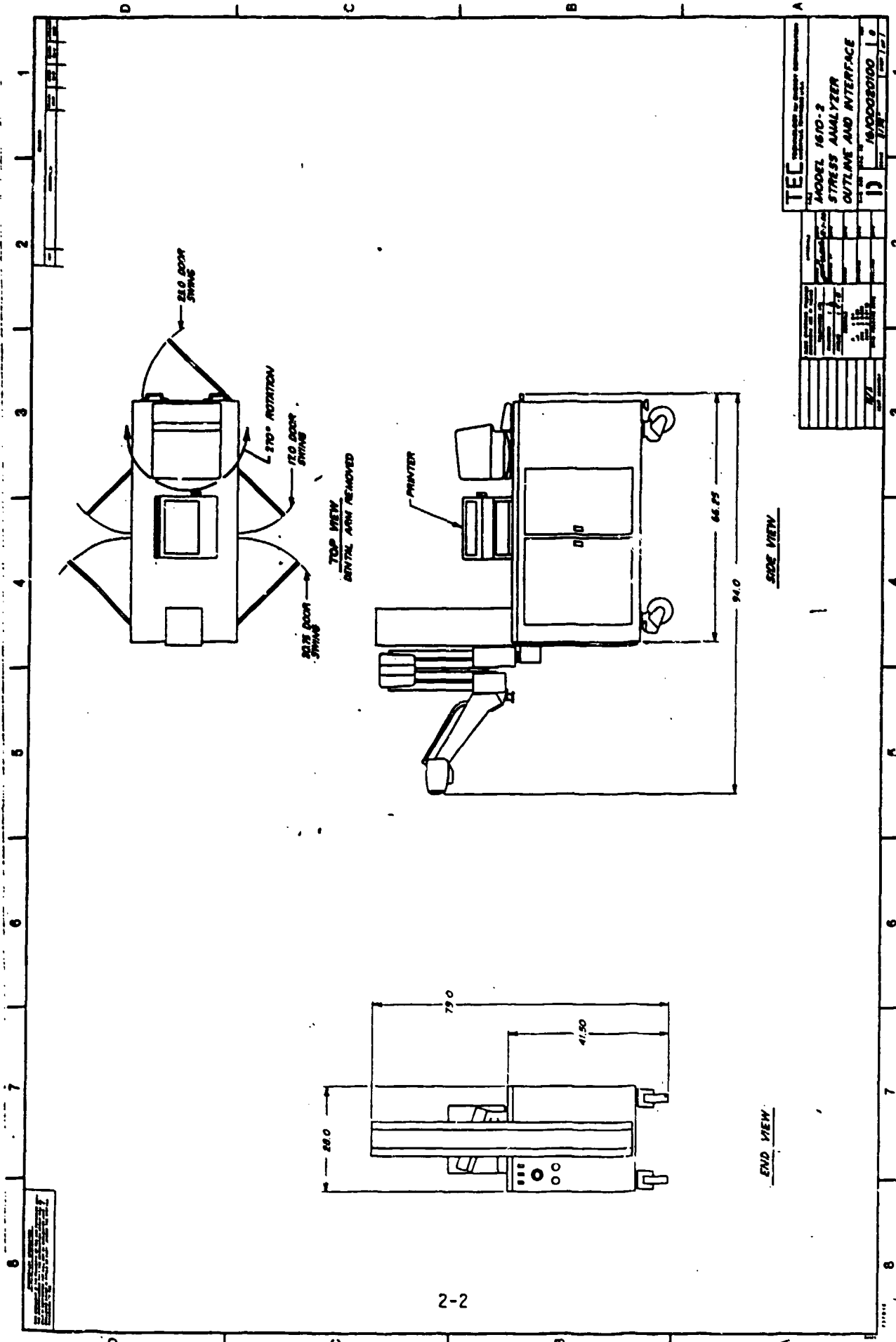


Figure 2-1
 Prototype Cart Design Dimensions

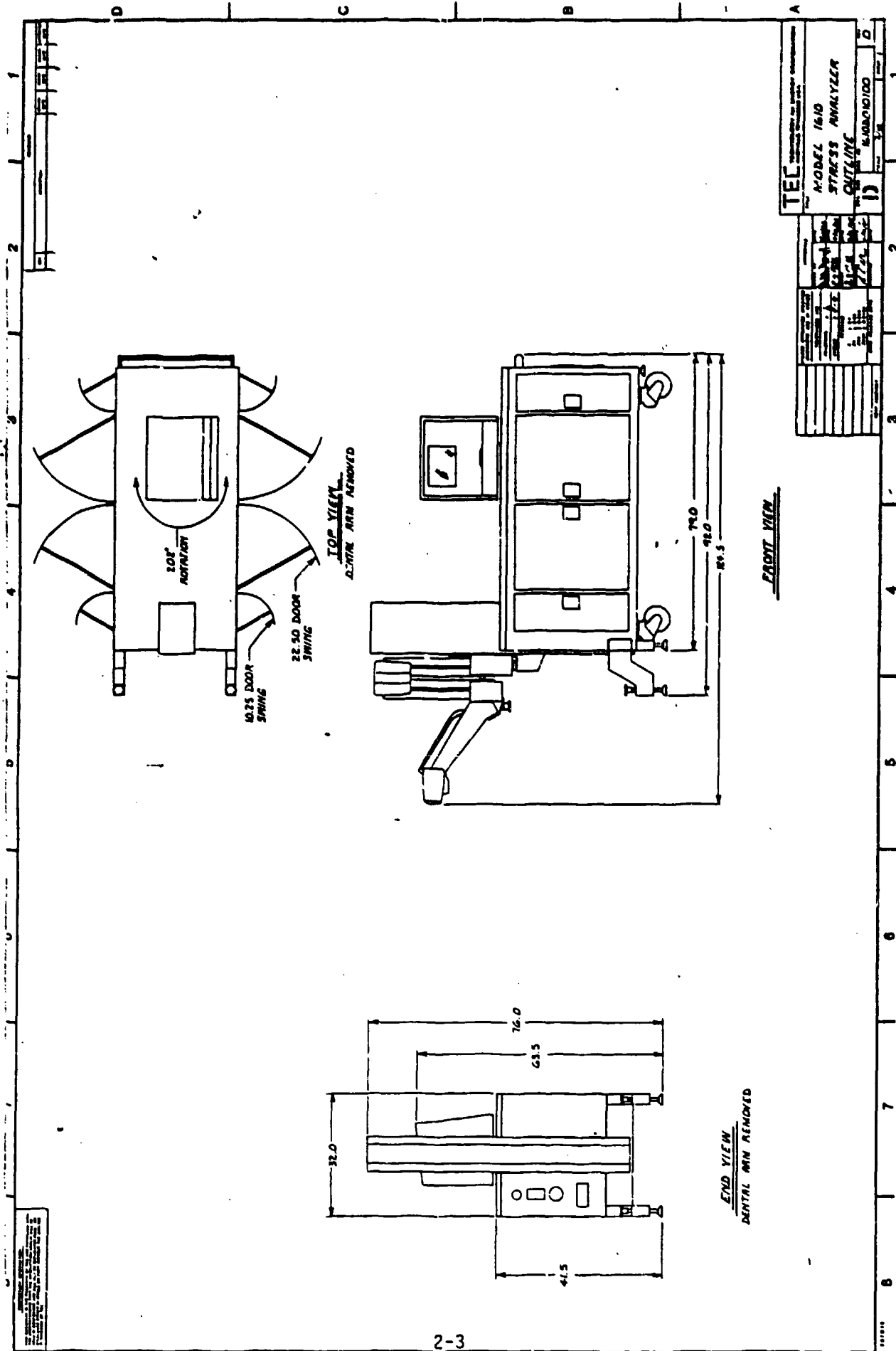


Figure 2-2
Original Cart Design Dimensions

2.2 WEIGHT REDUCTION

Weight reduction was a design objective that would also improve the maneuverability of the unit. Weight is particularly important where there are grades or uneven surfaces. In conjunction with reducing the weight, the diameter of the wheels on the shock-absorbing casters was increased from four inches to six inches to provide improved travel over obstacles that might be encountered in the service environment.

Since the design effort indicated that large reductions in weight would be achieved by the cart redesign, the weight of the tower and articulating arm assembly began to take on greater importance. Since this weight is located at one end of the cart, there was concern that the balance of the cart would be affected. A review of the original tower design showed that modifications to the elevating mechanism and other changes had the potential for saving about 200 pounds. Therefore, a tower assembly, lighter in weight with the same capability, was designed and a prototype was built.

The weight reductions achieved through redesign are summarized in Table 2-1.

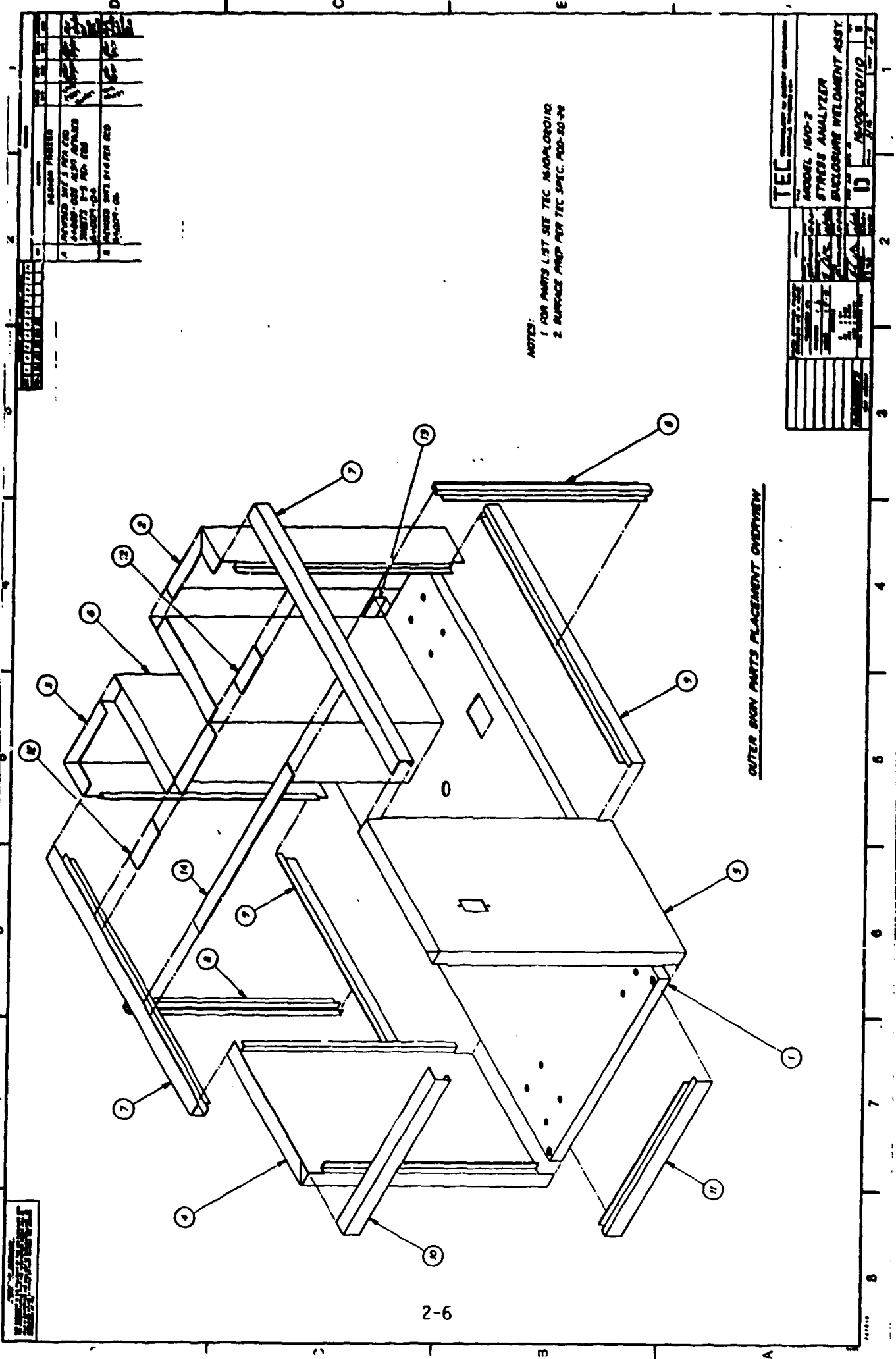
Table 2-1
Weight Reduction

	<u>Cart Assembly</u>	<u>Tower Assembly</u>	<u>Total System</u>
Current Design	1600 lbs.	450 lbs.	2050 lbs.
Prototype Design	880 lbs.	240 lbs.	1120 lbs.
Weight Savings	720 lbs.	210 lbs.	930 lbs.
% Reduction	45%	47%	45%

This weight reduction has been accomplished not only by reducing the size of the cart but also by using more sophisticated sheet metal construction techniques to obtain the reduction in weight without sacrificing strength or stiffness. The previous design had been constructed by first welding 2-inch angle iron into a three-dimensional rectangular frame and then welding 10-gauge steel sheet to the frame. In the prototype, the base of the cart is 10-gauge steel but the remainder is 14-gauge steel, and no angle iron is used. Figure 2-3 illustrates the major structure element of the prototype cart.

The weight savings in the tower assembly was accomplished by first redesigning the mechanism for raising and lowering the articulated arm and then changing the material of construction from 10 gauge to 14 gauge. In the original design, the articulated arm mounted to a precision twin-rail ball-slide arrangement. It was raised and lowered using a motor and gear reducer driving a double roller chain. An 80-lb counterweight travels inside the tower to overcome inertial forces when raising the arm and to prevent overrun when stopping the arm on its downward travel. The motor, gear reducer and drive sprockets were all located at the top of the tower and the normal position of the counterweight was at mid-height. Thus, the center of gravity of the tower was fairly high.

The prototype tower assembly retains the twin-rail ball-slide arrangement but the chain drive and counterweight are replaced by a ball-screw and electric brake. The motor and reduction gear box is located at the bottom of the tower assembly for an improved weight distribution. A ball-nut attached to the



NOTES:
 1 FOR PARTS LIST SEE TEC NAJOPLO010
 2 SURFACE PREP PER TEC SPEC. PDD-80-78

OUTER SKIN PARTS PLACEMENT OVERVIEW

TEC	
MODEL 1600-2	
STRESS ANALYZER	
ENCLOSURE WELDMENT ASST.	
REV	DATE
1	11/10/78
2	11/10/78
3	11/10/78
4	11/10/78
5	11/10/78
6	11/10/78
7	11/10/78
8	11/10/78
9	11/10/78
10	11/10/78
11	11/10/78
12	11/10/78

REV	DATE	DESCRIPTION
1	11/10/78	ISSUED FOR FAB
2	11/10/78	ISSUED FOR FAB
3	11/10/78	ISSUED FOR FAB
4	11/10/78	ISSUED FOR FAB
5	11/10/78	ISSUED FOR FAB
6	11/10/78	ISSUED FOR FAB
7	11/10/78	ISSUED FOR FAB
8	11/10/78	ISSUED FOR FAB
9	11/10/78	ISSUED FOR FAB
10	11/10/78	ISSUED FOR FAB
11	11/10/78	ISSUED FOR FAB
12	11/10/78	ISSUED FOR FAB

Figure 2-3

Major Structure Element - Prototype

mounting point of the articulated arm assembly is driven upward or downward by reversing the direction of rotation of the ball-screw. There is adequate torque with this design to overcome the inertia of the system when raising the articulated arm. To prevent overrun when the arm is being lowered and the motor is turned off at the selected height, an electrically operated brake stops the rotation of the ball-screw. Power is applied to the brake to release it and the removal of power causes the brake to actuate under spring load. This is a fail-safe feature.

2.3 OTHER DESIGN IMPROVEMENTS

In the design of the prototype, attention was paid to any area which would result in either improvement in the ease of use of the unit or in its maintainability. Any improvements gained in these areas would translate directly into a unit better suited to depot-level applications. Some of the improvements that were obtained are described below.

2.3.1 CRT

On the original design, the CRT was placed in a separate metal enclosure to protect the CRT from the environment (Figure 2-2). It is unlikely that such additional protection is required, so for the prototype unit, the CRT was mounted to a swivel base and placed on top of the cart (Figure 2-1). This results in less space being used up by the CRT, as well as contributes to the overall weight and size reduction. The user has the freedom with the prototype to move the CRT to an alternate location on top of the cart or to remove it from the cart altogether. Moreover, access to the terminal for maintenance is greatly simplified.

2.3.2 Relocation of Printer

In the original design, the printer was located in a drawer in the side of the cart. This location made the printer somewhat awkward to use, particularly if the CRT was rotated so that the operator was standing on the other side of the cart. In the new design, the printer was moved to the top of the cart where it is more accessible and easier to use; and it can be turned easily to whichever side the operator is working.

2.3.3 Power Distribution

The power distribution system within the cart was redesigned to reduce the number of components and simplify the system. As part of this redesign, the air conditioner was placed on a separate circuit. The instrument now uses two 15-amp three-prong plugs rather than a special 30-amp twist-lock plug. This will permit use of the instrument in any location where there are standard 15-amp wall receptacles.

2.3.4 Miscellaneous Changes

The cart is air conditioned so the electronics can be kept at the proper operating temperature regardless of the ambient environment. In the original design, the hot air exhaust from the air conditioner exited through a grill in the top of the cart near the handle bar. Not only was the grill uncomfortably warm to the touch, the blast of hot air could be annoying to the operator. In the new design, the hot air is exhausted through the bottom of the cart onto the floor in a manner that should be unnoticed by the operator.

The coolant systems for the x-ray tube was redesigned to simplify the plumbing layout and to make it easier for the operator to replenish the coolant reservoir.

The manner in which the computer system and related are installed now make it possible for one person to remove a major subsystem, whereas previously, it required two people. Access to the computers and other electronic subsystems for maintenance is also improved.

3.0 TASK 2 - RESIDUAL STRESS MEASUREMENTS

The objective of this task was to make measurements on a number of components and materials of interest to Naval Aviation. These measurements form the beginning of a data base of residual stress information. Additional objectives of the program were to use the information to determine if failure of F-14 landing gear pistons could be predicted, to see if abusive grinding of bearings could be detected and to determine if process parameters such as nickel-plating or weld repairs of titanium parts are satisfactory from the standpoint of process control and quality control.

In this section of the report, each of the measurement activities is discussed separately and the results are presented. A major effort was devoted to nickel-plating, which is presented as the last subsection.

3.1 F-14 MAIN LANDING GEAR

The F-14 main landing gear piston barrel was selected for study to determine if residual stress measurements can be related to service life. Measurements were carried out at Norfolk by Navy employees using a procedure developed by TEC. Twenty F-14 main landing gear (MLG) pistons were measured for residual stresses at NARF-Norfolk on their TEC Model 1610 Stress Analyzer. Service history was obtained for nineteen of these pistons.

3.1.1 Preparation of Measurement Procedure

A scrapped F-14 main landing gear piston barrel was received from Norfolk (Figure 3-1). A series of measurements were made to establish the measurement procedures and to obtain good data from the part. The axle on the landing gear

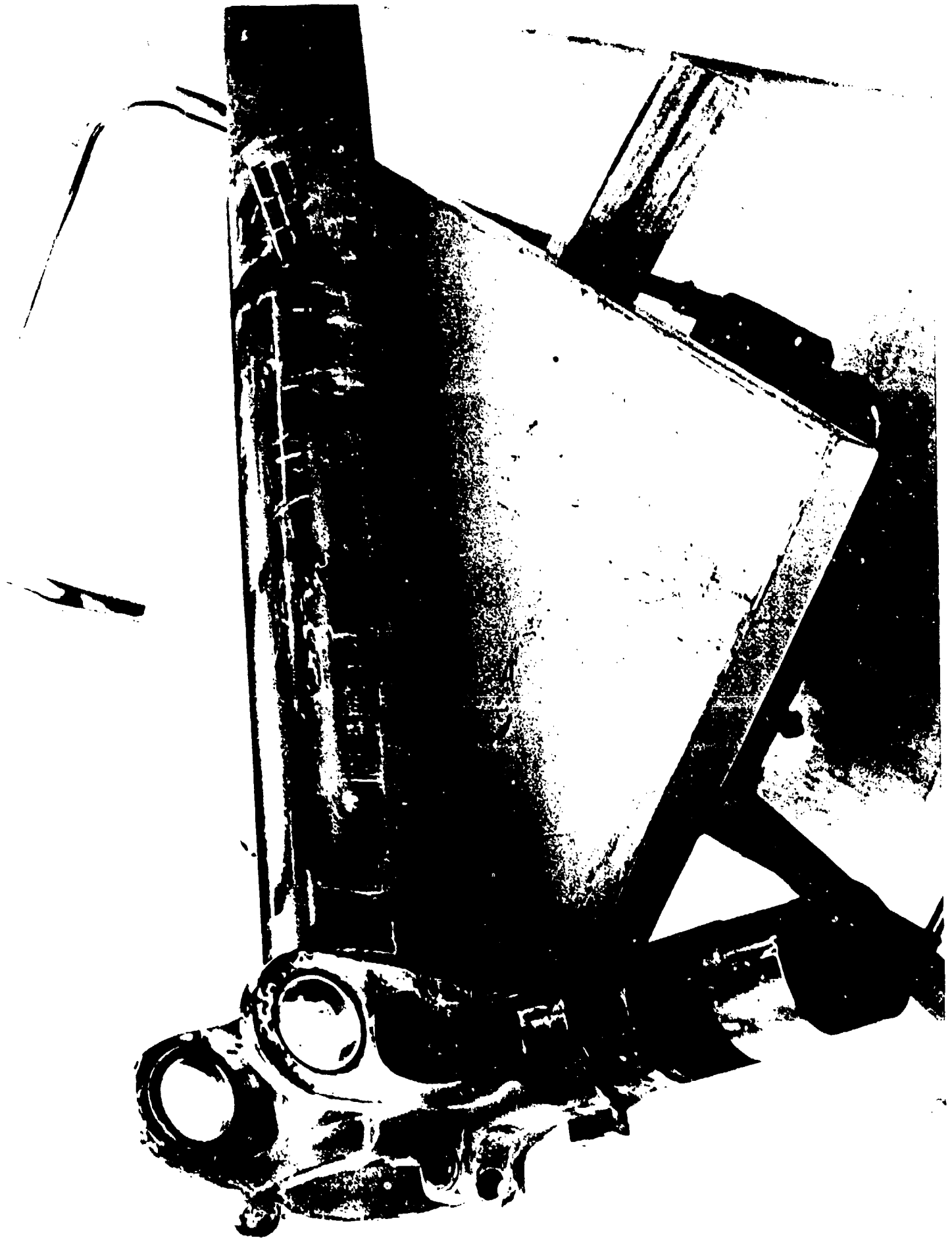


Figure 3-1
Photograph of F-14 Main Landing Gear Piston Barrel

interferes with the diffractometer head so that measurement cannot be made around the complete circumference of the gear. However, it is possible to get within about 22 degrees as measured from the axle center line and this is within the area of interest. The measurements are taken in the area of the chromium runout at the circumferential locations corresponding to the indexing points shown in Figure 3-2.

3.1.2 Service History

Pistons that had been in service from 4 to 14 years were used for these measurements. Nine left-handed pistons and eleven right-handed pistons were measured. The service history was assimilated for all but one left-handed piston (K-0344). One piston (K-1136) was new, and two pistons (K-0193 and K-1068) were a matched set. The matched pistons spent their entire life on a Grumman test plane, and about 100 of the total 237 arrested landings (traps) occurred on land. It is speculated that the land traps are less severe than carrier traps. The number of flight hours (excluding the new piston) ranged from 1,236 hours for the matched pistons to 3,400 hours for piston K-1100. The pistons represent a total number of landings that range from 1326 (K-0577) to 6506 (K-0581). Of these landings, the number that were arrested ranged from 237 for the matched pair to 1,061 for piston K-1102. The number of catapulted launches ranged from 131 for the matched pair to 1,056 for piston K-1102. These data are listed in Table 3-1.

3.1.3 Results

The residual stresses are listed in Table 3-2 and plotted for each measurement position in Figure 3-3. Examination of Table 3-2 shows a large variation in stresses at the four measurement positions. This variation apparently becomes

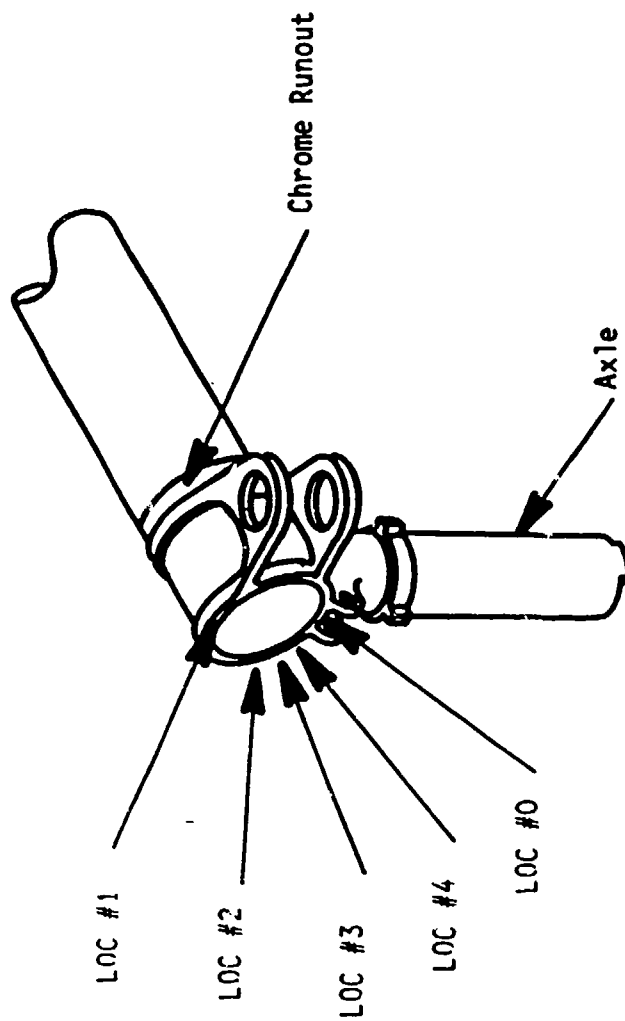


Figure 3-2
Indexing Points for Measurements

Table 3-1.

History of Selected F-14 Main Landing Gear Pistons

<u>Serial Number</u>	<u>Life</u>	<u>Flight Hours</u>	<u>Total Landings</u>	<u>Catapulted Launches</u>	<u>Arrested Landings</u>
K-0133	04/01/73 - 07/16/86	2,116	2,507	344	344
K-0173	Traced to 08/01/83	1,351	2,452	462	445
K-0193	08/31/72 - 12/01/86	1,236	2,518	131	237
K-0272	Traced to 08/16/82	1,616	2,123	440	435
K-0291	09/01/75 - 03/31/86	2,689	2,841	895	909
K-0577	Traced to 07/01/83	1,517	1,328	556	557
K-0851	07/03/78 - 06/04/86	2,653	6,506	478	485
K-0645	03/02/81 - 12/21/85	2,239	2,526	610	403
K-1028	05/02/73 - 11/21/86	1,924	2,548	620	626
K-1068	08/31/72 - 12/01/86	1,236	2,518	131	237
K-1100	04/25/74 - 08/11/86	3,400	4,191	937	908
K-1102	05/01/74 - 10/01/84	3,081	1,725	1,056	1,061
K-1106	07/01/74 - 12/02/85	2,566	3,373	841	851
K-1136	NEW	0	0	0	0
K-1200	Traced to 05/14/82	1,881	2,169	443	440
K-1250	03/10/76 - 03/15/86	2,986	5,781	272	291
K-1360	11/08/76 - 12/31/85	2,382	2,739	705	930
K-1498	Traced to 12/08/81	1,256	1,570	353	359
K-1590	Traced to 04/03/84	2,264	2,888	623	627

Table 3-2.

Residual Stresses for F-14 Main Landing Gear Pistons

Piston	Position 1 (180° from axle)	Position 2 (90° from axle)	Position 3 (45° from axle)	Position 4 (-22.5° from axle)*
(L) K-0133	- 82.4 ± 11.1 (H) -101.5 ± 7.7	- 99.8 ± 11.1	-74.5 ± 7.9	-26.5 ± 7.9
(L) K-017	- 76.5 ± 7.6 (H) - 97.6 ± 7.7	-115.8 ± 10.3	-102.2 ± 8.1	-96.7 ± 10.0
(L) K-0193	-110.6 ± 8.6	-102.5 ± 8.1	- 95.9 ± 7.1	-73.5 ± 7.8
(L) K-0272	-107.6 ± 7.1	- 98.6 ± 7.3	- 58.2 ± 8.1	-25.2 ± 8.1
(L) K-0291	-107.6 ± 8.5	- 91.3 ± 10.9 -101.4 ± 8.7	- 91.7 ± 5.9	-65.7 ± 6.7
(L) K-0334	-159.1 ± 10.8	-128.2 ± 25.6 -101.9 ± 48.7	- 53.2 ± 29.7	+13.9 ± 38.8
(L) K-0577	- 93.4 ± 7.7	-131.5 ± 8.5	- 26.4 ± 7.2	+11.3 ± 7.3
(L) K-0581	-107.6 ± 6.6	- 85.4 ± 8.6	- 50.9 ± 7.5	-25.7 ± 8.2
(L) K-0645	- 96.7 ± 10.5 - 84.8 ± 7.0	-107.6 ± 5.5	-136.5 ± 7.1	-135.8 ± 6.0
(R) K-1028	-123.7 ± 8.1	-106.5 ± 7.9	-110.8 ± 7.2	- 95.0 ± 7.2(30°)
(R) K-1068	-122.9 ± 6.3	-122.2 ± 8.4	-107.4 ± 7.5	- 85.4 ± 7.7
(R) K-1100	-157.0 ± 17.5	-156.4 ± 12.7	-156.7 ± 15.6	-129.9 ± 7.0
(R) K-1102	- 83.5 ± 11.1 - 95.1 ± 15.3 (H)	- 51.5 ± 11.5	+ 3.3 ± 7.7	
(R) K-1106	-169.2 ± 18.6	-163.8 ± 7.9	-152.5 ± 8.1	-145.3 ± 6.7(30°)
(R) K-1136 (NEW)	-121.1 ± 6.2	- 96.7 ± 5.5	-112.7 ± 8.3	-112.7 ± 8.0
(R) K-1200	-127.7 ± 8.7	- 98.7 ± 26.8 -113.7 ± 17.6 -103.9 ± 19.6	-152.8 ± 40.1 -122.9 ± 12.9	-106.1 ± 10.1(35°)
(R) K-1250	-126.2 ± 6.5	-118.3 ± 7.1	- 99.9 ± 6.9	-102.3 ± 7.1
(R) K-1360	-120.8 ± 6.0	-107.5 ± 8.5	- 99.0 ± 6.0	- 61.3 ± 8.4
(R) K-1498	-120.5 ± 7.3	-103.0 ± 7.7	- 5.0 ± 12.4 + 4.7 ± 7.7	+ 30.0 ± 13.3(35°)
(R) K-1590	-135.9 ± 10.1	-109.2 ± 12.0	-117.9 ± 16.5	-----

*P4 was not accessible on the right-handed piston.

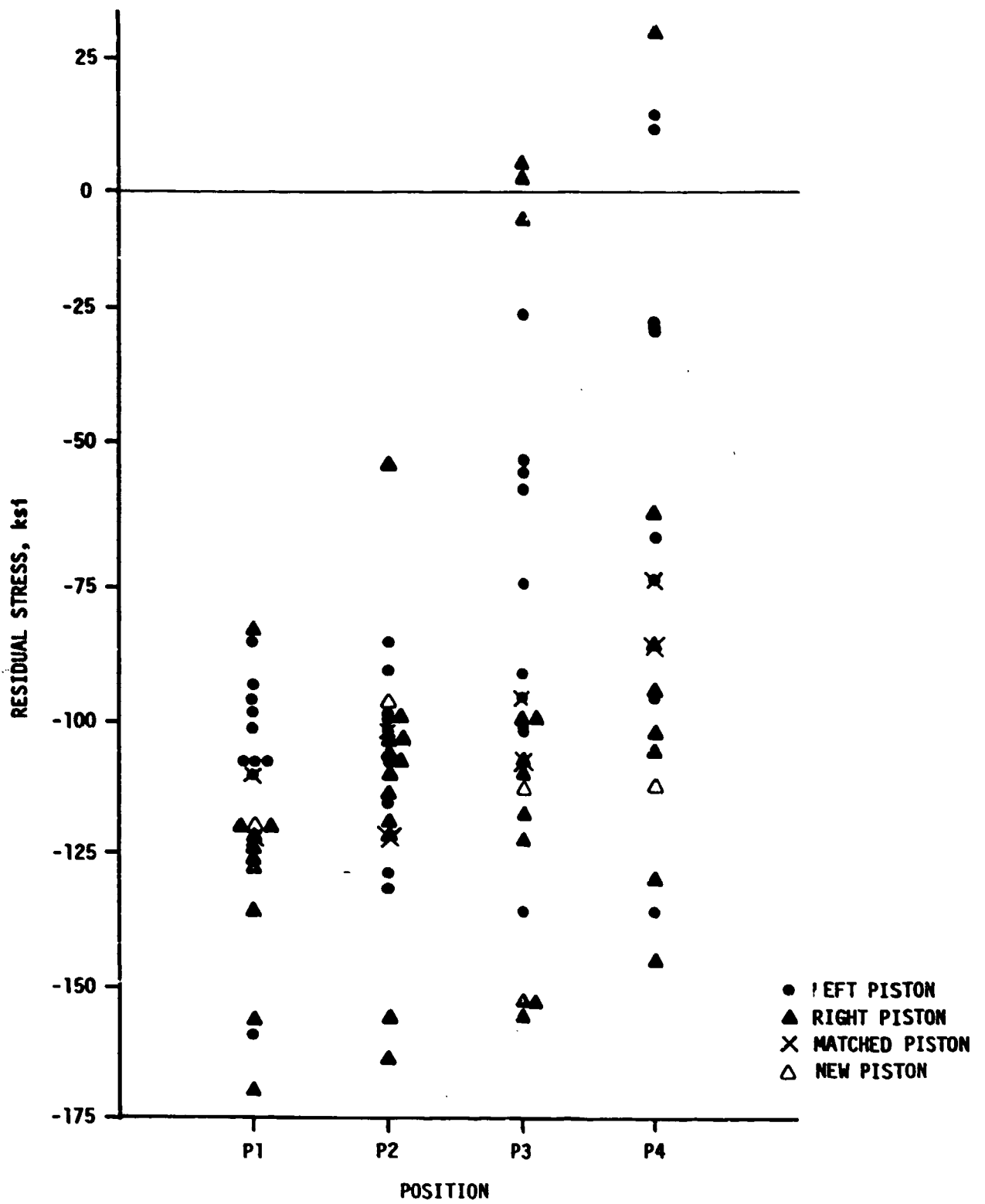
The P4 position ranged from -25° to 35° from the axle.

(L) Left-handed piston.

(R) Right-handed piston.

(H) Measurement made in circumferential (hoop) direction.

All measurements were in the longitudinal direction unless marked.



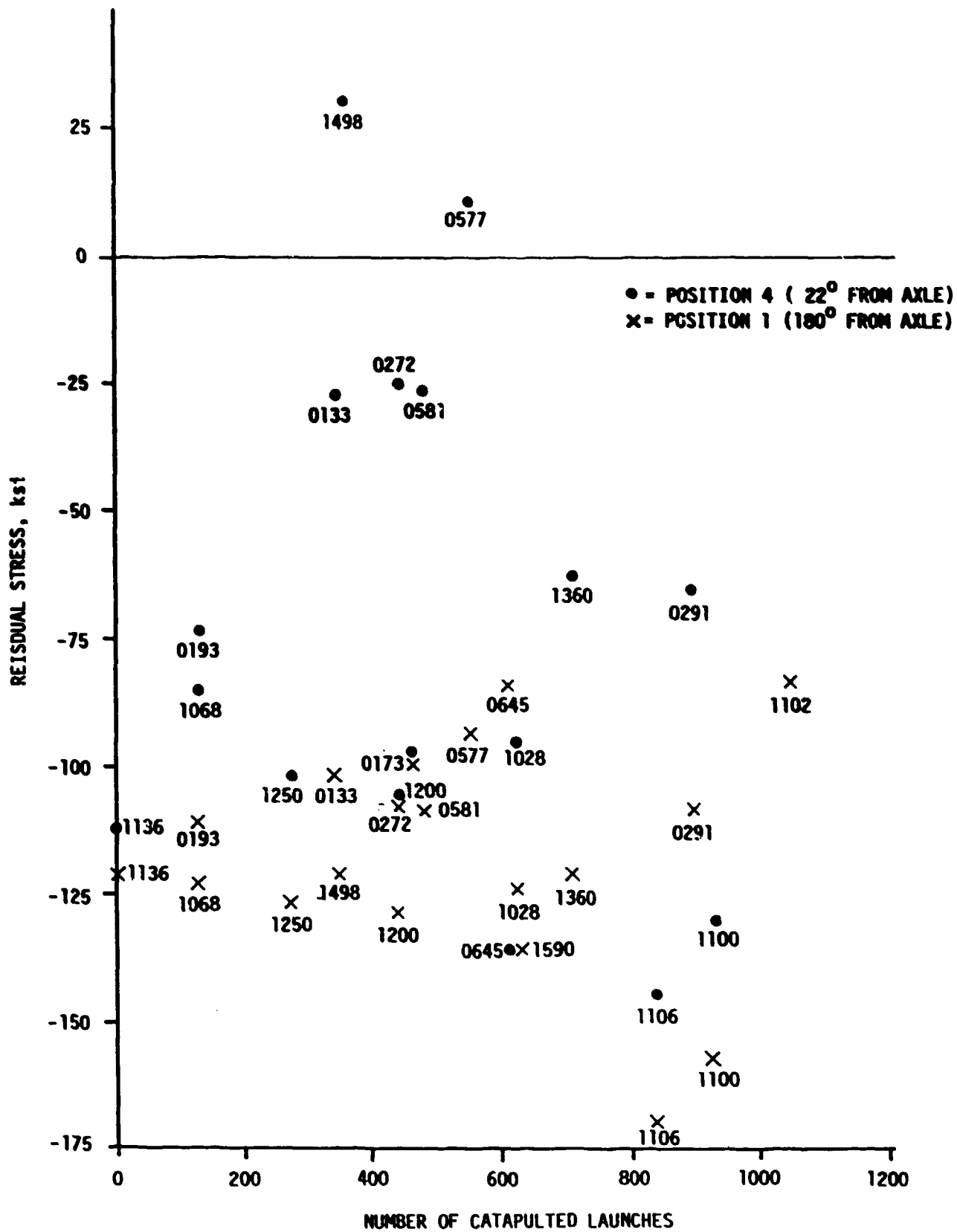
32121A23

Figure 3-3
Residual Stress vs. Measurement Position

greater nearer the axle. Past F-14 failures have been near the chromium runout region of the piston near the axle.¹ All of the measured stresses at 180° from the axle (Position 1) were more compressive than 80 ksi. Position 4, which is 22° to 35° from the axle, had both tensile and compressive stresses. They ranged from +30 to -145 ksi. Measurements at Position 3 (45° from the axle) were also compressive and tensile ranging from -157 to +5 ksi. Similar to Position 1, Position 2 (90° from the axle) had compressive residual stresses. They ranged from -52 to -164 ksi. In all but one case the stress at Position 1 was more compressive than at Position 4. For piston K-0645 the residual stress was -84 ksi at Position 1 and -136 ksi at Position 4. The high and low stresses at each position were found on right-handed pistons. On the matched pair of pistons, the right-handed piston was always more compressive than the left-handed piston. It is not known if this observation is significant, especially since the error bars for the stresses overlap. Stresses on the new piston were uniform at the four positions. They ranged from -97 to -121 ksi.

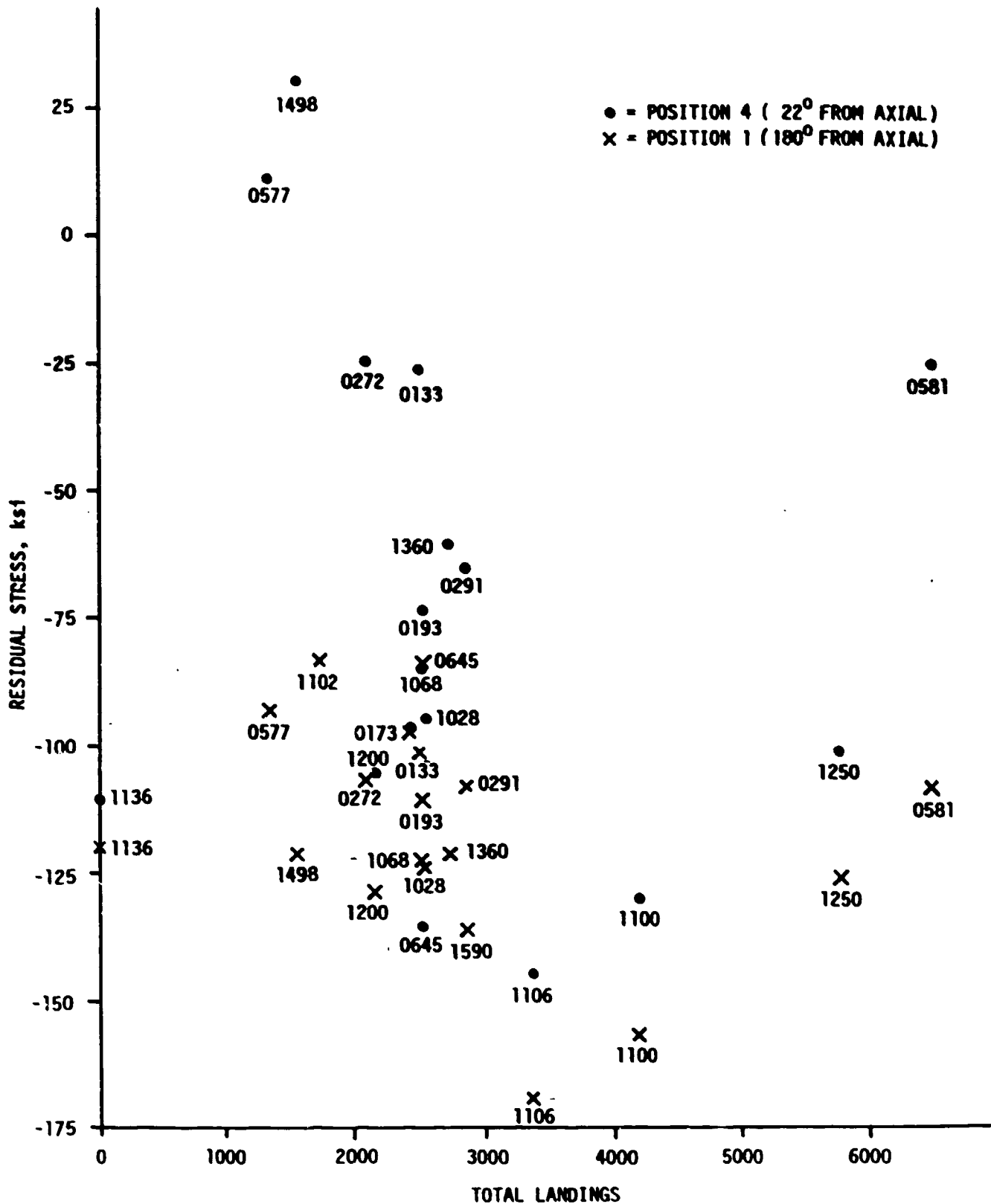
Figures 3-4, 3-5, and 3-6 show the residual stress level versus several operation parameters - total flight hours, catapulted launches, and total landings. Other data presented in these figures do not show any relationship between the residual stresses and the plotted operation parameter. It is possible that trends may become evident if a much larger population is sampled. Previous experience with the same material (300M) under similar circumstances indicated that crack initiation began when the stresses became less compressive (more tensile). If this is

1. Conversation with Ken Fizer of NARF-Norfolk.



32121A24

Figure 3-5
 Residual Stress Level vs. Catapulted Launches



32121A22

Figure 3-6
Residual Stress Level vs. Total Landings

the case for the F-14 pistons, then periodic monitoring of residual stresses may indicate which pistons are in need of reworking.

The reported failure modes for the F-14 MLG's are fatigue, stress corrosion cracking, hydrogen embrittlement, or a combination of these modes.² Tensile stresses at the surface are often a contributing factor for these failure modes. Location of tensile stresses near the axle in the chromium runout region is consistent with the observed failure initiation in this region. Previous work with MLG's resulted in three categories.³

- 1) MLGs with high compressive stress at the critical locations could be returned to service.
- 2) MLGs with low compressive or tensile stresses could be returned to service after reworking. Shot peening was part of the rework procedure which resulted in restoring high compressive stresses at the surface.
- 3) MLGs with high tensile stresses could not be reused.

Additional information is necessary to quantify the magnitudes of the stresses for these three categories for the F-14 MLGs.

3.1.4 Conclusions

There was no correlation found between residual stress level and the flight hours, number of catapulted launches, or number of arrested landings. If piston

-
2. Conversation with Ken Fizer of NARF-Norfolk.
 3. Conversations with McDonnell Douglas personnel.

failures are associated with fading compressive stresses then periodic monitoring of the stress level may be the most prudent course of action. Since the acknowledged failure modes (fatigue, stress corrosion cracking, hydrogen embrittlement, or a combination of these) are generally associated with tensile residual stresses at the surface, periodic monitoring of the stresses near the axle should help to determine which MLGs can be reworked.

3.2 BEARING RACEWAY GRINDING

3.2.1 Introduction

The objective of this portion of the measurement program was to determine if the use of residual stress measurements could identify abusive grinding of bearing raceways. If it could be used on bearings, the technique could potentially be useful on other applications where grinding is used as the final machining operation. Three sets of bearings were analyzed for residual stress levels. Each set consisted of a good (properly ground) and a bad (abusively ground) bearing raceway. The bearings were from a J-79, TF-34, and F-404 engine (Figures 3-7 and 3-8). The purpose of this measurement program was to quantify differences between the good and bad bearings.

3.2.2 Measurements

Measurements were made on the surfaces of all the inner ring raceways at the location of rolling element contact. These surfaces were more accessible than those on the inner surface of the outer ring raceways. Also, the inner ring raceways in these bearings should experience the higher loading stresses in operation. This study concentrated on the J-79 bearings because it was thought that the bad bearing was one that had spalled during proof testing. A later discussion of the stress results with NARF - North Island personnel revealed that the bad J-79 bearing sent to TEC was not the one that had spalled. An unsuccessful attempt was made to locate the spalled bearing and ship it to TEC for testing under the Phase II program. Both surface and subsurface measurements were made on both the good and bad J-79 bearings.



Figure 3-7
J-79 Inner and Outer Bearings



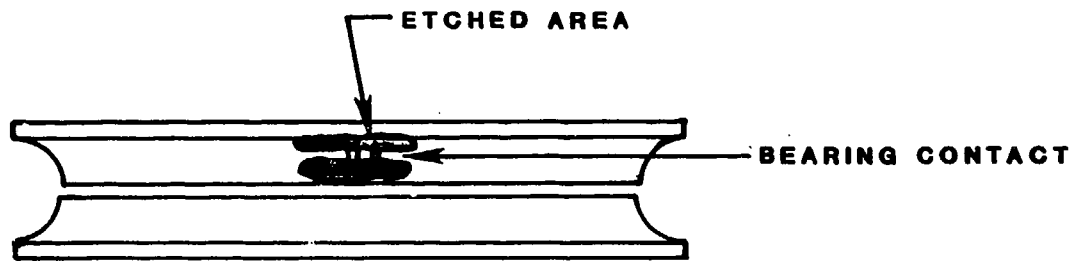
Figure 3-8
TF-34 and F-404 Inner and Outer Bearings

The subsurface measurements were made by removing a minute layer of material and repeating the stress measurement. A chemical etchant, Tarasov's etch, was used, not only to remove the surface layers but also to show the areas of martensite versus over-tempered martensite. Previous work performed by S. W. Shin and G. H. Walter¹ used this etchant on bearing races to show clearly the areas of grinding burn. They estimated that this etchant removed less than 0.001" of material for every 15-second etch cycle. The geometry of the bearing raceways made it impractical to determine the amount of material removed.

The abusively ground J-79 race had periodic axial stains that were assumed to be related to areas of martensite alternated with areas of over-tempered martensite. A very small collimated beam was used to measure the stresses associated with each area. After completing the surface measurements, the raceway was etched to reveal the over-tempered martensite. A thin, light-colored circumferential strip at the bearing contact surface was accentuated by the etchant (Figure 3-9). Axial striations similar to the stains found before etching were visible within the circumferential strip.

The good J-79 raceway was uniformly metallic in coloration. Measurements were first made on the inner ring raceway surface followed by measurements made on the etched areas. The Tarasov's etch uniformly blackened the raceway surface in contrast to the light and dark regions found on the abusively ground bearing.

1. "Case Histories of Residual Stress Related Component Failures," Residual Stress for Designers and Metallurgists, American Society for Metals.



32121A26

Figure 3-9
J-59 Bearing Inner Raceway

Additional measurements were made on the mating surface between the split inner ring sections of the burned J-79 bearing to compare this surface with the raceway. The measurement of this flat surface could help determine if the complex geometry of the raceway affected the d-spacing versus $\sin^2\psi$ plots. Measurements performed during the Phase I effort had $\sin^2\psi$ splits that were attributed to either shear stresses or geometric factors.

Surface measurements were made on both J-79 bearing outer ring racesways. These measurements were made in the raceway at the rolling element contact and also on the outside diameter surface.

3.2.3 Results and Discussion

3.2.3.1 Inner Ring Racesways - Results of the x-ray diffraction stress analysis are given in Table 3-3. Surface stresses in the raceway of the inner rings from the good bearing were more compressive than those from the bad bearings. For the J-79 bearings, the good bearing had uniform compressive stresses in both the axial and circumferential directions (-112 to -129 ksi). The bad J-79 bearing inner ring raceway had all tensile stresses (+69 to +113 ksi). Stresses in the bad TF-34 bearing inner ring ranged from +4 to -67 ksi, while those in the same good bearing were -142 and -170 ksi. Similarly, stresses in the bad F-404 bearing were -43 and +42 ksi compared to -146 and -152 ksi for the good F-404 raceway. The compressive stress in the bad F-404 bearing was measured near the edge of the raceway.

A consistent result, seen when comparing the inner ring racesways of the properly ground bearings to the abusively ground bearings, was the differences in the

Table 3-3.

Surface Stresses on Inner Ring Raceway

<u>Bearing</u>	<u>Direction</u>	<u>Stress, ksi</u>	<u>FWHM, °2θ</u>
J-79, Good	Circumferential	-119.7 ± 21.8	4.6
	Circumferential	-128.7 ± 23.4	4.6
	Circumferential	-112.2 ± 11.4	4.8
	Axial	-117.2 ± 17.3	4.8
	Axial	-114.2 ± 10.1	4.7
J-79, Bad	Circumferential	+ 70.0 ± 28.0	5.4
	Circumferential	+112.7 ± 32.4	5.3
	Axial	+ 69.1 ± 24.7	5.3
	Axial	+ 76.8 ± 23.3	5.6
TF-34, Good	Circumferential	-142.4 ± 9.2	4.8
	Axial	-170.0 ± 12.2	4.8
TF-34, Bad	Circumferential	- 45.1 ± 16.8	5.2
	Circumferential	- 45.5 ± 16.7	5.1
	Circumferential	- 39.0 ± 18.3	5.2
	Circumferential	+ 4.3 ± 23.2	5.7
	Circumferential	- 4.9 ± 20.9	5.5
	Axial	- 66.9 ± 13.0	5.2
F-404, Good	Axial	- 7.1 ± 17.8	5.8
	Circumferential	-151.5 ± 9.0	4.8
F-404, Good	Circumferential	-140.1 ± 13.2*	4.8
	Circumferential	-140.1 ± 13.2*	4.8
F-404, Bad	Circumferential	+ 42.3 ± 26.6	5.7
	Circumferential	- 43.4 ± 16.7*	5.5

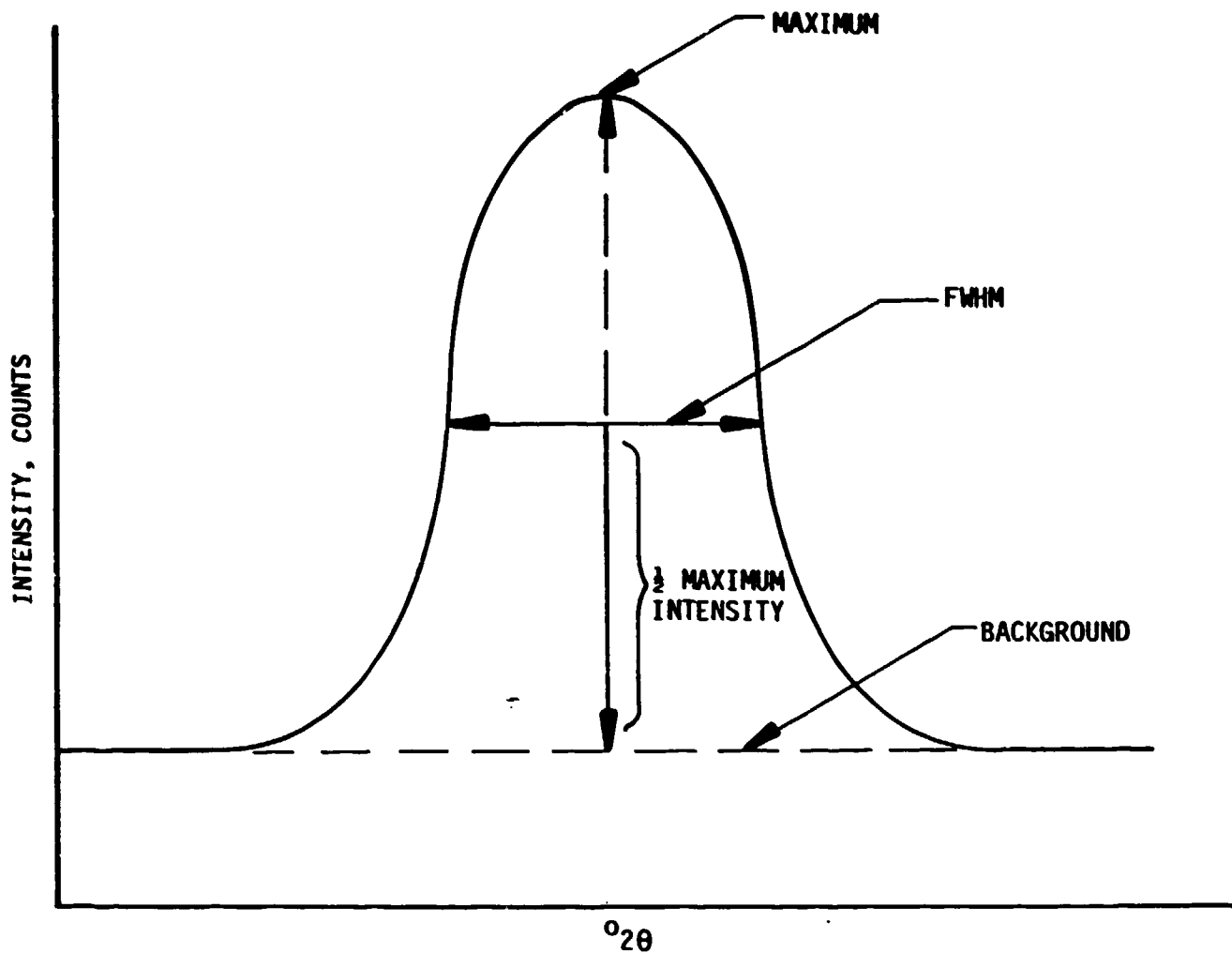
*Measurement made near edge of inner ring raceway.

diffraction peak full width at half the maximum intensity (FWHM) (Figure 3-10). The FWHM is an indication of the amount of cold working in the surface of the material.² From these measurements, the FWHM was consistently lower (less cold working) in the properly ground bearings than in the abusively ground bearings. The FWHM ranged from 4.6 to 4.8° 2 θ for the good bearings and from 5.1 to 5.8° 2 θ for the bad bearings, indicating a higher amount of cold working in the abusively ground bearings.

Another difference noted between the measurements made on the good and bad inner ring raceways was the d-spacing versus $\sin^2\psi$ plots. The plots for the good bearings were generally linear (Figure 3-11 is an example) while those for the bad bearings were nonlinear (Figures 3-12 and 3-13). The nonlinearity may be a result of measuring microstresses (short range stresses) instead of macrostresses (long range stresses). It is speculated that the abusive grinding process contributes to the nonlinearity of these plots.

3.2.3.2 Outer Ring Raceways (J-79 Only) - Stresses measured on the outer rings of the J-79 bearings (Table 3-4) showed different trends than those on the inner rings. First, measurements in the raceways of the good and bad outer rings resulted in the same stresses and FWHM. Stresses at the land were about twice as compressive for the bad outer raceway as for the good one. Measurements were also made around the O.D. circumference of these rings for comparison. Here, the

2. P. S. Prevey, "Diffraction Notes", Lambda Research, Inc., Cincinnati, Ohio, Volume 1, No. 1, Winter, 1987.



32 121A37

Figure 3-10
 Differences in the Diffraction Peak
 Full Width at Half the Maximum Intensity

d-SPACING vs. $\text{Sin}^2 \psi$

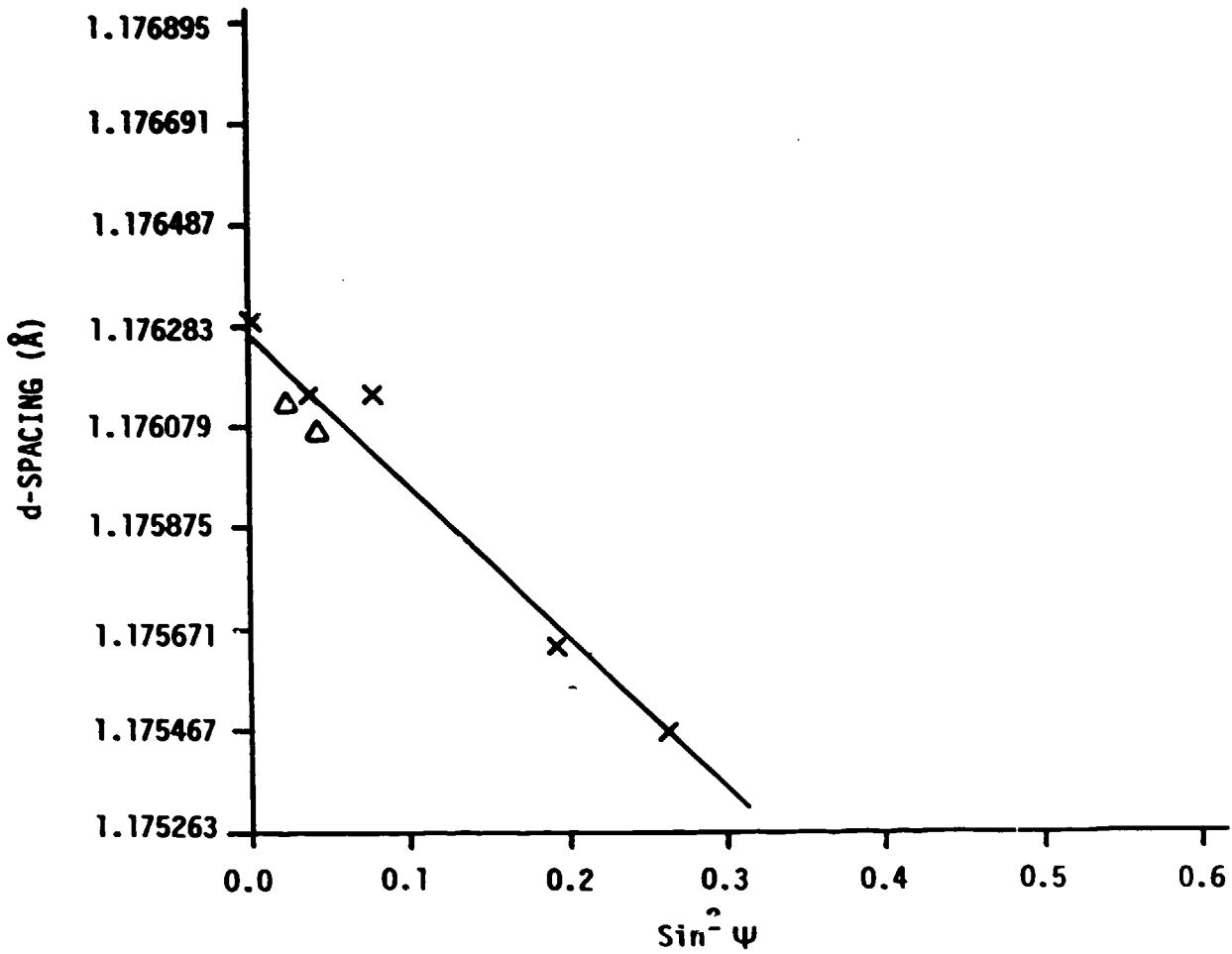


Figure 3-11
Linear Plot Associated with High Compressive Stresses
in Good Bearing

32121A21

d-SPACING vs. $\sin^2 \psi$

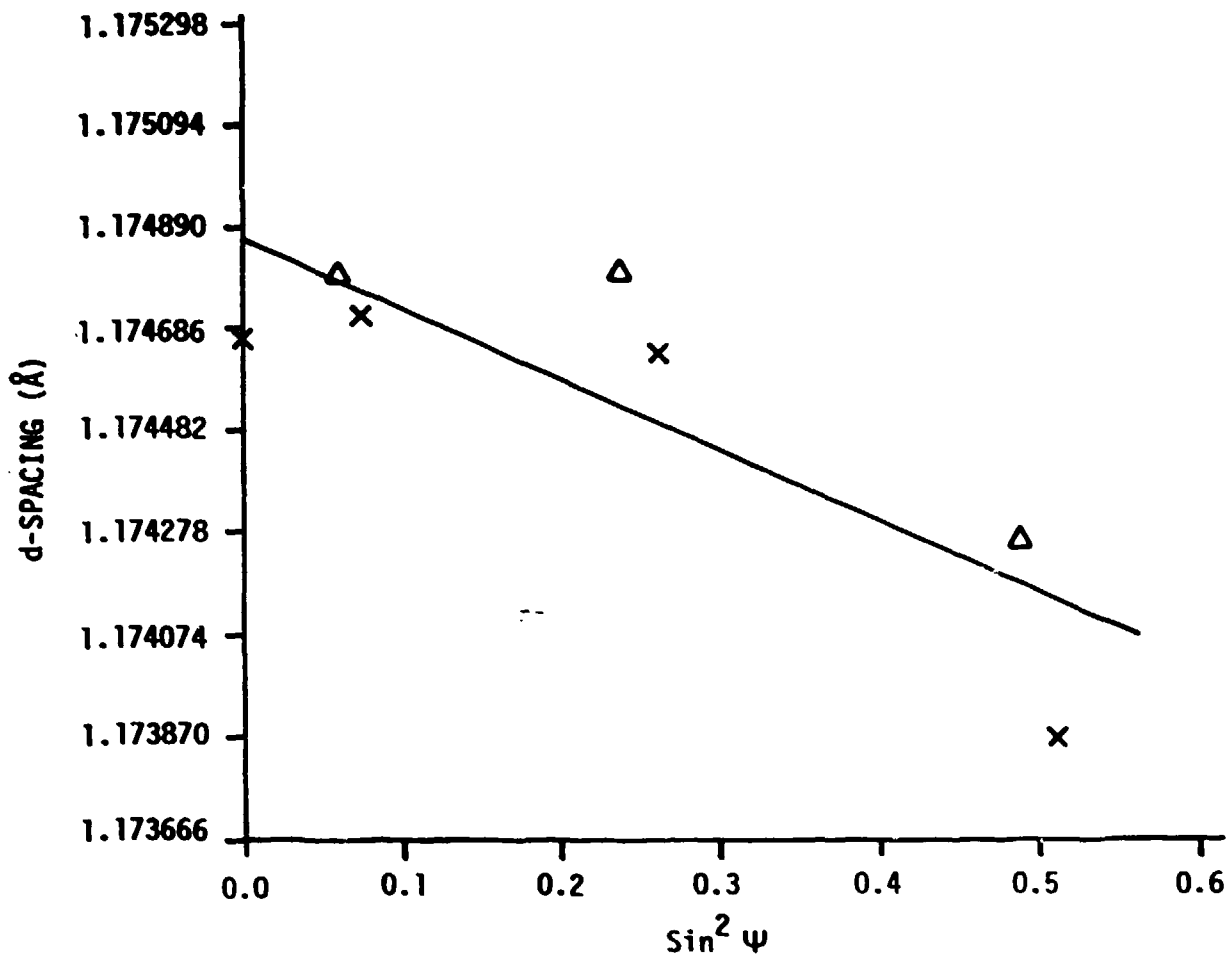


Figure 3-12
Non-Linear Plot of Low Compressive Stresses
in Bad Bearing

32121A19

d-SPACING vs. $\sin^2 \psi$

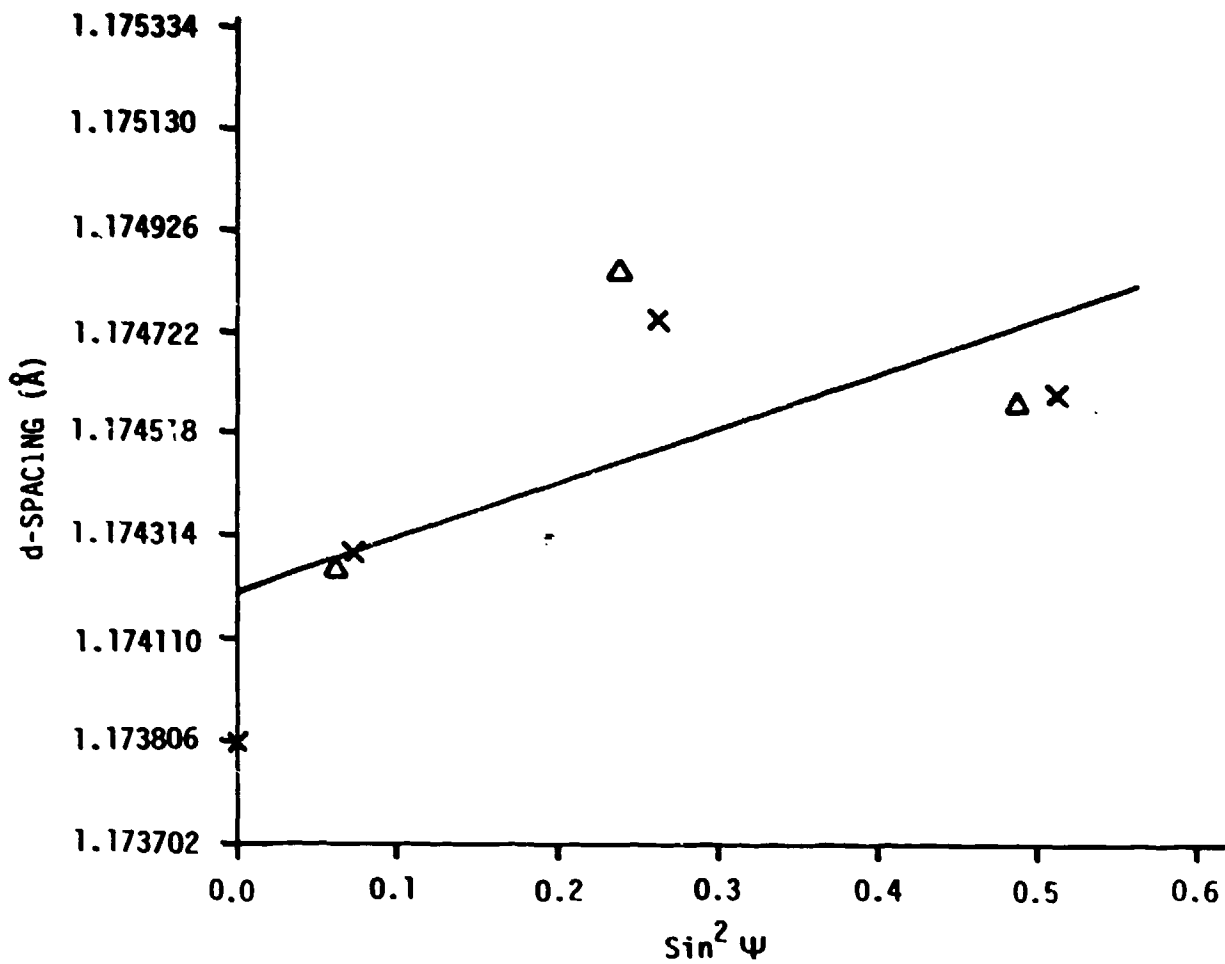


Figure 3-13
Non-Linear Plot of Tensile Stresses in Bad Bearing

32121A20

Table 3-4.

Residual Stresses on Outer Rings (J-79 Only)

Location	Good		Bad	
	Stress, ksi	FWHM, °2θ	Stress, ksi	FWHM, °2θ
Raceway	-63.1 ± 11.4	4.9	-54.1 ± 12.3	4.9
			-56.1 ± 45.4	5.1
			-59.9 ± 15.6	5.0
			-83.5 ± 12.4	4.8
			-64.2 ± 19.8	4.9
Land	-35.2 ± 9.3	3.9	-78.5 ± 23.3	4.9
O. D.	-70.5 ± 12.0	4.8	-29.0 ± 10.8	5.1
	-70.4 ± 12.0	4.8	-25.3 ± 9.5	5.2
	-77.3 ± 10.9	4.7	+17.8 ± 13.0	5.7
	-71.3 ± 11.9	4.7	+3.5 ± 11.7	5.4
			+22.4 ± 13.5	5.2

good ring had consistently compressive values (-70 to -77 ksi) and the bad ring had both tensile and compressive readings (+22 to -29 ksi). The FWHM at the O.D. surface of the bad bearing was larger than for the good bearing.

3.2.3.3 Comparison to Phase I Results - Data on raceways from the Phase I study had suggested that shear stresses (indicated by $\sin^2\psi$ splits) may be related to grinding burns. The Phase II work indicates that tensile or low compressive stresses are found on the bad bearing raceways, and high compressive stresses are found on the good raceways. The d-spacing versus $\sin^2\psi$ plots are linear or nonlinear and do not exhibit the $\sin^2\psi$ split associated with shear stresses. The collimated x-ray beam was smaller for the Phase II study. It was concluded that geometric effects from a large collimated x-ray beam and not shear stresses resulted in the $\sin^2\psi$ splits seen in the previous work.

3.2.3.4 Evaluation of the Effects of Etching - Stress measurements made after etching differed from the surface measurements. Recall that only the J-79 bearings were etched with the Tarasov's etchant. A stress measurement made in a dark axial striation in the light colored circumferential strip of the bad raceway was -6 ksi. This was the only compressive stress found in the inner ring of this bearing with one exception. Measurements on the mating surface between the split inner ring sections were -159, -168, and -178 ksi, suggesting that this surface was not representative of the raceway. Stresses in the light colored etched areas (+54 and +74 ksi) were similar to the surface stresses.

The stresses on the surface of the good bearing were consistently compressive, but this was not the case for the subsurface measurements. Etching with the Tarasov etchant for an unknown time (<1 minute) quickly discolored the surface and resulted in very low stresses (-10 to +4 ksi). Considering that this etchant should not remove more than 0.001" of material, it was questioned whether a stress gradient of this magnitude existed. The stress was then measured on the surface adjacent to the etched area. Once again the surface stress was compressive (-114 ksi). A series of etchings followed by stress measurements were performed in this adjacent area. This time the etching procedure was carefully controlled to insure that the etching time did not exceed 10 seconds per etch. This procedure resulted in a linear decrease in the compressive stress measured for the first five etching cycles (Figure 3-14). The etching procedure was repeated a total of seven times until the stresses were -23 to -25 ksi. A one-minute etch at a separate location resulted in a low stress of 4 ksi. These results led to speculation that the etchant at dwell times greater than 10 seconds may preferentially dissolve portions of the grain boundaries

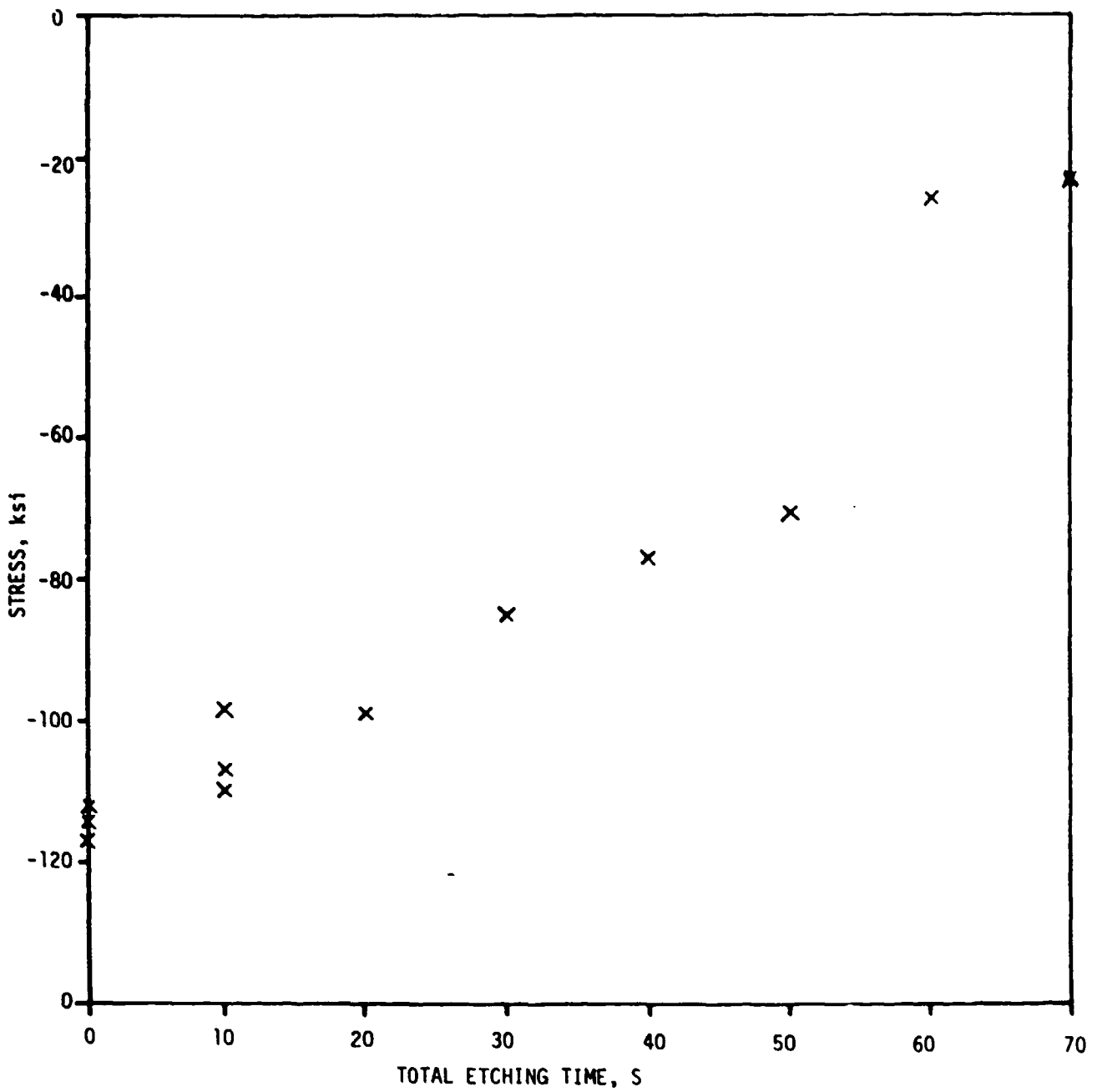


Figure 3-14
Residual Stress vs. Etching Time for Bearing Raceway J-79 (Good)

32121A03

around the surface grains. The areas that had been etched longer than 10 seconds at a time had a rougher texture than the other etched areas and lends credibility to this speculation. If portions of the grain boundaries were dissolved by the etchant, then the surface stress was artificially stress-free because the connective material necessary to support stresses was removed. Additionally, if high stress gradients really existed, then curved d-spacing versus $\sin^2\psi$ plots of the unetched surface would be expected.³ The d-spacing versus $\sin^2\psi$ plots were linear for the unetched measurements.

A section (<1 inch) of the good J-79 bearing inner ring was removed for scanning electron microscopy (SEM) of the etched and unetched surfaces. The intent of this investigation was to determine if the etchant had preferentially attacked the grain boundaries resulting in an artificially induced stress-free surface. The bearing raceway geometry made the examination difficult. The 700X photographs (Figures 3-15 and 3-16) are clear enough to show that the etching did not occur only at grain boundaries. It was not possible to estimate the amount of material removed by etching. Based on the SEM and the 10-second etching cycles, it is assumed that stress gradients do exist in the raceway. The gradient cannot be quantified from these data since the amount of material removed could not be measured by means employed during the Phase II work.

3. I. C. Noyan, "Effect of Gradients in Multi-Axial Stress States on Residual Stress Measurements with X-Rays," Graduate Student and Research Assistant, Department of Materials and Engineering, The Technological Institute, Northwestern University, Evanston, Illinois.

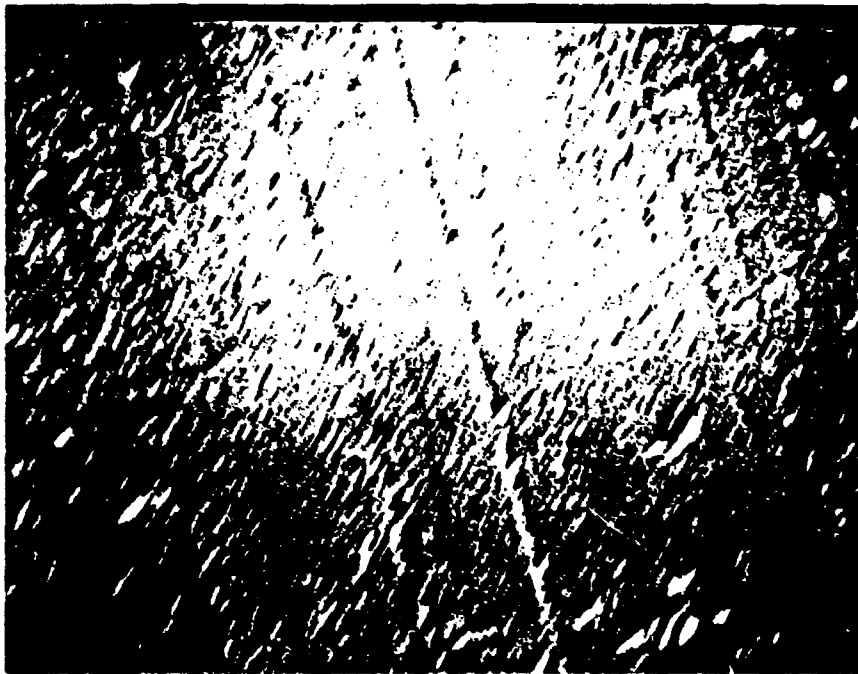


Figure 3-15
Photograph of Unetched Surface on
Bearing Inner Ring Raceway

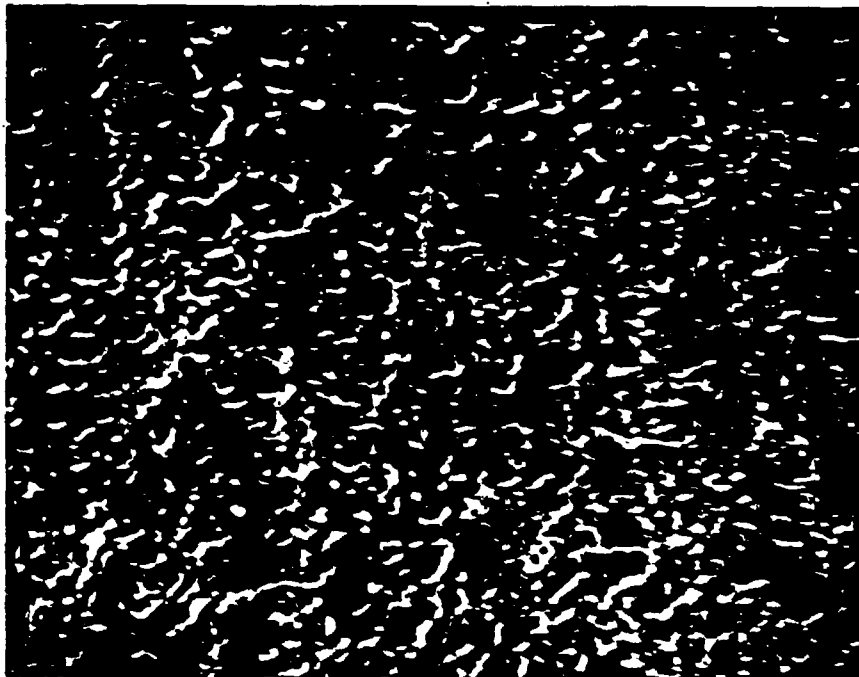


Figure 3-16
Photograph of Etched Surface on
Bearing Inner Ring Raceway

The 10-second etch depth profiling was also performed on the mating surface between the split inner ring sections of the bad J-79 bearing. Recall that the surface measurements on the area of the bad inner ring were similar to the raceway measurements on the good bearing. The depth profile in Figure 3-17 follows the same trend as Figure 3-14. Again, this indicates that the mating surface measurements cannot be used to distinguish good from bad bearings.

3.2.4 Conclusions

Abusively ground bearings can be distinguished from properly ground bearings by measuring the stresses on the inner raceways at the point of rolling element contact. The properly ground bearing raceways have high compressive stresses, linear d-spacing versus $\sin^2\psi$ plots and a smaller FWHM. The abusively ground bearing raceways have tensile or low compressive stresses, nonlinear d-spacing versus $\sin^2\psi$ plots and a larger FWHM. It was concluded that these differences were directly related to the increased cold working imparted to the surface during abusive grinding.

Shear stresses as indicated by $\sin^2\psi$ splits were not found on either good or bad bearings. Splits seen during the Phase I study were attributed to the geometric effects of the large collimator used.

High stress gradients probably exist in the surface of the inner raceways. The stress gradients could not be quantified, however, the stresses decreased linearly when the sample was etched under controlled conditions.

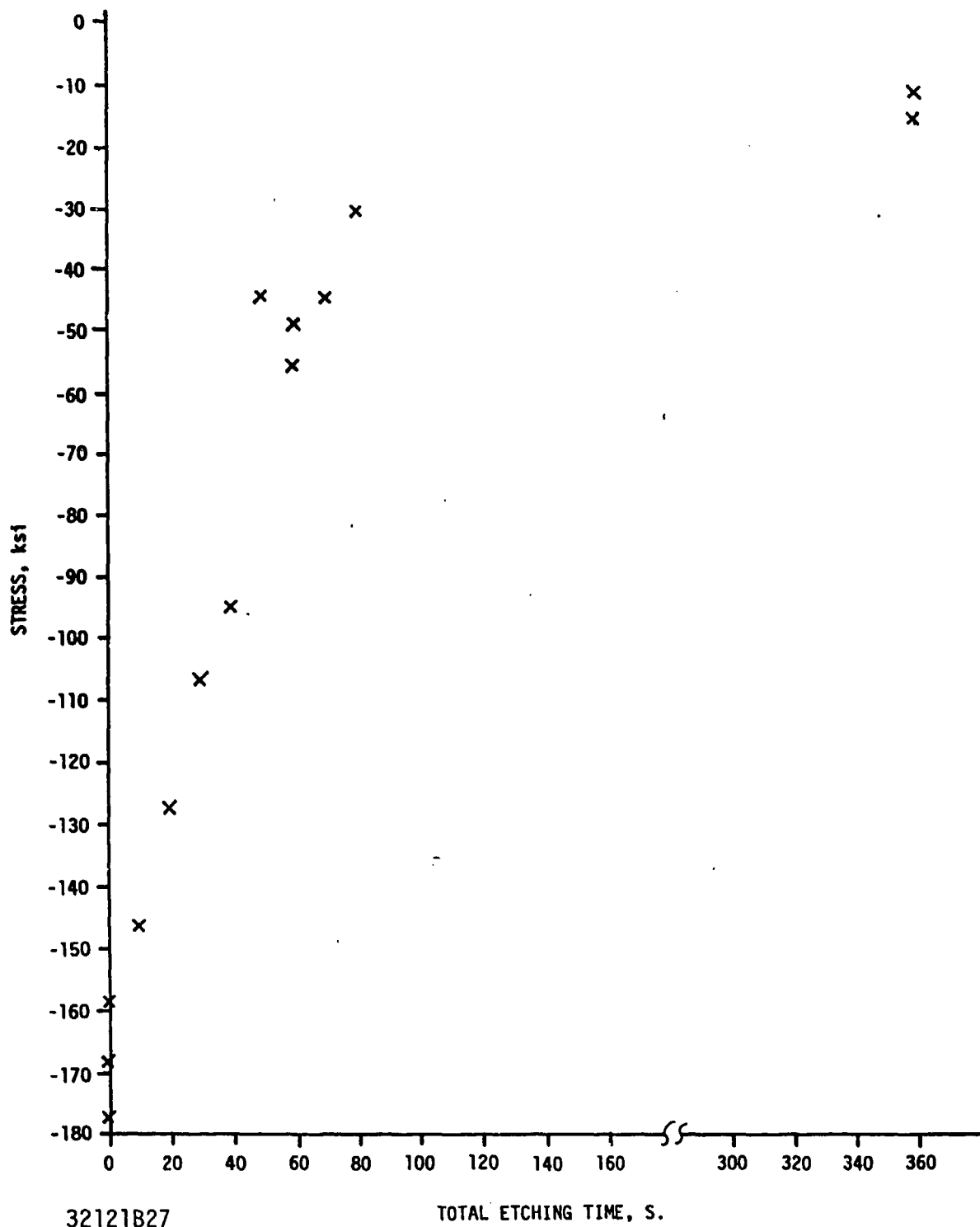


Figure 3-17
 Residual Stress vs. Etching Time for Bearing Race J-79
 (Bad) Mating Surface Between the Split Inner Ring Section

3.3 COMPRESSOR AND FAN BLADES

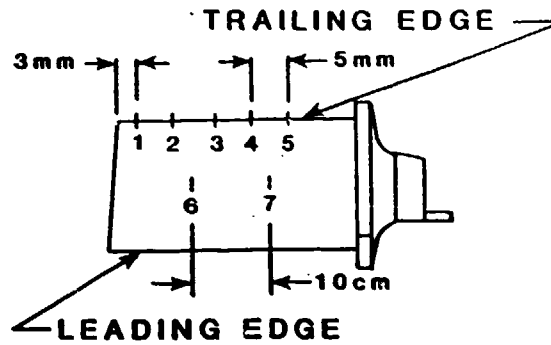
Eight J-52 compressor blades and four TF-30 fan blades were analyzed for residual stresses. The blades represented several different processing stages and conditions. The purpose of this work was to quantify and compare the stress levels for each blade.

3.3.1 Blade Description and Measurement

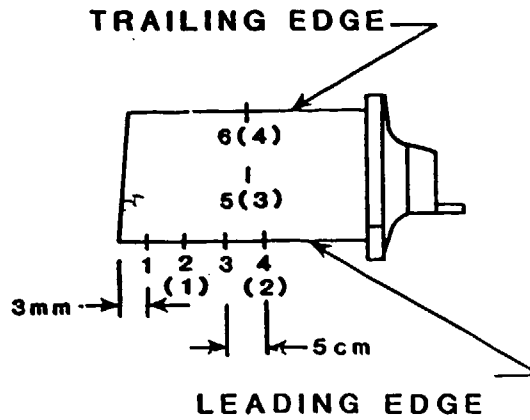
Measurements were made on both surfaces of the compressor blades and the top (convex) surface of the fan blades. All of the blades were made of Ti-6-4, therefore, measurement parameters were similar. Measurement locations are shown in Figures 3-18 and 3-19. The compressor blades were numbered 1, 2, 3, 4, A, B, C and D. Blades 1 and 2 had been in service, and Blade 1 was damaged by impact with an object, while Blade 2 was undamaged. Blades 3 and 4 were weld repaired blades with no subsequent service. Blades A, B and C had been welded and blended which represented an intermediate processing step in normal weld repair. Blade D had been glass beaded after the weld and blend stage. Of the four fan blades, two had been in service and received damage by impact from an object (EZ6381 H95 and KH9483 H85). One of the blades was new (KL0990) and the remaining blade (KJ1788 H87) had been electron beam welded.

3.3.2 Results and Discussion

The results for the compressor blades are tabulated in Tables 3-5 through 3-12. All stresses are compressive. A comparison of the compressor blade data shows low compressive stresses on the used blades (typically less than -60 ksi) and high compressive stresses on the weld repaired blades (typically greater than -90 ksi). The blades that were welded and blended (A, B and C) exhibited low



**J52 COMPRESSOR BLADES 'A'-'D'
MEASUREMENT LOCATIONS**



(PARENTHESES INDICATE
BOTTOM LOCATIONS)

**J52 COMPRESSOR BLADES '1'-'4'
MEASUREMENT LOCATIONS**

32121A41

Figure 3-18

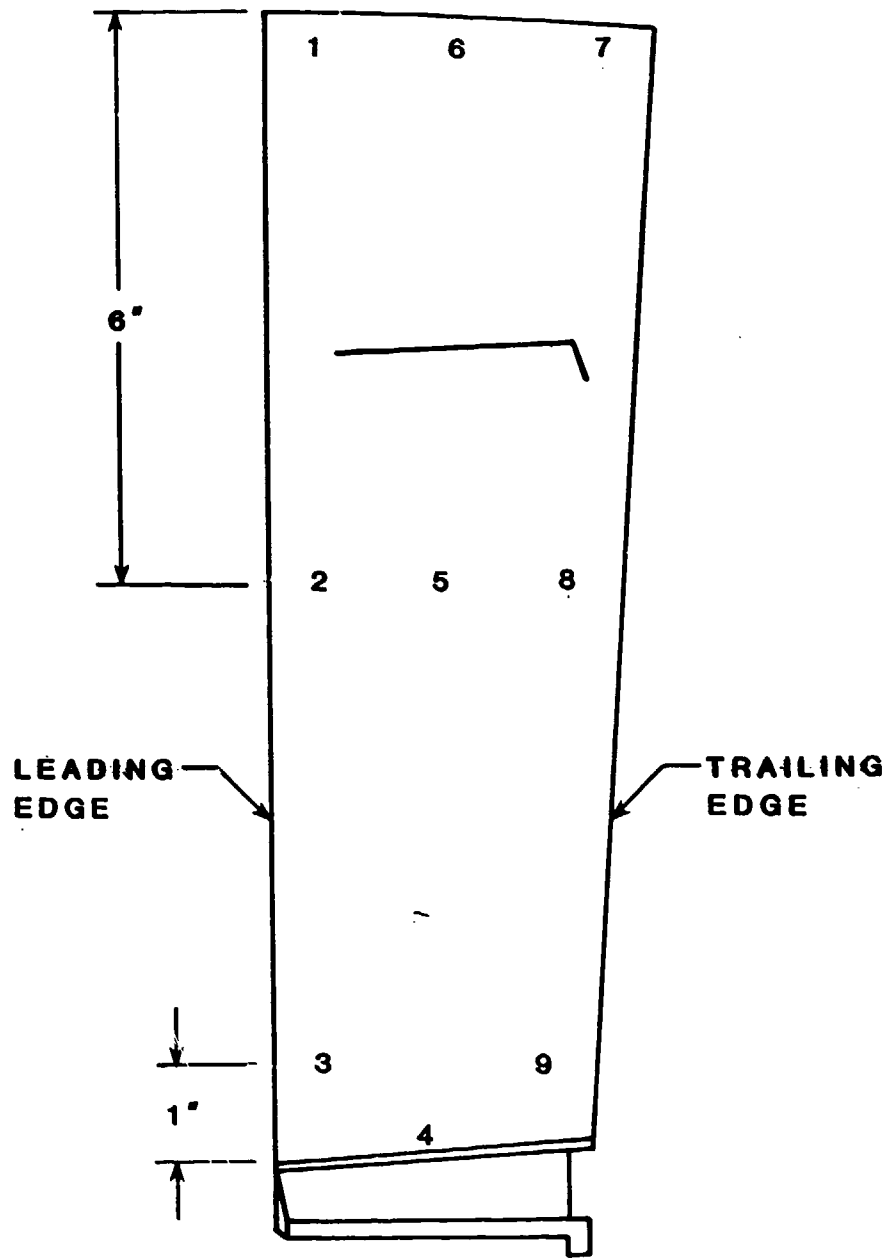


Figure 3-19
 TF30 FAN BLADE MEASUREMENT LOCATIONS

Table 3-5.

**Residual Stress Summary for J-52 Compressor Blade 1
(Impact Damage Near Position 1)**

<u>Location</u>		<u>Residual Stress (ksi)</u>	
		<u>Lateral</u>	<u>Longitudinal</u>
TOP			
Trailing Edge	Position 1	-15.0 ± 3.1	-37.3 ± 3.4
	Position 2	-46.4 ± 5.4	-37.6 ± 4.2
	Position 3	-59.6 ± 3.3	-51.4 ± 4.0
	Position 4	-68.4 ± 4.1	-53.2 ± 9.7
	Position 5	-47.2 ± 4.2	N/A
Center	Position 6	-57.0 ± 4.2	-59.8 ± 4.2
	Position 7	-53.4 ± 3.6	-57.4 ± 7.9
BOTTOM			
Trailing Edge	Position 1	-45.6 ± 4.5	-48.9 ± 3.4
	Position 2	-61.0 ± 9.2	-58.0 ± 6.5
	Position 3	-58.3 ± 12.4	-64.7 ± 4.9
	Position 4	-56.2 ± 12.2	-62.4 ± 5.8
	Position 5	-58.4 ± 8.9	-60.4 ± 4.4
Center	Position 6	-42.6 ± 4.5	-46.4 ± 4.9
	Position 7	-43.2 ± 4.9	-63.7 ± 4.0

Table 3-6.

**Residual Stress Summary for J-52 Compressor Blade 2
(Used)**

<u>Location</u>		<u>Residual Stress (ksi)</u>	
		<u>Lateral</u>	<u>Longitudinal</u>
TOP			
Trailing Edge	Position 1	-19.1 ± 6.3	-22.5 ± 5.4
	Position 2	-27.5 ± 3.2	-24.0 ± 5.6
	Position 3	-21.2 ± 5.3	-25.0 ± 4.7
	Position 4	-21.0 ± 7.1	N/A
	Position 5	-23.4 ± 6.0	-32.6 ± 6.9
Center	Position 6	-40.0 ± 6.8	-28.8 ± 5.6
	Position 7	-33.6 ± 4.9	-32.1 ± 5.6
BOTTOM			
Trailing Edge	Position 1	-69.4 ± 9.1	-46.8 ± 4.5
	Position 2	-60.4 ± 11.9	-55.2 ± 6.6
	Position 3	-52.7 ± 10.4	-42.0 ± 11.0
Center	Position 4	-49.7 ± 4.6	-44.1 ± 7.2
	Position 5	-43.3 ± 4.6	-43.9 ± 6.7

Table 3-7.

Residual Stress Summary for J-52 Compressor Blade 3
(Weld Repaired)

	<u>Location</u>	Residual Stress (ksi)	
		<u>Lateral</u>	<u>Longitudinal</u>
TOP			
Trailing Edge	Position 1	-106.0 ± 15.7	-88.7 ± 9.3
	Position 2	-105.0 ± 7.8	-98.5 ± 7.2
	Position 3	-90.5 ± 7.8	-91.9 ± 6.7
	Position 4	-90.5 ± 10.9	-95.7 ± 5.8
	Position 5	-79.4 ± 11.3	-92.4 ± 18.0
Center	Position 6	-91.5 ± 9.4	-98.0 ± 9.9
	Position 7	-107.5 ± 7.8	-93.8 ± 7.5
BOTTOM			
Trailing Edge	Position 1	-140.8 ± 16.1	-119.2 ± 7.9
	Position 2	-120.2 ± 38.9	-95.9 ± 13.0
	Position 3	-117.6 ± 17.2	-97.3 ± 8.2
	Position 4	-112.1 ± 16.8	-94.9 ± 11.8
	Position 5	-115.2 ± 12.2	-111.0 ± 8.3
Center	Position 6	-86.5 ± 12.9	-109.3 ± 11.2
	Position 7	-96.4 ± 13.2	-90.6 ± 9.6

Table 3-8.

Residual Stress Summary for J-52 Compressor Blade 4
(Weld Repaired)

	<u>Location</u>	Residual Stress (ksi)	
		<u>Lateral</u>	<u>Longitudinal</u>
TOP			
Trailing Edge	Position 1	-91.6 ± 8.0	-99.0 ± 12.1
	Position 2	-100.3 ± 10.9	-117.4 ± 7.6
	Position 3	-81.2 ± 21.8	-92.9 ± 8.4
	Position 4	-110.0 ± 9.7	-97.8 ± 17.1
	Position 5	-68.2 ± 5.5	N/A
Center	Position 6	-92.1 ± 12.1	-103.2 ± 8.6
	Position 7	-93.5 ± 11.0	-103.5 ± 11.3
BOTTOM			
Trailing Edge	Position 1	-106.1 ± 15.6	-109.9 ± 12.8
	Position 2	-123.3 ± 15.3	-109.4 ± 8.4
	Position 3	-105.5 ± 7.5	-109.8 ± 7.0
	Position 4	-120.9 ± 9.8	-88.2 ± 16.8
	Position 5	-92.2 ± 12.1	-92.7 ± 10.5
Center	Position 6	-115.2 ± 8.6	-104.3 ± 7.4
	Position 7	-86.6 ± 8.2	-124.6 ± 6.8

Table 3-9.

Summary of Measurements
on Welded and Blended J-52 Compressor Blade 'A'

<u>Location</u>		Residual Stress (ksi)	
		<u>Lateral</u>	<u>Longitudinal</u>
TOP OF BLADE			
Leading Edge	1	-11.3 ± 5.6	-8.9 ± 4.8
	2	-13.4 ± 5.2	-3.6 ± 5.1
	3	-57.6 ± 8.2	-56.8 ± 6.1
	4	-94.3 ± 11.2	-93.2 ± 7.4
	5	-116.1 ± 12.3	N/A
Center	6	-110.8 ± 8.4	-86.4 ± 28.2
Trailing Edge	7	-108.7 ± 5.7	-87.7 ± 7.5
BOTTOM OF BLADE			
Leading Edge	1	-19.1 ± 8.8	-9.9 ± 5.4
	2	-132.5 ± 13.7	-108.0 ± 9.4
Center	3	-112.9 ± 9.0	-112.9 ± 9.0
Trailing Edge	4	-109.6 ± 8.4	-109.6 ± 8.4

Table 3-10.

Summary of Measurements
on Welded and Blended J-52 Compressor Blade 'B'

<u>Location</u>		Residual Stress (ksi)	
		<u>Lateral</u>	<u>Longitudinal</u>
TOP OF BLADE			
Leading Edge	1	-38.4 ± 12.0	-27.8 ± 5.3
	2	-31.1 ± 7.1	-16.2 ± 7.0
	3	-86.9 ± 9.7	-59.4 ± 5.1
	4	-105.9 ± 18.6	-102.1 ± 11.0
	5	-118.8 ± 9.2	-116.2 ± 7.0
Center	6	-123.7 ± 8.6	-104.5 ± 13.5
Trailing Edge			
BOTTOM OF BLADE			
Leading Edge	1	-12.7 ± 5.7	-4.5 ± 5.5
	2	-113.1 ± 10.1	-130.2 ± 18.6
Center	3	-101.6 ± 7.5	-106.0 ± 14.3
Trailing Edge	4	-102.2 ± 12.4	-101.5 ± 9.6

Table 3-11.

Summary of Measurements
on Welded and Blended J-52 Compressor Blade 'C'

<u>Location</u>		Residual Stress (ksi)		
		<u>Lateral</u>	<u>Longitudinal</u>	
TOP OF BLADE				
Leading Edge	1	-17.0 ± 8.1	-12.7 ± 7.9	
	2	-26.3 ± 7.2	-19.7 ± 9.1	
	3	-69.6 ± 6.8	-45.1 ± 6.6	
	4	-99.2 ± 13.5	-96.0 ± 7.0	
Center	5	-99.9 ± 8.3	-108.9 ± 7.8	
	Trailing Edge	6	-98.5 ± 7.9	-94.8 ± 7.5
		7	-92.9 ± 8.0	-96.5 ± 7.3
BOTTOM OF BLADE				
Leading Edge	1	-16.6 ± 5.9	-11.7 ± 7.1	
Center	2	-106.6 ± 13.7	-111.2 ± 7.6	
Trailing Edge	3	-78.2 ± 6.1	-85.1 ± 11.6	

Table 3-12.

Summary of Measurements
on Welded and Blended J-52 Compressor Blade 'D'
(After Glass Beading)

<u>Location</u>		Residual Stress (ksi)		
		<u>Lateral</u>	<u>Longitudinal</u>	
TOP OF BLADE				
Leading Edge	1	-120.7 ± 15.8	-120.9 ± 20.2	
	2	-123.2 ± 19.7	-123.1 ± 12.4	
	3	-129.7 ± 43.3	-126.0 ± 10.4	
	4	-125.4 ± 9.9	-118.7 ± 26.7	
Center	Trailing Edge	5	-99.8 ± 20.6	-129.4 ± 12.2
		6	-132.0 ± 24.8	-137.8 ± 9.8
	7	-138.1 ± 8.7	-110.9 ± 17.7	
BOTTOM OF BLADE				
Leading Edge	1	-209.1 ± 35.0	-116.7 ± 10.3	
Center	2	-123.1 ± 15.7	-111.6 ± 7.9	
Trailing Edge	3	-106.7 ± 11.3	-117.1 ± 8.2	

compressive stresses in the welded and blended region. Outside this region, the stresses were typically -100 ksi. Blade D which had been glass beaded after welding and blending had the highest overall compressive stresses (-120 ksi).

Trends in these data suggest that compressive residual stresses imparted to the surface by beading and peening operations fade during blade service. The history of the used blades was not available; therefore, it is not possible to correlate the reduction in compressive stresses with engine run time.

The high compressive stresses seen after glass beading were expected. Previous experience with titanium alloys and conversations with Ken Fizer of NARF - Norfolk indicate that operations appearing less severe than full fledged shot peening can actually produce higher compressive surface stresses. Furthermore, these stresses are superficial and fade rapidly as a function of depth into the surface. The significance of superficial high compressive stresses in compressor blades is not known.

Stresses in the fan blades (Table 3-13) were relatively uniform at all measurement locations for all blades with a range of about -80 to -110 ksi. No significant difference was seen between the blades. Position 1 (near tip at leading edge) for the new blade was more compressive than the same position for the other blades. Other than that, there was no significant difference between blades at all other measurement locations.

Table 3-13.

Summary of Measurements
on TF-30 Fan Blades

Longitudinal Residual Stress (ksi)

<u>Location</u>	<u>EZ6381 H95 (used)</u>	<u>KH9483 H85 (used)</u>	<u>KJ1788 H87 (EB Welded)</u>	<u>KL0990 New</u>
1	-69.6 ± 8.5	-87.9 ± 26.3	-77.9 ± 10.7	-109.3 ± 6.1
2	-83.7 ± 8.8	-84.6 ± 13.0	-86.2 ± 7.7	-87.0 ± 5.4
3	-80.9 ± 11.8	-103.5 ± 8.4	-95.1 ± 8.3	-104.2 ± 6.5
4	-84.5 ± 6.8	-116.8 ± 33.6	-103.4 ± 11.5	-92.6 ± 5.5
5	-91.9 ± 4.5	-94.7 ± 24.8	-95.6 ± 7.6	-111.8 ± 11.3
6	-73.6 ± 7.3	-96.8 ± 12.4	-95.6 ± 7.4	-98.4 ± 6.8
7	N/A	N/A	N/A	-99.0 ± 6.8
8	N/A	N/A	N/A	-92.6 ± 4.5
9	N/A	N/A	N/A	-105.4 ± 6.8

3.3.3 Conclusions

The used compressor blades exhibited a fading of the compressive stresses which was associated with service life. Glass beading operations leave the top surface layer in high compressive stress. The effect of superficial high compressive stresses on blade life is unknown. Also, there was no significant difference in the residual stress state of the fan blades.

3.4 P-3 PROPELLER HUB MEASUREMENTS

3.4.1 Introduction

Residual stress measurements were made on an intact propeller hub (7076 aluminum) and on a hub section which were supplied by NARF - Alameda. The propeller had been removed from the intact hub. Both samples had cracks that initiated on an internal thread surface. The sectioned piece was about 2 1/2" x 2 1/4" x 3/8" and the sectioning occurred at a screw hole where crack indications had been found. The measurement surface (Figure 3-20) for this sectioned piece had been metallurgically prepared, i.e., polished and etched.

Measurements were made on the top surface of the intact hub (Figure 3-21) at the screw holes and at a location between a screw hole and a bolt hole. The purpose of these measurements was to quantify the stresses and determine if a correlation existed between the stress levels and cracking in the threads of the screw hole.

3.4.2 Results

The residual stresses in the sectioned hub are shown in Table 3-14 and in the intact hub are shown in Table 3-15. The stresses in the sectioned piece were essentially zero. This result was to be expected since the sample had been polished and etched. The etching process generally relieves surface residual stresses.

Measurements on the intact hub were compressive and relatively uniform at all measurement locations. These data suggest that the stress level at the top

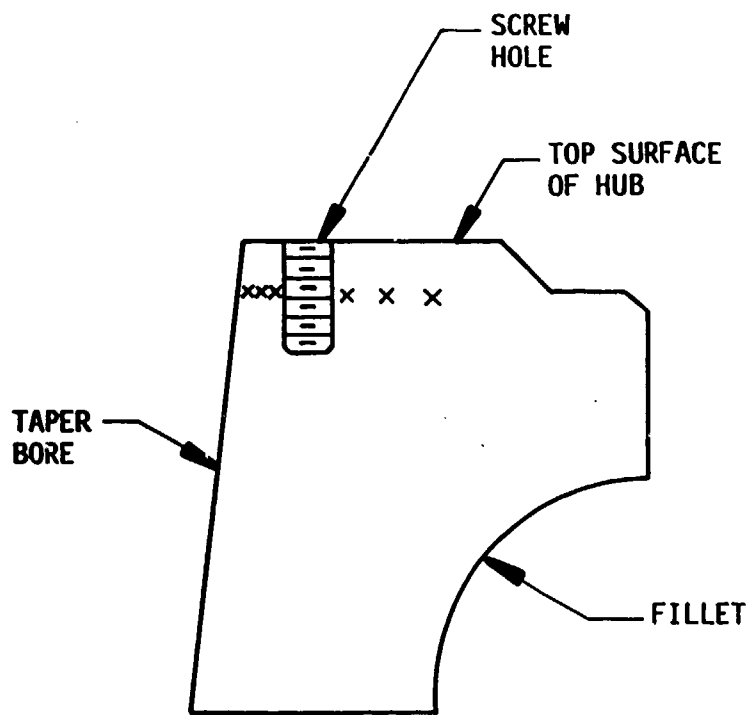


Figure 3-20
P-3 PROPELLER HUB SECTION.

32121A42

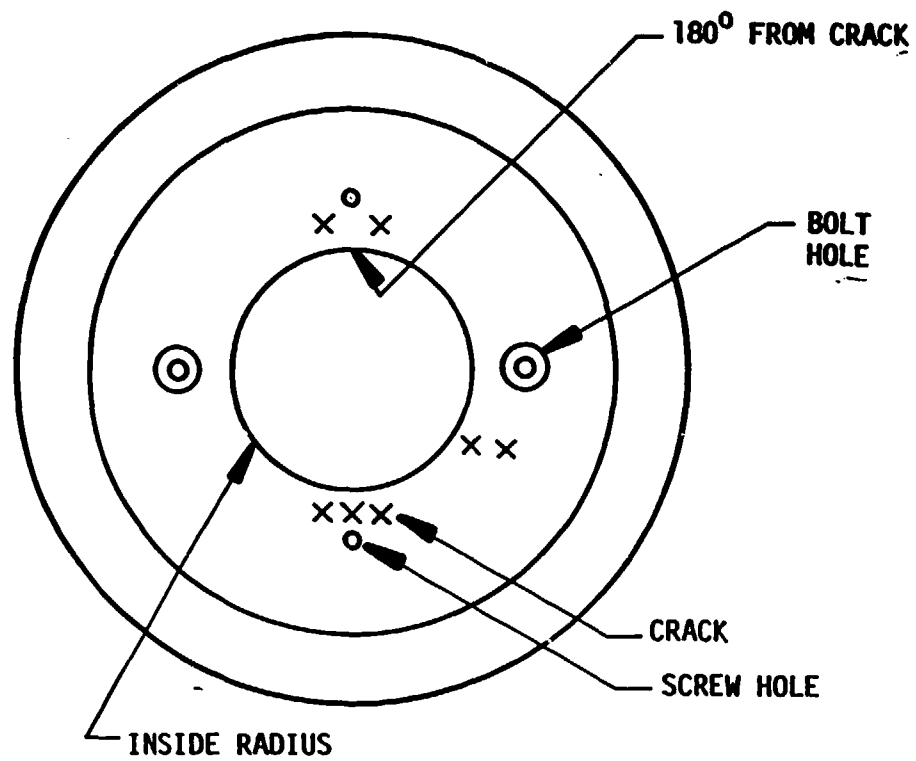


Figure 3-21
TOP VIEW OF P-3 PROPELLER HUB

32121A43

Table 3-14.

Summary of Measurements
on P-3 Propeller Hub

<u>Location Description</u>	Residual Stress (ksi)	
	<u>Left Side of Screw Hole</u>	<u>Right Side of Screw Hole</u>
Next to Screw Hole	2.5 ± 6.1	1.0 ± 2.3
More Distant from Screw Hole	7.3 ± 3.8	0.0 ± 2.2
Most Distant from Screw Hole	8.7 ± 4.2	-0.2 ± 1.6

Table 3-15.

Summary of Measurements
on P-3 Propeller Hub

<u>Location Description</u>	Residual Stress (ksi)		
	<u>Left Edge of Screw Hole</u>	<u>Right Edge of Screw Hole</u>	<u>Between Screw and Bolt Holes</u>
4 mm from inside radius			
hoop	-24.9 ± 4.4	-23.8 ± 3.3	-26.7 ± 2.8
radial	-29.4 ± 4.2	-20.7 ± 2.4	-23.9 ± 2.2
4 mm from inside radius at crack			
radial	-18.6 ± 0.7	N/A	N/A
10 mm from inside radius			
hoop	N/A	N/A	-22.7 ± 3.1
radial	N/A	N/A	-18.6 ± 0.7
4 mm from inside radius 180° from crack			
hoop	-15.9 ± 1.3	-21.2 ± 1.2	N/A
radial	-23.7 ± 2.7	-23.8 ± 1.1	N/A

surface was uniform and unaffected by cracking at the internal threaded surface. An uncracked hub was unavailable for comparison, however, only one of the screw holes in the intact hub had cracking. It was assumed that the stresses around the uncracked screw hole are representative of stresses in an uncracked hub.

3.4.3 Conclusions

The stresses in the sectioned pieces were affected by the metallurgical preparation. Stresses in this section at the crack location were essentially zero. Stresses in the intact hub on the top surface were compressive and uniform at cracked and uncracked locations. Thus, surface residual stress analysis at the top surface of the hub may not indicate the stresses that result in cracking in the internal threaded region.

3.5 NICKEL-PLATING STUDY

3.5.1 Study of Nickel-Plating Residual Stress Measurements

3.5.1.1 Introduction - The nickel-plating study is to determine if and how residual stress can be used to determine whether the process parameters are satisfactory. During Phase I, the Company received test coupons from two different sets of nickel-plating process parameters and some H-3 helicopter camshafts from the NARF - Pensacola. The data obtained from the H-3 camshafts produced perplexing results due to $\sin^2\psi$ splitting and non-linear d-spacing versus $\sin^2\psi$ plots. High compressive surface stresses were also found.

As a result of findings during the Phase I examination, an intensive study of residual stresses in nickel-plating was undertaken during the Phase II program. Specifically, four phenomena were singled out for study: an anomalous $\sin^2\psi$ split from Cr K α radiation, s-shaped d-spacing versus $\sin^2\psi$ plots for Cr K α , Cu K α , and Co K α radiations, a $\sin^2\psi$ split for the Co K α radiation; and high compressive stress values on one of the nickel-plated camshafts.

An additional objective of the Phase II nickel-plating study was to understand the underlying x-ray physics involved in x-ray stress analysis of nickel-plated components and thereby address the above noted phenomena. For this study, a flat nickel-plated coupon was used to eliminate any geometric factors that would be present in using cylindrical camshafts. After numerous measurements were made on the coupon, a camshaft was measured using knowledge gained from the flat plate study. This section of the report discusses the measurement philosophy, the results of the measurements, and the important lessons learned from this exercise.

3.5.1.2 Flat Plate Sample

Hard Plating - A nickel-plated coupon (3"x2"x1/8"), plated under standard camshaft plating conditions, was selected for the first part of this study. These plating conditions generally result in a hardness of 50 to 51 Rockwell C. The first experiment was designed to determine the cause of the s-shaped d-spacing versus $\sin^2\psi$ plots. These s-shaped plots are typically associated with a large grain size and/or preferred orientation of the grains in the material. All three radiation wavelengths used in the Phase I study were used to determine stresses to different depths in the material. Different radiations due to their different wavelengths measure the stresses to different depths into the surface. There were indications of stress gradients in the Phase I study. The current study was made to determine if there was an optimum radiation for nickel-plating.

Ten non-overlapping locations (Figure 3-22) were measured on the coupon in the flat position with three radiation wavelengths. These ten locations were measured again with the sample inclined at an arbitrarily selected angle of 27° to the horizontal, and the measurements were repeated a third time with the coupon inclined at a symmetric angle of -27° to the horizontal (Figure 3-23). The inclinations were perpendicular to the direction of stress measured. Measurements were performed at the inclinations to compare the intensities of the diffraction peaks from the inclined runs to those from the flat position. These data were used to check for preferred orientation of the grains. The stress results are listed in Table 3-16. The stresses were relatively low in every case, but they varied from about -14 ksi to about +14 ksi. The variation

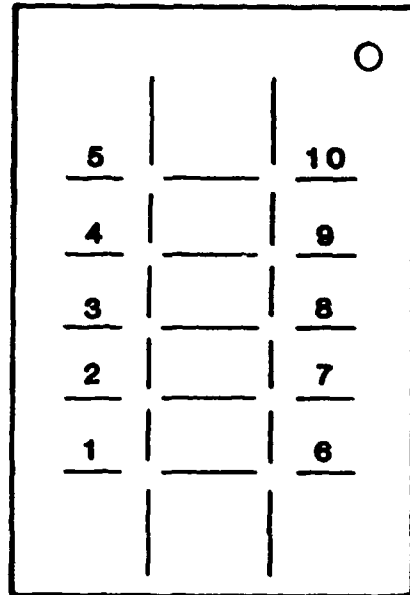
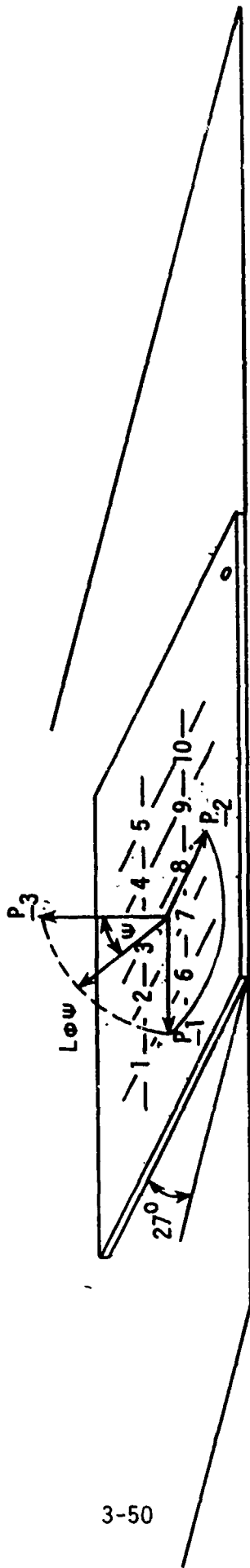


Figure 3-22
Ten Residual Stress Measurements
on Flat Plate Sample

92121A02



3-50

32121A04

Figure 3-23
 Measurement at Angle of 27° to Horizontal
 and Symmetric Angle of -27° to Horizontal

Table 3-16.

Residual Stresses for the Flat Plate Sample
(Hard Plating)

Copper X-ray Position	Horizontal (0°) Stress, ksi	27° Stress, ksi	-27° Stress, ksi
1	-7.5 ± 7.9	5.0 ± 5.7	-2.6 ± 5.6
2	7.1 ± 4.6	-0.6 ± 4.8	-1.6 ± 5.2
3	7.3 ± 3.4	-1.9 ± 4.0	0.7 ± 6.2
4	5.5 ± 5.3	0.3 ± 6.5	2.6 ± 6.4
5	5.4 ± 3.5	2.9 ± 4.8	-1.3 ± 5.8
6	2.3 ± 4.7	-4.1 ± 8.4	-4.0 ± 5.8
7	13.0 ± 4.4	5.9 ± 5.4	6.9 ± 4.6
8	4.1 ± 4.2	5.7 ± 5.2	9.9 ± 5.6
9	7.8 ± 3.6	5.4 ± 4.7	2.5 ± 4.5
10	12.7 ± 5.8	13.6 ± 6.3	1.9 ± 5.4
AGGREGATE	7.3 ± 3.2	4.4 ± 2.1	2.3 ± 2.0

Cobalt X-ray Position	Horizontal (0°) Stress, ksi	27° Stress, ksi	-27° Stress, ksi
1	3.1 ± 5.6	2.4 ± 6.2	-0.3 ± 4.6
2	1.7 ± 5.2	3.2 ± 4.5	-2.5 ± 5.0
3	0.0 ± 4.8	14.6 ± 10.5	-4.5 ± 4.2
4	-1.0 ± 5.1	-0.1 ± 5.5	-7.3 ± 4.7
5	-7.0 ± 4.8	4.2 ± 5.6	-6.6 ± 5.7
6	-3.4 ± 5.3	1.5 ± 6.8	-5.2 ± 5.0
7	0.9 ± 4.9	5.3 ± 4.6	-1.2 ± 7.2
8	7.3 ± 5.7	7.6 ± 6.3	-3.3 ± 4.8
9	-1.0 ± 6.5	4.0 ± 6.4	-5.5 ± 6.3
10	-9.8 ± 5.1	0.6 ± 5.0	-4.5 ± 5.2
AGGREGATE	-0.2 ± 2.2	4.2 ± 3.3	-3.1 ± 2.3

Chromium X-ray Position	Horizontal (0°) Stress, ksi	27° Stress, ksi	-27° Stress, ksi
1	-14.0 ± 17.3	6.6 ± 12.2	-1.7 ± 8.8
2	-1.4 ± 13.0	5.8 ± 13.2	-1.0 ± 13.7
3	0.3 ± 13.3	4.4 ± 9.3	0.7 ± 8.5
4	4.9 ± 10.4	6.3 ± 8.1	1.6 ± 12.4
5	-7.9 ± 15.1	7.7 ± 10.6	1.2 ± 10.6
6	-8.0 ± 25.7	7.0 ± 10.2	3.2 ± 12.9
7	-3.3 ± 12.0	-0.3 ± 8.3	4.1 ± 11.6
8	3.7 ± 11.2	5.3 ± 9.8	6.2 ± 10.4
9	5.0 ± 11.5	9.7 ± 10.7	3.5 ± 16.0
10	-1.2 ± 10.9	1.0 ± 12.6	1.1 ± 13.4
AGGREGATE	1.1 ± 8.3	5.2 ± 8.8	2.0 ± 10.0

did not appear to be related to the target radiation used, nor was there a point-to-point comparison of the stress levels. The error in the stress value in many cases was as large or larger than the stress. The largest errors were seen with Cr K α radiation and originated from the anomalous $\sin^2\psi$ split. S-shaped d-spacing versus $\sin^2\psi$ plot contributed to the errors for the other two radiations used.

The ten data sets from each inclination (27° , 0° , and -27°) were added together to form three aggregate data sets - each aggregate data set corresponding to a particular inclination. The aggregate data sets were formed by combining all of the data for each of the ψ angles. This combined data was then analyzed as if it were from a single measurement. In this manner, the stress over the entire surface for each inclination could be "averaged" to reduce any local stress effects, such as those seen with preferred orientation. The Cr K α data were within one standard deviation of all data taken with the other radiations due to the large error bars associated with the anomalous $\sin^2\psi$ split for this radiation. The Co K α and Cu K α data agreed within two standard deviations for the flat and tilted positions. There was good agreement between all the aggregate data analysis results for the flat and tilted positions for each radiation employed. These aggregate data ranged from -3.1 ± 2.3 (Co K α radiation, -27°) to 7.3 ± 3.2 (Cu K α radiation, 0°).

The intensities of each ψ angle for every measurement revealed very interesting trends (Figures 3-24 through 3-26) that indicate the coupons do not have random orientation of the grains. (The intensities of each ψ angle are uniform if the sample is fine-grained and exhibits random orientation, and they are nonuniform

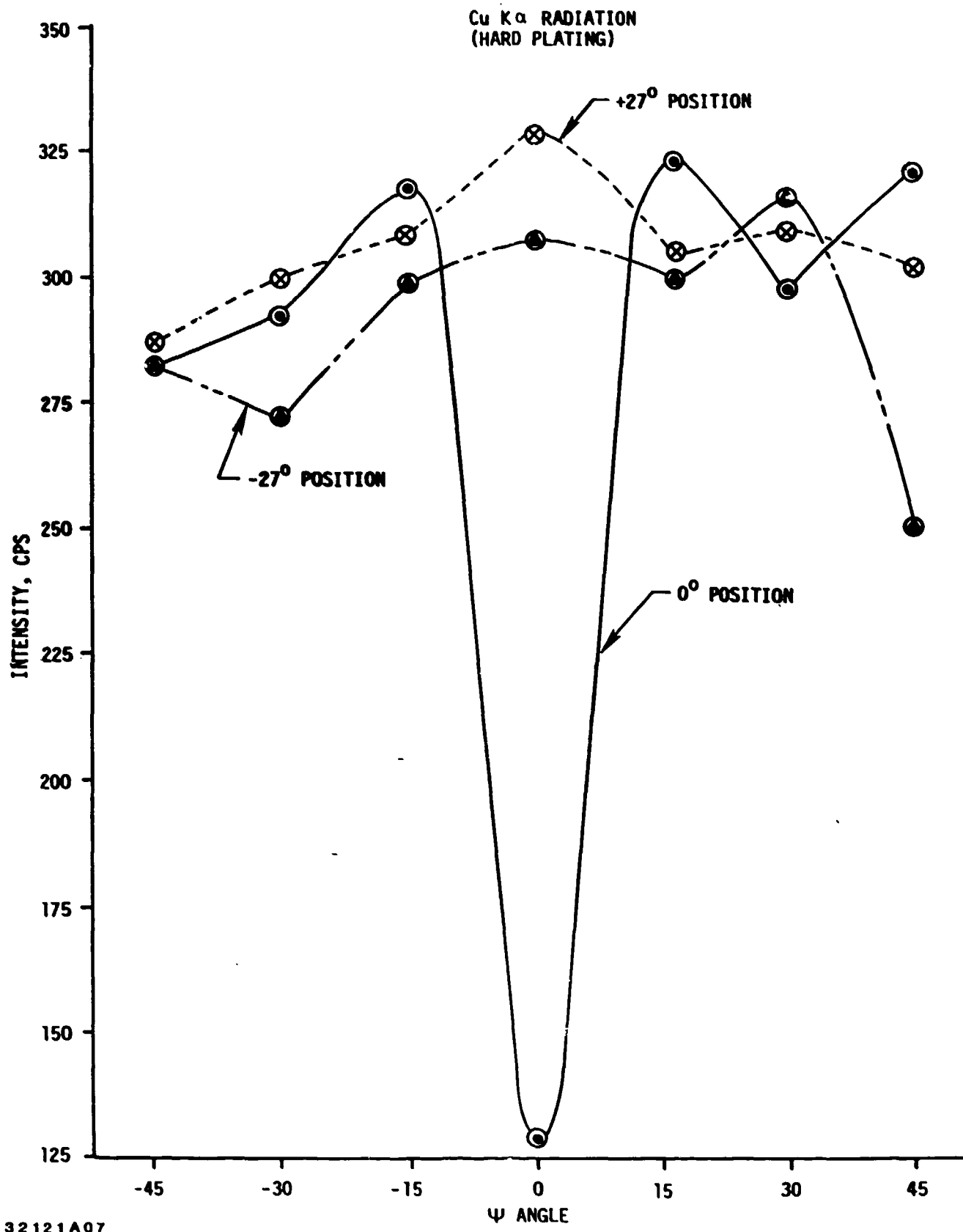
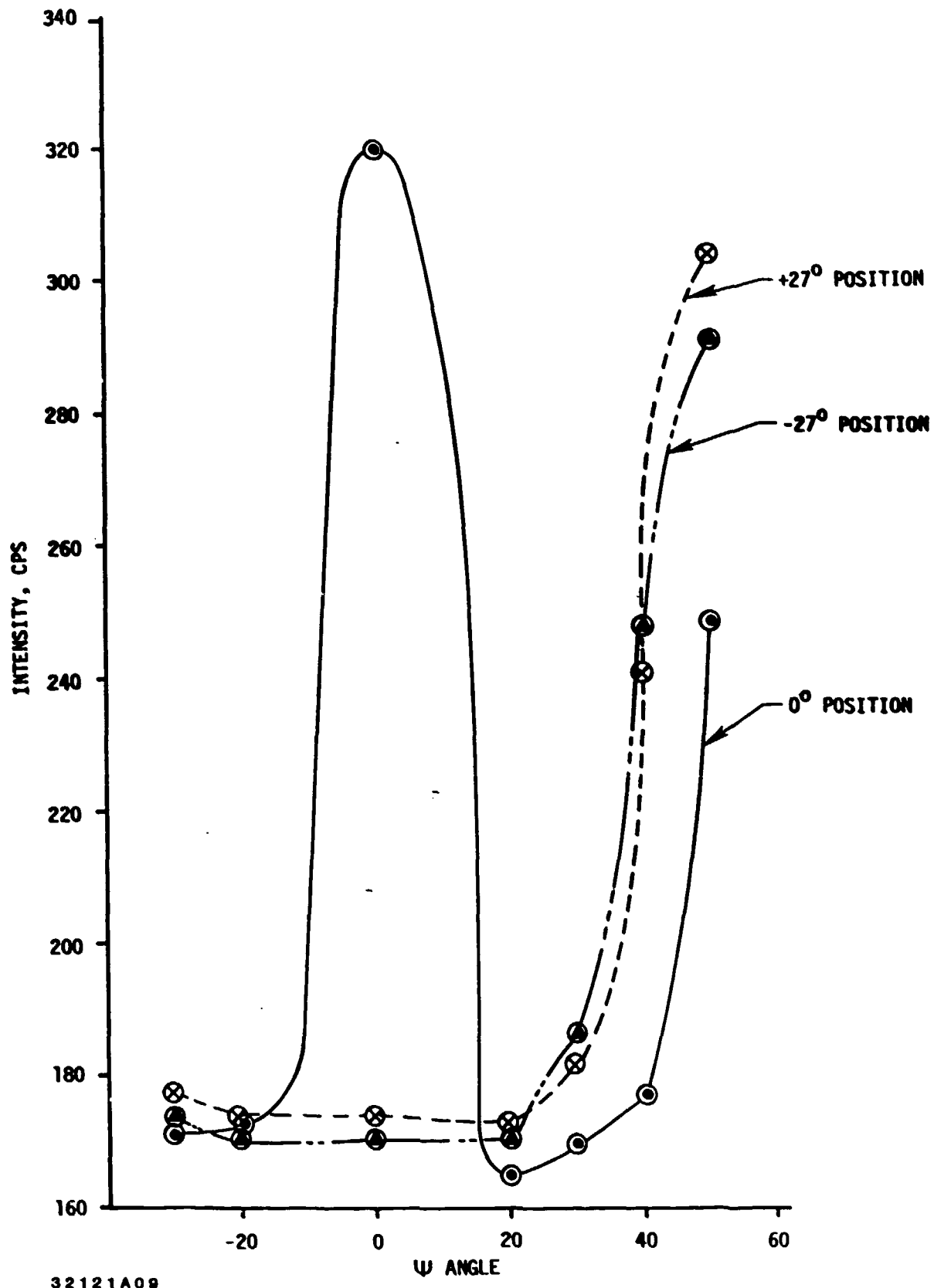
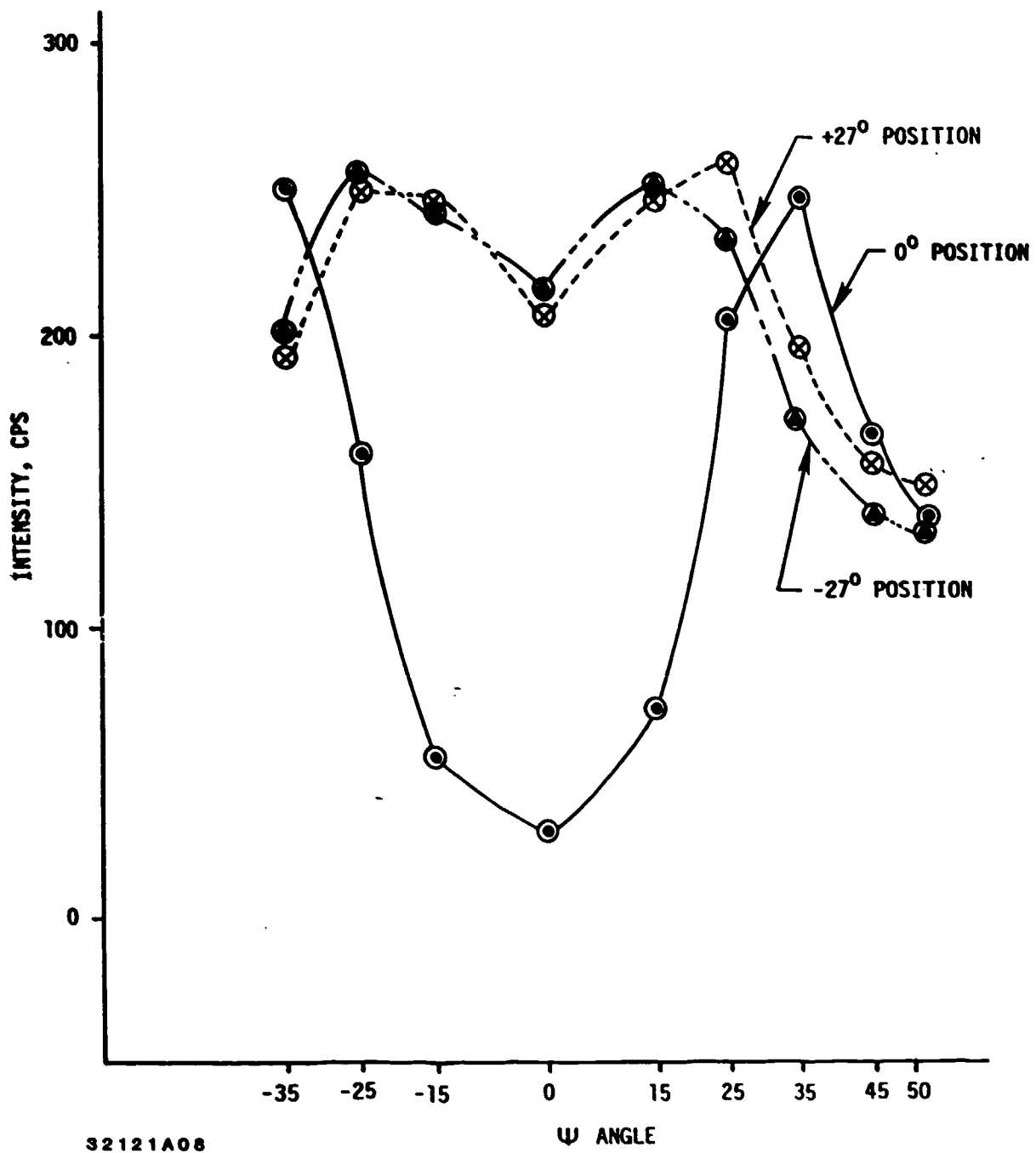


Figure 3-24
Measurement with Cu K α Radiation (Hard Plating)



32121A09

Figure 3-25
Measurement with Co K α Radiation (Hard Plating)



32121A08

Figure 3-26
Measurement with Cr K α Radiation (Hard Plating)

if preferred orientation and/or large grain sizes are present.) For Cu K α and Cr K α radiation, the minimum intensity always occurred at 0° ψ in the 0° position. For Cu K α radiation the ratio of minimum intensity to maximum intensity was approximately 0.4:1, while for Cr K α radiation it was 0.1:1.

The intensities in the tilted positions for these radiations were more uniform and did not show a minimum at 0° ψ . For Co K α radiation which measures the {222} family of planes, the maximum intensity for the flat position occurred at 0° ψ . For Co K α , the maximum intensity for the tilted positions occurred at 50° ψ . The ratio of minimum to maximum intensity was about 0.5:1 for the flat and tilted positions. The {hhh} type of planes such as {222} will show less intensity variation if the sample has preferred orientation due to elastic anisotropy. This appears to be the case for the nickel-plating based on the results with the Co K α radiation.

The results show that the {111} family of planes was oriented parallel to the surface of the plating. These planes have the densest packing and are common slip planes in face-centered cubic materials such as nickel.

Soft Plating - A second flat plate sample which had a softer plating was examined with Cr K α x-rays. Softer plating in this case refers to the surface hardness of the plating which was 43 to 45 Rockwell C scale. The purpose of this testing was to see if the stresses and diffraction peak intensities were more uniform on the softer sample. Ten locations were measured on this sample in the horizontal (0°) position. The stresses were all tensile and ranged from

4.0 ± 10.1 to 15.6 ± 9.5 ksi (Table 3-17). The aggregate data resulted in a stress of 11.1 ± 7.3 ksi. The anomalous $\sin^2\psi$ split seen on the first flat plate sample was also seen on this sample. The intensities for each ψ angle varied with the minimum intensity in each case at $0^\circ\psi$ (Figure 3-27). The ratio of the minimum to the maximum intensity was 0.3:1 which is higher than the ratio for the same radiation on the first flat plate sample. This suggests that this sample has less preferred orientation than the harder nickel-plating.

3.5.1.3 Rotated Flat Plate Sample - The first flat plate sample was reanalyzed with the sample rotating in the horizontal plane about the normal direction to the plating. This experiment was performed to determine if sample rotation would duplicate the stresses found by calculating stress from the aggregate data sets for ten discrete locations. If the data were comparable, then sample rotation would reduce by a factor of about ten times the amount of time needed to collect a sufficient amount of data. The sample was rotated at one revolution per second and the circle traced by the x-ray beam had a diameter of about 1.5 in. Only Cu K α and Co K α radiations were used for this experiment since all previous measurements with Cr K α radiation had large error bars. The results for Cu K α radiation are given in Table 3-18. They range from 5.2 ± 4.6 to 10.3 ± 5.0 ksi. Stress calculated from the aggregate rotation data was 6.7 ± 3.0 ksi. This is an excellent agreement with the aggregate data obtained from the ten discrete measurements in the 0° orientation.

The intensities of the diffraction peaks, with Cu K α radiation, were a minimum at $0^\circ\psi$ (Figure 3-28) and the ratio of minimum to maximum intensities was 0.7:1. This ratio is almost twice that found by using the aggregate data for the ten

Table 3-17.

Residual Stresses for Flat Plate Sample
(Soft Plating)

Cr K α Radiation
0° Position

<u>Position</u>	<u>Stress, ksi</u>
1	4.0 ± 10.1
2	13.4 ± 10.6
3	14.3 ± 10.0
4	11.9 ± 10.4
5	8.2 ± 10.0
6	15.6 ± 9.6
7	10.6 ± 11.8
8	14.1 ± 10.6
9	10.8 ± 8.7
10	8.8 ± 9.2
AGGREGATE	11.17 ± 7.3

Table 3-18.

Residual Stresses for the Rotated Flat Plate Sample
(Hard Plating)

Cu K α Radiation

<u>Stress</u> <u>500 sec</u>	<u>Stress</u> <u>600 sec</u>	<u>Stress</u> <u>1500 sec</u>
6.1 ± 2.6	5.2 ± 4.6	10.3 ± 5.0

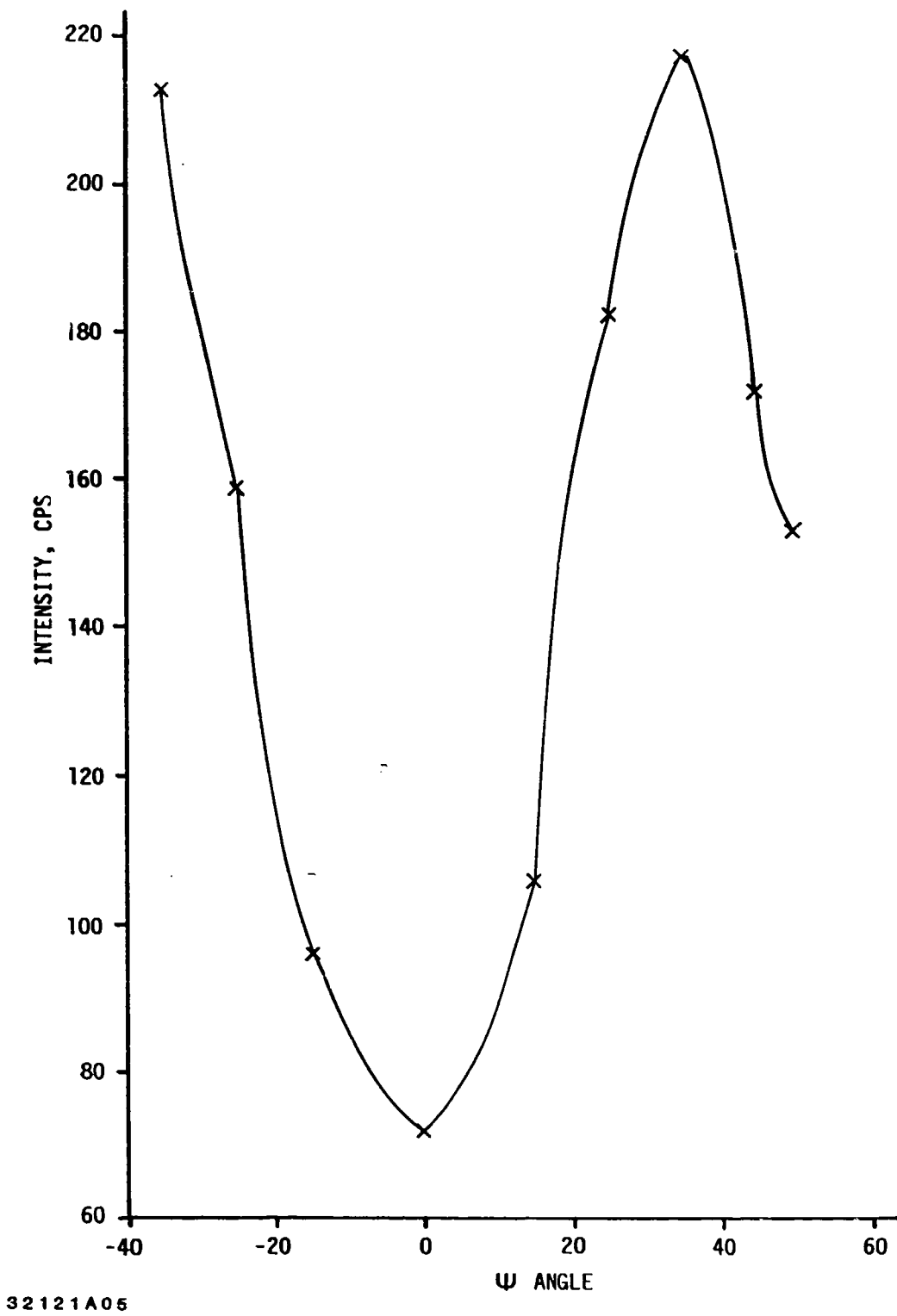
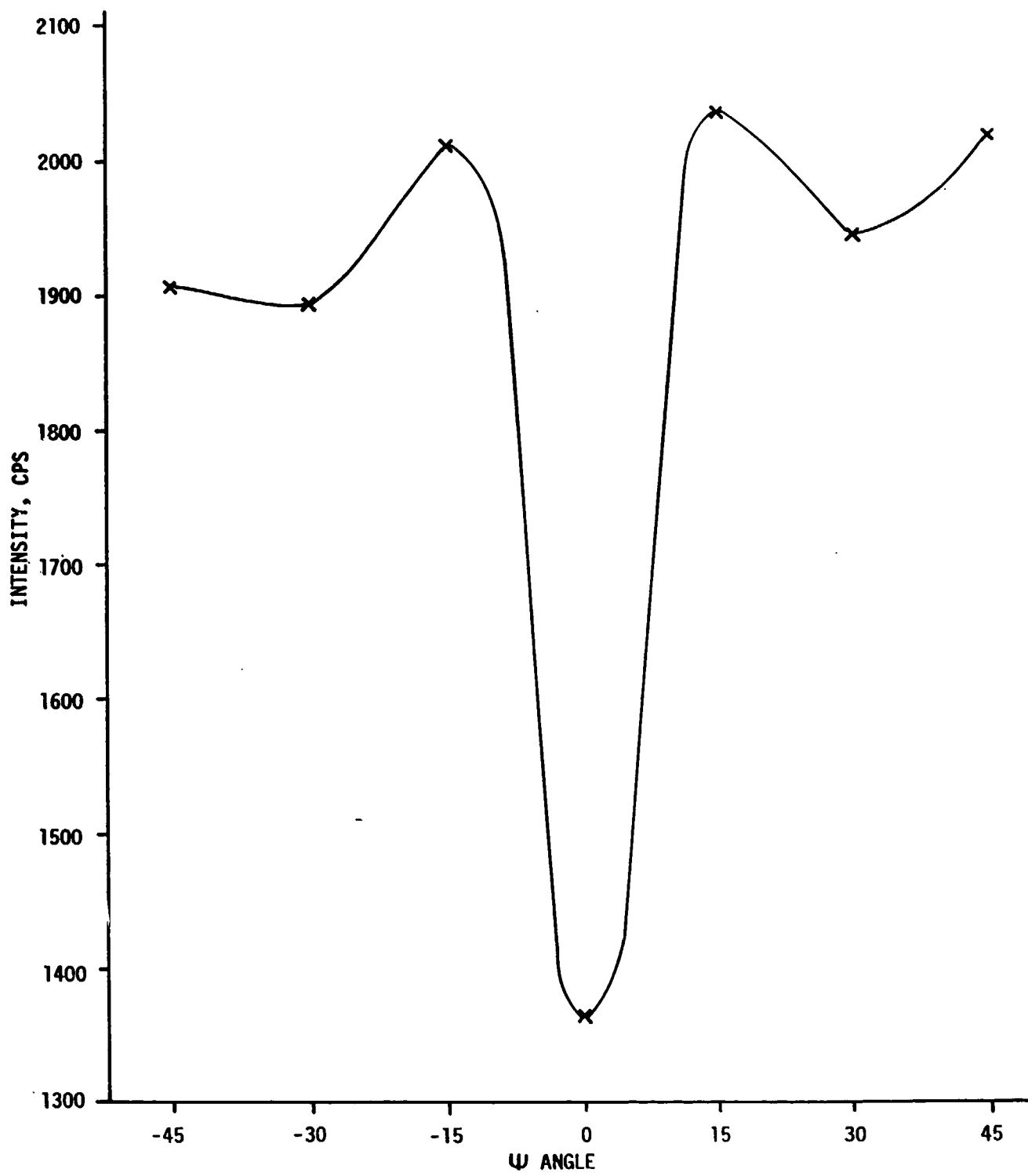


Figure 3-27
 Measurement with Cr K α Radiation (Soft Plating)



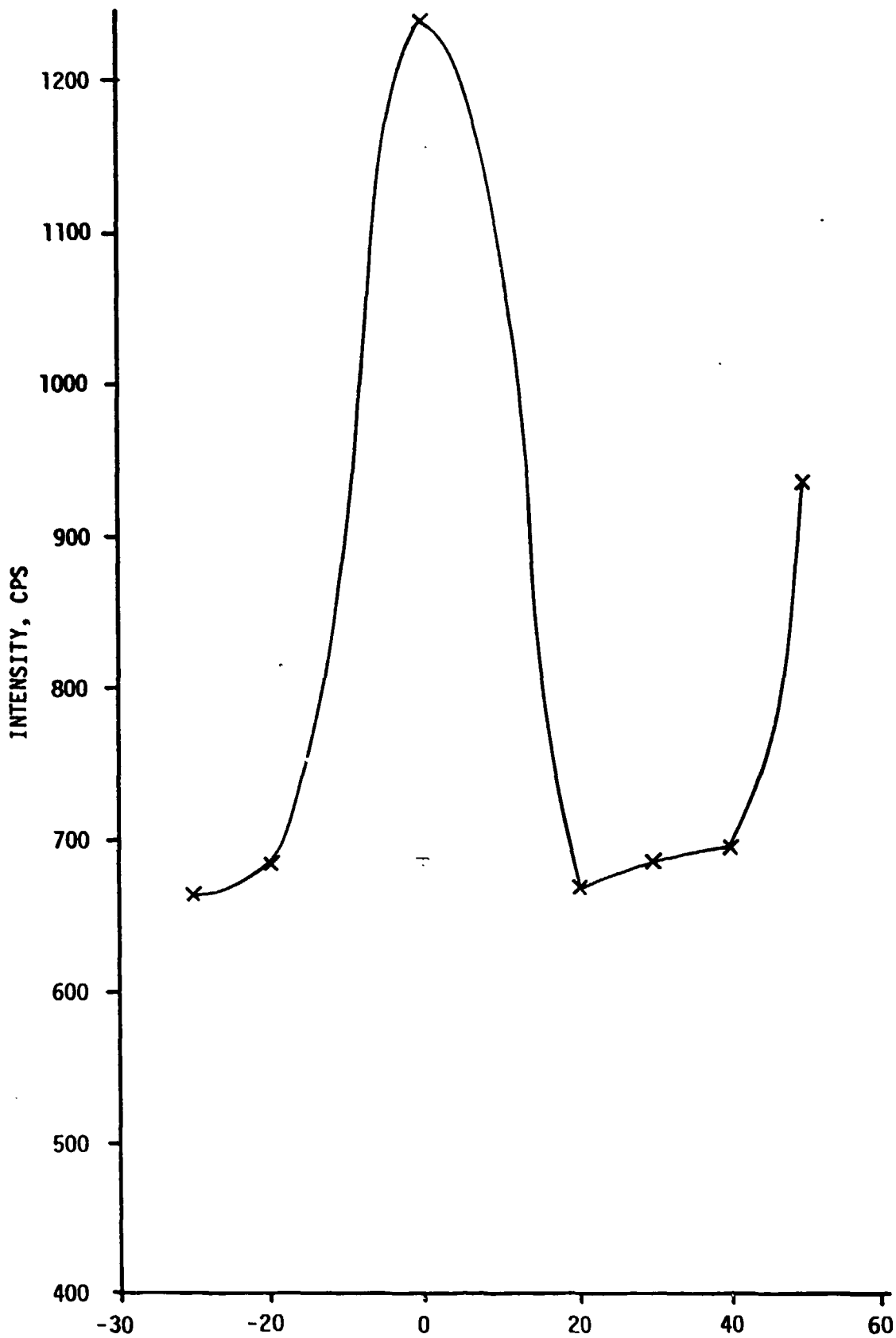
32121A06

Figure 3-28
Measurement with Cu K α Radiation (Rotating Sample)

discrete points. This result suggests that rotating the sample may be a superior technique to taking data at discrete locations and combining the data since rotation in this case reduced the variation in intensities. In other words, sample rotation reduced the effects of preferred orientation on the calculated stress value. In some cases sample translation, (back-and-forth movement along a single axis) would be more appropriate than sample rotation. The nickel-plated coupon was essentially stress-free in both the longitudinal and transverse directions. Had the stresses in one direction been sufficiently different from those in the orthogonal direction, then sample rotation would have the affect of averaging not only the intensities but also the stresses in all directions on the surface of the plane.

Data taken with Co K α radiation ranged from -8.5 ± 8.4 to -23.1 ± 9.9 ksi. All of these measurements had a $\sin^2\psi$ split. The aggregate rotation data resulted in a stress value of -14.9 ± 6.2 ksi which does not correlate well with the aggregate data obtained for the ten discrete measurements.

The intensities of the rotated data (Figure 3-29) did correlate well with the previous measurements on the stationary sample. The maximum intensity occurred at $0^\circ\psi$, and the intensity ratio was 0.5:1. A $\sin^2\psi$ split can generally be attributed to shear stresses in the sample or an incorrect ψ -angle indication. Since the coupon had very low stresses, shear stresses were unlikely. A series of diffractometer positioning experiments were conducted to determine if the ψ angle was correct. These experiments revealed that the x-ray tube position deviated from the center of rotation by about 0.005". This deviation could easily have caused the $\sin^2\psi$ splits.



Ψ ANGLE
Figure 3-29
Co K α RADIATION (ROTATED SAMPLE)

3.5.1.4 Cr K β Measurements

Flat Plate - A measurement was made on the first flat plate sample using Cr K β radiation to determine if this would reduce or remove the anomalous $\sin^2\psi$ split. This radiation penetrates the sample to about the same degree as Cr K α radiation. Its advantage over Cr K α radiation is that it has a single line of radiation. The Cr K α radiation consists of a K α 1 and a K α 2 component. Defocusing errors caused by the detector deviating from the focusing circle can result in a skewed peak that is compounded by the presence of the two components. This effect is greater at the lower back reflection angle (2θ - 135°) used for the {220} planes in nickel. Cr K β radiation causes diffraction of the {311} planes at a high back reflection angle of about 157° . The main disadvantage of Cr K β radiation is its relatively low intensity - less than a fourth of the intensity of the Cr K α line. Fortunately, the position-sensitive proportional counter used as the detector on the TEC Stress Analyzer can easily detect even the low intensity radiation from the Cr K β line. The stress measured by the Cr K β radiation on the flat plate sample was -8.7 ± 5.4 ksi (Table 3-19). Not only did this value agree well with measurements made with the other radiations, but the anomalous $\sin^2\psi$ split was no longer present.

Camshaft - Stress measurements were made on a camshaft with Cr K β radiation as a result of the apparent success with this radiation to produce d-spacing versus $\sin^2\psi$ plots without the anomalous $\sin^2\psi$ split. The particular camshaft used for these measurements had been plated with a plating current density of 75 A/ft^2 and was in the as-plated condition. This camshaft was selected because of the high compressive stresses measured on the plated region during

Table 3-19.

**Residual Stress and Diffraction Peak Intensities
for the Flat Plate Sample Using Cr K β Radiation**

Position ψ 3	<u>Position</u>		<u>Stress, ksi</u>				
	-45	-30	-15	0	15	30	45
	168.4	207.6	187.2	366.7	232.3	184.3	170.9

Table 3-20.

**Summary of Residual Stress
for Navy Pensacola Nickel Plated Camshaft 75 ASF**

<u>Location</u>	<u>Residual Stress (ksi)</u>		
	<u>6 mm inboard¹</u>	<u>Center</u>	<u>6 mm outboard²</u>
1	-109.2 \pm 10.6 -121.5 \pm 11.7 - 98.2 \pm 9.6	-106.9 \pm 16.4 -101.5 \pm 18.4 -111.9 \pm 34.1 - 89.5 \pm 23.2	-100.4 \pm 7.5 - 93.9 \pm 9.6
2	-108.7 \pm 21.6	-119.1 \pm 47.2	- 92.2 \pm 47.7
3	-105.8 \pm 10.8 -111.9 \pm 21.2	-104.2 \pm 7.8 -105.3 \pm 21.2	-113.2 \pm 9.0 -127.2 \pm 21.4
4	-101.7 \pm 7.4	-113.6 \pm 10.9	-104.4 \pm 6.3 -117.0 \pm 32.8
1.5 ³		- 91.7 \pm 8.4 -131.9 \pm 10.2 (filed) - 2.8 \pm 9.6 (etched)	

¹ Measurements made 6 mm inboard of center of plated region.
² Measurements made 6 mm outboard of center of plated region.
³ Measurements made midway between locations 1 and 2.

the Phase I testing. There was concern that nickel-plating could not support compressive stresses of this magnitude (~85 ksi). Testing during the current study with the Cr K β radiation resulted in relatively linear d-spacing versus $\sin^2\psi$ plots and high compressive stresses.

Axial measurements were made at four locations around the circumference of the camshaft spaced at 90° apart. At each circumferential position three locations were selected for comparison - 6 mm from either side of the center of the plated region. All measurements were similar with a range from -90 to -127 ksi (Table 3-20). A private communication with Dr. Jerome Cohen of Northwestern University led to the conclusion that nickel-plating can support high compressive stresses at the surface. Dr. Cohen indicated that stresses in nickel-plating could be similar to stresses in work hardened nickel. Furthermore, the higher current density used on this camshaft compared to the 50 A/ft² current density normally used could result in higher compressive stresses in this camshaft. This is consistent with the results of the Phase I study. The yield strength of Nickel 200 (commercially pure nickel) in a cold worked condition can be as high as 135 ksi according to the American Society for Metals' Metals Handbook, Vol. 3. The stresses calculated in the present study, while approaching the yield strength, are probably reasonable.

A series of measurements were made at a circumferential location between two of the other sets of measurements to determine how the stresses varied with depth into the plating. These measurements were made at the center of the plated region. The surface stress, -92 ksi, was within the range of the other surface stress measurements made. The plating was then filed to remove about 0.003"

and remeasured. The stress was -132 ksi which is consistent with the work hardening expected to result from the filing process. This area was subsequently electropolished to remove the disturbed material caused by filing. Approximately 0.0003" was removed during this process. The stress at this depth (~1/3 of the plating depth) dropped to -3 ksi. These results suggest that there is a high stress gradient in this plating.

3.5.2 Conclusions

The series of experiments performed was successful in accomplishing the objectives set forth for this task. The measurements made on the flat plate sample indicated that the residual stress was essentially zero. The s-shaped d-spacing versus $\sin^2\psi$ curves were attributed to preferred orientation of the grains in the plating. The preferred orientation was due to elastic anisotropy, and a semi-quantitative pole figure showed the {111} planes oriented parallel to the surface of the plating.

Multiple measurements could be made and the data combined into an aggregate data set. The stresses analyzed from the aggregate data were less sensitive to the preferred orientation than the individual data points. The data could be acquired in a significantly shorter period of time by rotating the sample. These data compared favorably to the aggregate data and the acquisition time was a tenth of that required for the aggregate data. This technique can thus allow a much faster stress measurement on samples with preferred orientation.

The $\sin^2\psi$ split observed with Co K α radiation is apparently due to a deviation from the center of rotation of the x-ray tube. The deviation, about 0.005", is

sufficient to give a $\sin^2\psi$ split. The stress state of the plated coupon is low enough that shear stresses are very unlikely.

The high compressive stresses measured on the 75 A/ft² camshaft during the Phase I program were confirmed with the Phase II measurements. The surface residual stress approaches the yield strength of commercially pure nickel. At about 0.003" into the surface the stress drops to almost zero that indicates a high stress gradient in the stress through the plating.

The most interesting finding of this study was the benefits of using Cr K β radiation. This radiation is similar to Cr K α radiation in terms of penetration into the surface of the sample. It is superior to Cr K α radiation because it produces more precise data. The precision is improved because Cr K β radiation uses a higher back reflection diffraction peak and the anomalous $\sin^2\psi$ split (Figure 3-30) disappears. The shift in the diffraction peaks which is used to calculate stress can be determined more precisely at the higher back reflection angles. The precision of the stress is also improved as the d-spacing versus $\sin^2\psi$ plot becomes more linear. The anomalous $\sin^2\psi$ split was attributed to defocusing errors that are larger at the lower back reflection angles and more prevalent with a radiation that has a double line (K α_1 -K α_2). Thus, these defocusing errors can be dramatically reduced by using Cr K β radiation (Figure 3-31). The results from this radiation were consistent with the results obtained with Co K α and Cu K α radiations.

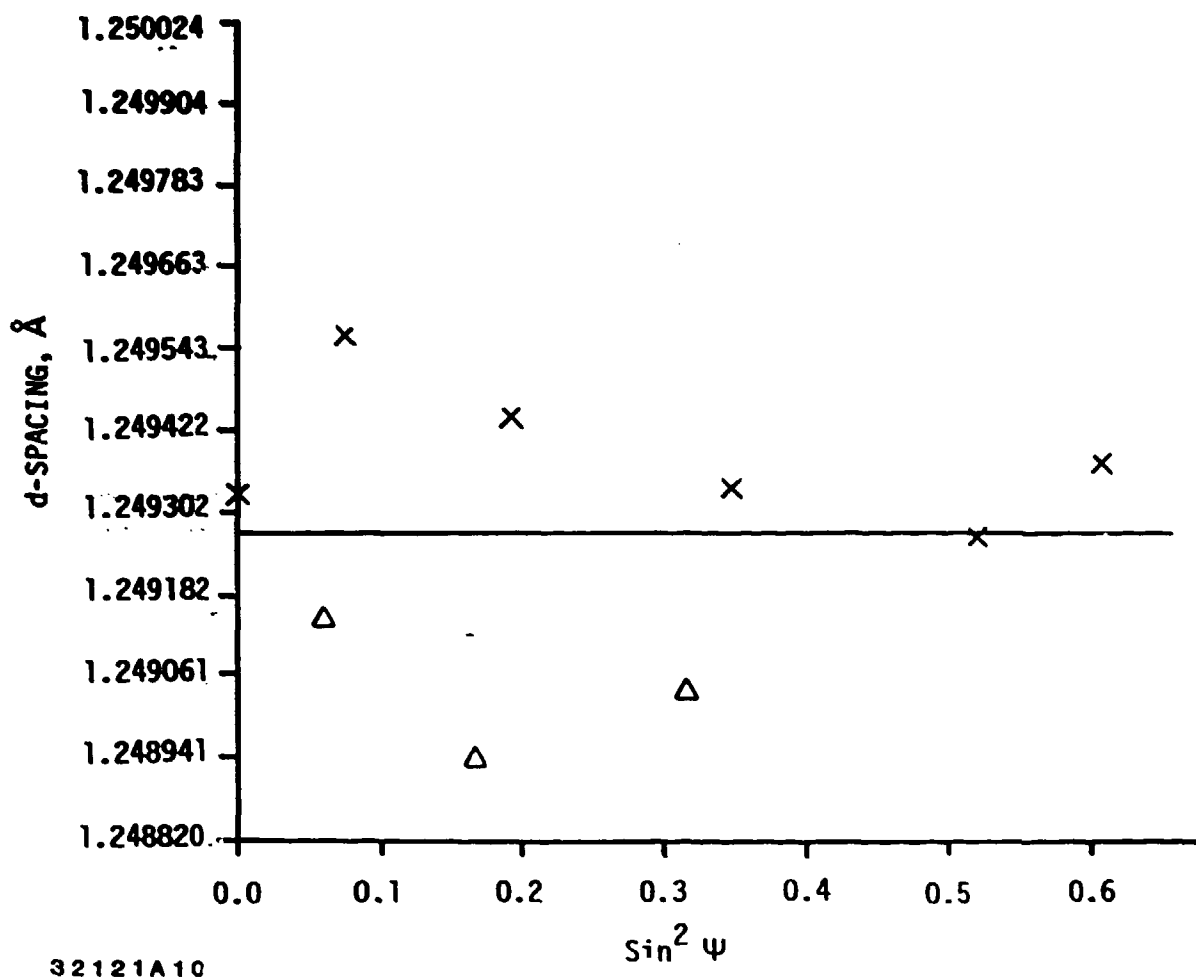


Figure 3-30
 D-Spacing Versus $\sin^2 \psi$ Plot Showing Anomalous $\sin^2 \psi$ Split

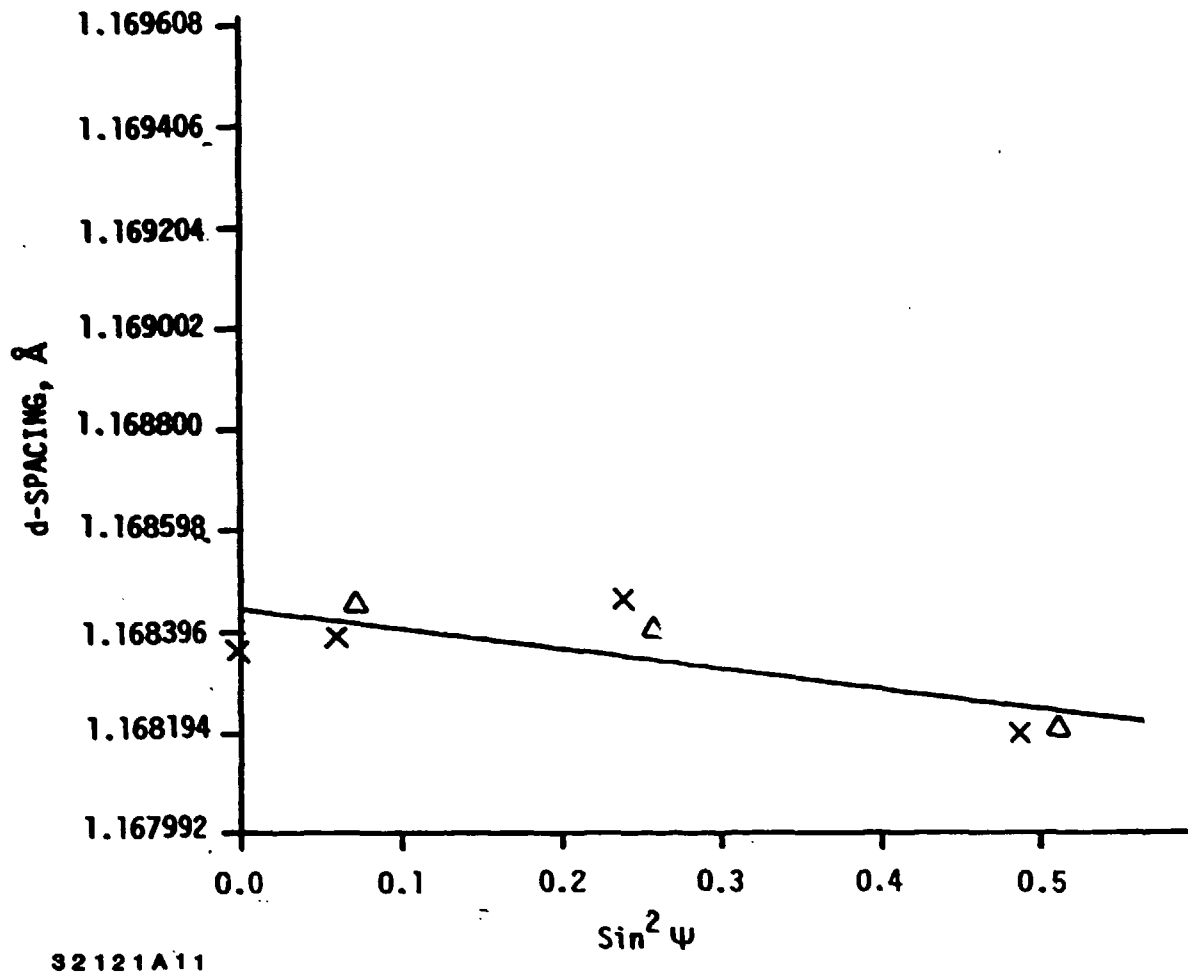


Figure 3-31
 D-Spacing Versus $\sin^2 \psi$ Plot for Nickel Plating Using Cr $K\beta$ Radiation

3.5.3 Nickel-Plated Fatigue Samples

3.5.3.1 Introduction - The purpose of this study was to evaluate the fatigue life on four groups of nickel-plated samples and compare fatigue life to residual stress levels. Twenty-eight nickel-plated fatigue samples were supplied by NARF-Pensacola for the residual stress analysis and fatigue testing program. The samples were made of 4340 steel heat treated to a hardness of 35 Rockwell C. The button head dog bone samples were prepared according to drawings supplied by Metcut Research Associates for low cycle axial fatigue testing (Figure 3-32). The specified surface finish was 32 RMS. Each sample was inspected according to MIL-I-6868 for magnetic particle inspection and then shot peened following NARF-Pensacola standard pre-plating operations. The samples were nickel-plated to a thickness of 0.010 inches per side. They were then divided into four groups of seven samples each. Five mils (0.005 inches) were removed from each sample per the following instructions:

Group A: Standard Grinding

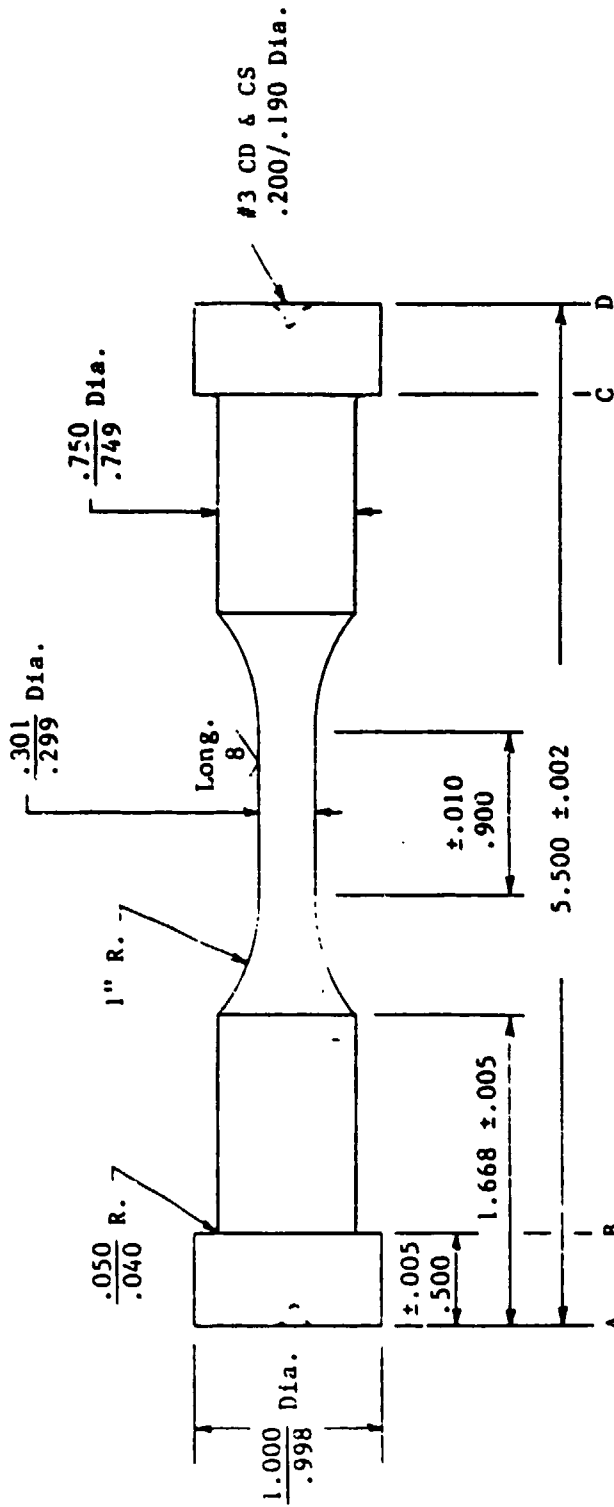
Group B: Abusive Grinding (coolant cut off intermittently and greater infeed)

Group C: Standard Machining

Group D: Abusive Machining (coolant cut off and varied feed and speed)

The testing program consisted of stress analysis on the samples followed by fatigue testing. Post-fatigue test stress analysis was then performed.

NOTE: For planning purposes only; do not manufacture without approval from test engineering.



Gage and shoulders to be concentric within .0005
Surfaces A,B,C & D to be flat and parallel within .001

LOW CYCLE AXIAL FATIGUE		Metcut Research Associates Inc. Cincinnati, Ohio 45209-1196	
LCIRS	Approval	Date	Dwg. No. 820914-2
DRAWN	<i>J.P.</i>	10-18-84	
TEST	<i>V. Stone</i>	1-8-85	
MFG	<i>Cl. Miller</i>	10-22-84	
QA	<i>K. Quinn</i>	1-8-85	

Figure 3-32
Button Head Dog Bone Samples for Low Cycle Axial Fatigue Testing

3.5.3.2 Measurements - The samples were first analyzed for residual stresses. Measurements were made in the center of the gage length in the axial direction using Cr K β radiation. Five ψ tilts ranging from -43° to $+43^\circ$ were selected, and a ψ -angle oscillation of $\pm 2^\circ$ was used to reduce the effects of preferred orientation.

After stress analysis, the samples were sent to Metout Research Associates, Inc. for fatigue testing. Room temperature, high-cycle fatigue tests were performed. A sinusoidal waveform at a frequency of 35Hz was used. Stress versus cycles to failure (S/N) curves were developed for each group.

The samples were then returned to TEC for post-fatigue test stress analysis. Stress measurements were repeated following the same procedure used during initial testing.

3.5.3.3 Results and Discussion - The residual stresses and the fatigue test results are tabulated in Tables 3-21 and 3-22. Figures 3-33 through 3-37 are the S/N curves generated from the fatigue test data. Figures 3-38 through 3-41 depict the failure location for each sample.

The stress analysis data show that, in general, the standard and abusive grinding result in low stresses and the standard and abusive machining results in compressive stresses. As a group, there was no apparent difference between the standard and abusive processing in terms of their surface residual

Table 3-21.

Surface Residual Stresses in Nickel-Plated Fatigue Samples

Sample I.D.	Process	Pre-Fatigue Testing			Post-Fatigue Testing		
		Stress, ksi		F _{WH} , °2θ	Stress, ksi		F _{WH} , °2θ
A1	Standard Grinding	- 5.3 ±	9.7	2.3	-9.1 ±	9.2	2.5
A2		- 8.2 ±	7.1	2.2	-12.0 ±	8.7	2.9
A3		+ 1.1 ±	4.6	2.1	+11.5 ±	3.7	2.3
A4		- 9.0 ±	4.0	2.2	+ 3.8 ±	6.3	2.1
A5		-10.3 ±	13.2	2.4	+ 5.3 ±	11.3	2.6
A6		- 5.1 ±	4.7	2.4	-23.6 ±	4.5	2.2
A7		- 5.7 ±	5.8	2.3	-33.6 ±	17.7	2.4
B1	Abusive Grinding	- 9.6 ±	7.4	2.2	- 6.7 ±	10.1	2.4
B2		-13.2 ±	7.9	2.4	-20.4 ±	11.6	2.4
B3		-27.2 ±	11.1	2.4	+36.4 ±	10.0	2.5
B4		-36.2 ±	3.4	1.8	-31.3 ±	6.2	1.8
B5		+ 1.3 ±	4.7	2.2	-10.9 ±	13.6	2.5
B6		- 0.5 ±	6.1	2.1	- 9.5 ±	4.5	2.2
B7		- 9.1 ±	8.9	2.3	- 7.1 ±	10.7	2.6
C1	Standard Machining	-64.5 ±	12.6	2.3	-46.8 ±	10.6	2.4
*C2		-64.7 ±	12.9	2.3	-97.8 ±	14.6	2.9
C3		-72.8 ±	10.0	1.9	-81.3 ±	13.1	2.6
C4		-77.3 ±	10.9	2.4	-49.1 ±	13.3	2.4
C5		-53.0 ±	8.7	2.2	-88.3 ±	3.6	2.7
C6		-23.4 ±	16.5	2.1	-33.9 ±	10.6	2.7
C7		-38.4 ±	10.1	2.3	-21.5 ±	10.8	2.5
D1	Abusive Machining	-46.9 ±	7.0	2.3	-46.6 ±	10.2	2.4
D2		-74.9 ±	24.3	2.3	-61.9 ±	12.8	2.7
D3		-17.0 ±	5.2	2.3	-36.0 ±	19.9	2.4
**D4		+12.1 ±	7.5	1.8	+ 3.1 ±	9.0	2.2
D5		-31.2 ±	9.7	2.3	-35.9 ±	8.1	2.6
D6		-42.9 ±	9.3	2.2	-45.5 ±	10.2	2.6
D7		-53.3 ±	10.8	2.3	-70.2 ±	7.2	2.9

*Sample overloaded during fatigue test resulting in a void test.

**Sample in the as-plated condition.

Table 3-22.

Axial Fatigue Data Summary
Nickel-Plated 4340 Steel
75°F 35 Hz. A = Infinity

Standard Grinding

Test Number	Specimen Number	Temp. (°F)	Stress Max. (ksi)	Alt. (ksi)	Cycles (X10 ³)	Results	Test Hours
1	A1	75	80	80	33.3	Failure	.3
2	A2	75	70	70	67.5	Failure	.6
9	A3	75	60	60	28.7	Failure	.2
13	A4	75	50	50	38.2	Failure	.4
16	A5	75	40	40	218.4	Failure	1.8
21	A6	75	30	30	184.9	Failure	1.5
25	A7	75	15	15	10,758.1	Runout	85.4

Abusive Grinding

3	B1	75	80	80	13.0	Failure	.1
6	B2	75	70	70	76.2	Failure	.7
10	B3	75	60	60	36.8	Failure	.3
14	B4	75	50	50	30.8	Failure	.3
22	B6	75	45	45	213.1	Failure	1.7
23	B7	75	42	42	51.7	Failure	.4
17	B5	75	40	40	10,876.2	Runout	86.3

Standard Machining

4	C1	75	80	80	53.8	Failure	.6
26	C7	75	70	70	392.0	Failure	3.4
15	C4	75	70	70	2,283.3	Failure	18.1
24	C6	75	60	60	246.6	Failure	1.9
12	C3	75	60	60	916.8	Failure	7.2
19	C5	75	50	50	10,025.5	Runout	79.6

Abusive Machining

5	D1	75	80	80	10.9	Failure	.1
8	D2	75	70	70	46.7	Failure	.4
28	D7	75	70	70	10,338.0	Failure	80.7
18	D4	75	65	65	27.5	Failure	.4
27	D6	75	65	65	408.1	Failure	3.3
11	D3	75	60	60	6,016.2	Failure	47.7
20	D5	75	60	60	11,000.0	Runout	85.9

Note: S/N C-2 ran 332,700 cycles at 70 ksi when due to a controller malfunction, the specimen was overloaded in compression. Void test.

P/A stress calculation based on gross area.



METCUT RESEARCH ASSOCIATES INC.
4340 STEEL W/.005 STD. NI. PLATING
75F O/N MRA B20214-2 NOM. GAGE DIA. .300

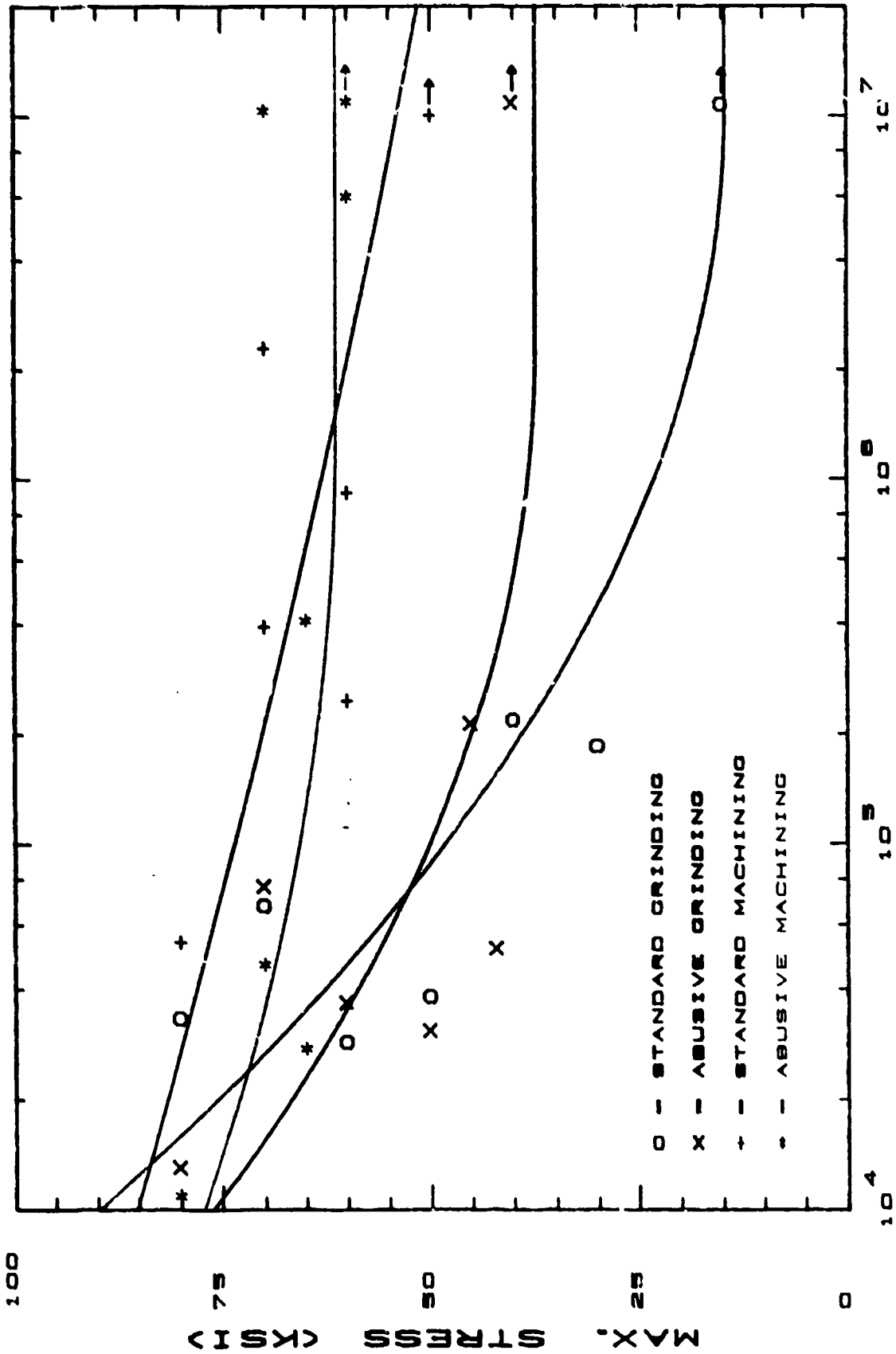
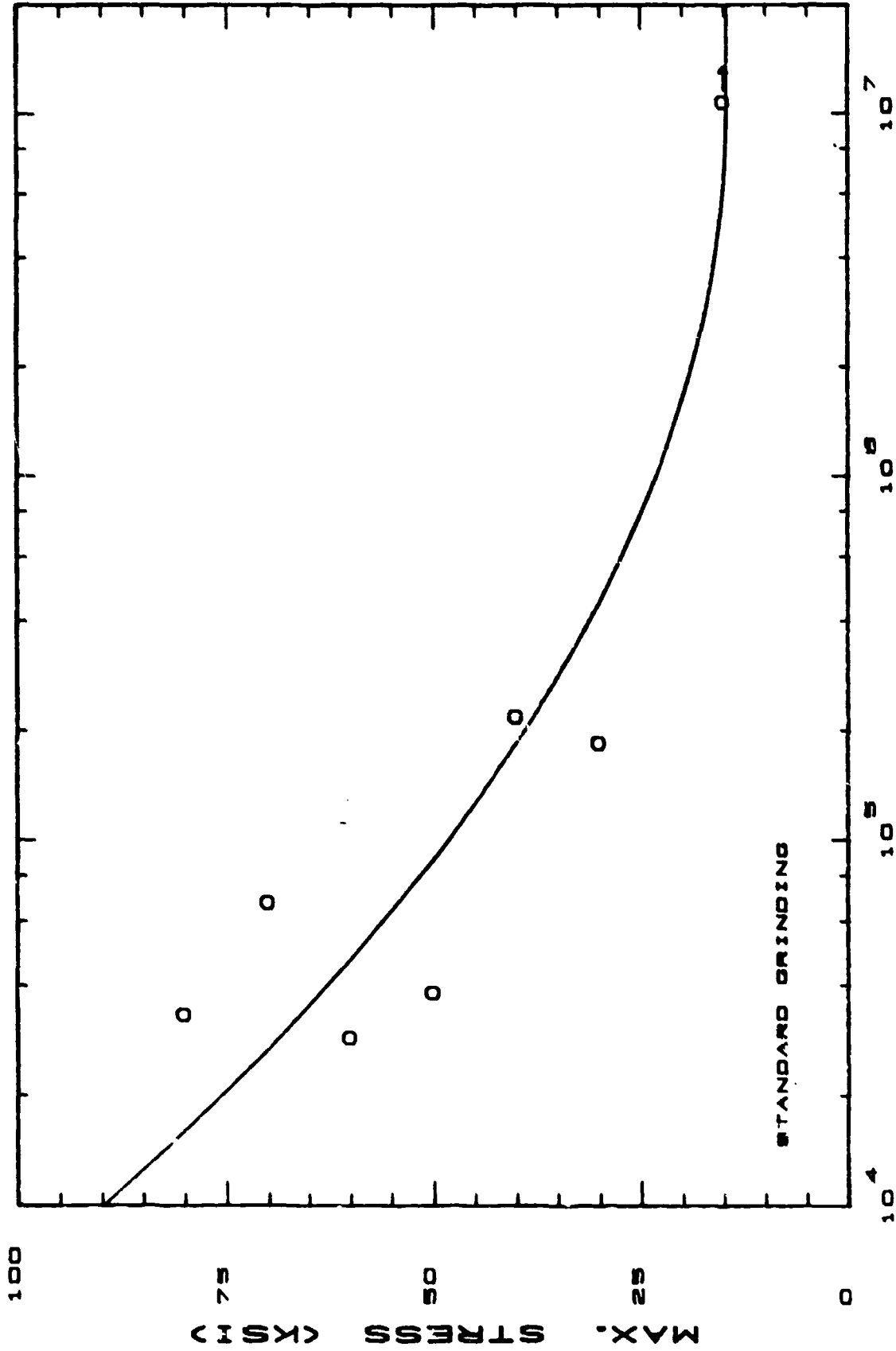


Figure 3-33
S/N Curves for All Samples



METCUT RESEARCH ASSOCIATES INC.
4340 STEEL W/.005 STD. NI. PLATING
75F D/N MRA 820014-2 NOM. GAGE DIA. .300



STANDARD GRINDING

Figure 3-34
S/N Curves for Standard Grinding Samples



METCUT RESEARCH ASSOCIATES INC.
4340 STEEL W/.005 STD. NI. PLATING
75F D/N MRA 820914-2 NOM. GAGE DIA. .300

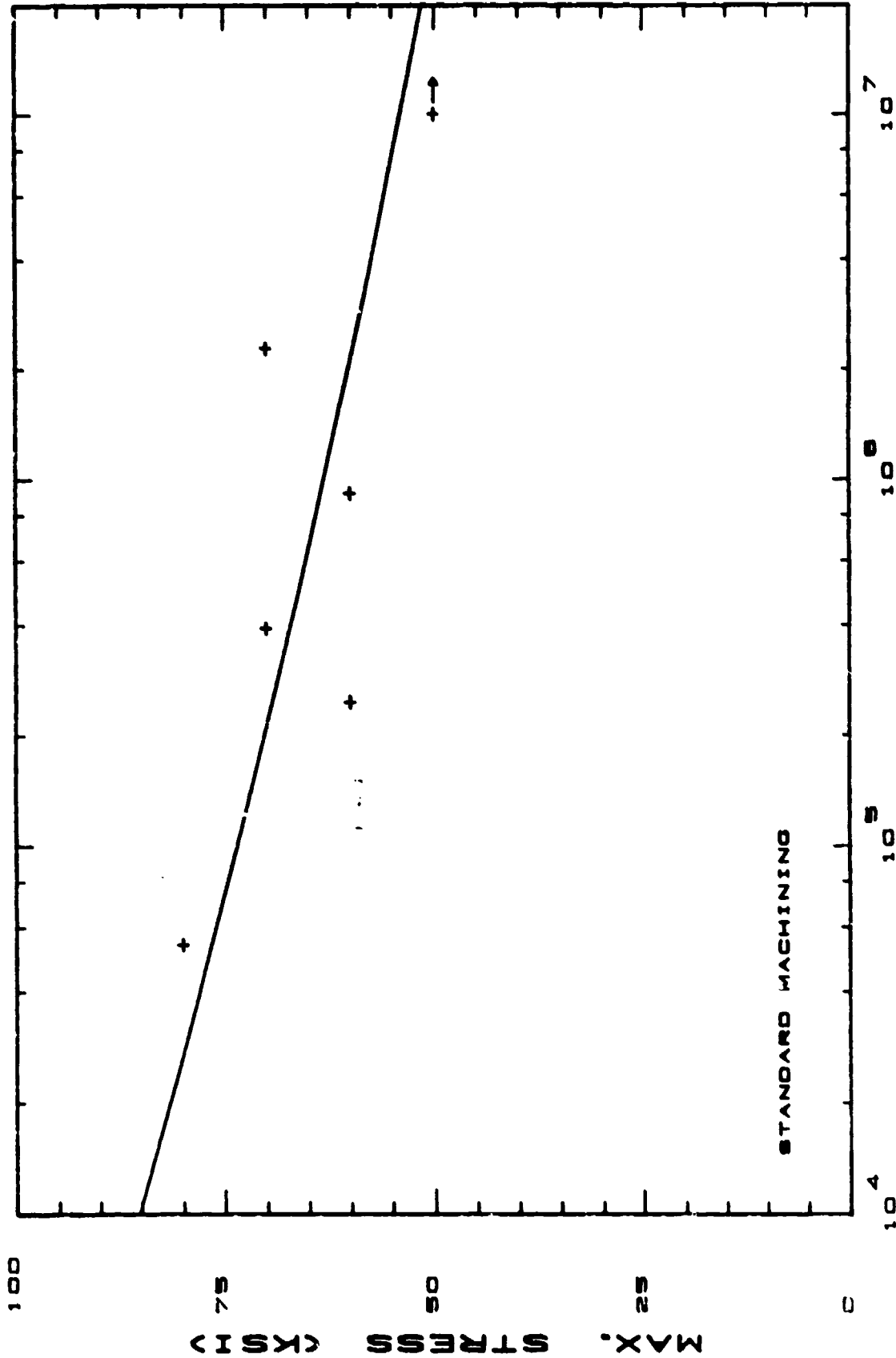


Figure 3-35
S/N Curves for Standard Machining Samples



METCUT RESEARCH ASSOCIATES INC.
4340 STEEL W/.005 STD. NI. PLATING
75F D/N MRA B20B14-2 NOM. GAGE DIA. .300

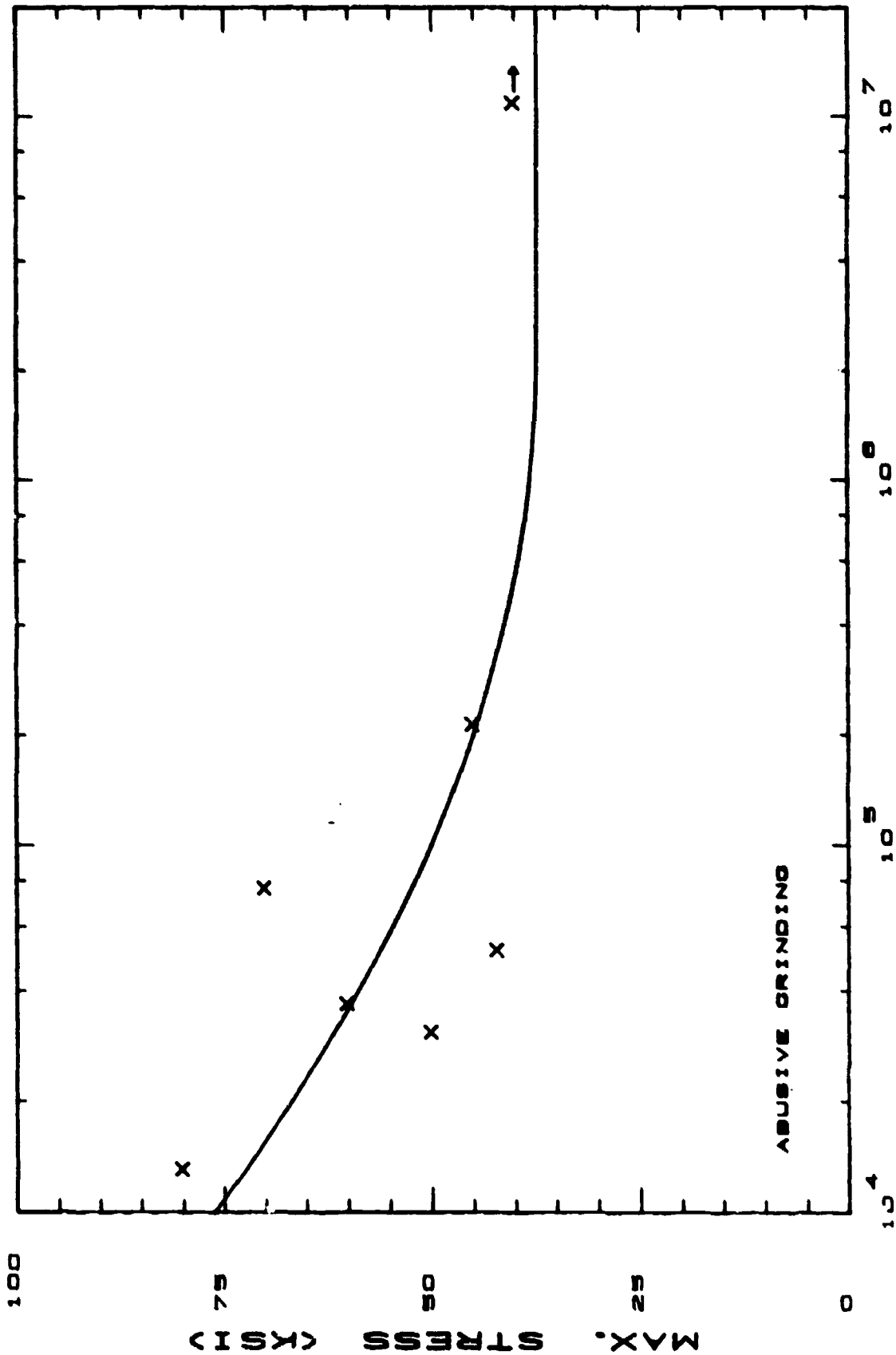


Figure 3-36
S/N Curves for Abusive Grinding Samples



METCUT RESEARCH ASSOCIATES INC.
4340 STEEL W/.005 STD. NI. PLATING
75F D/N MRA 820914-2 NOM. GAGE DIA. .300

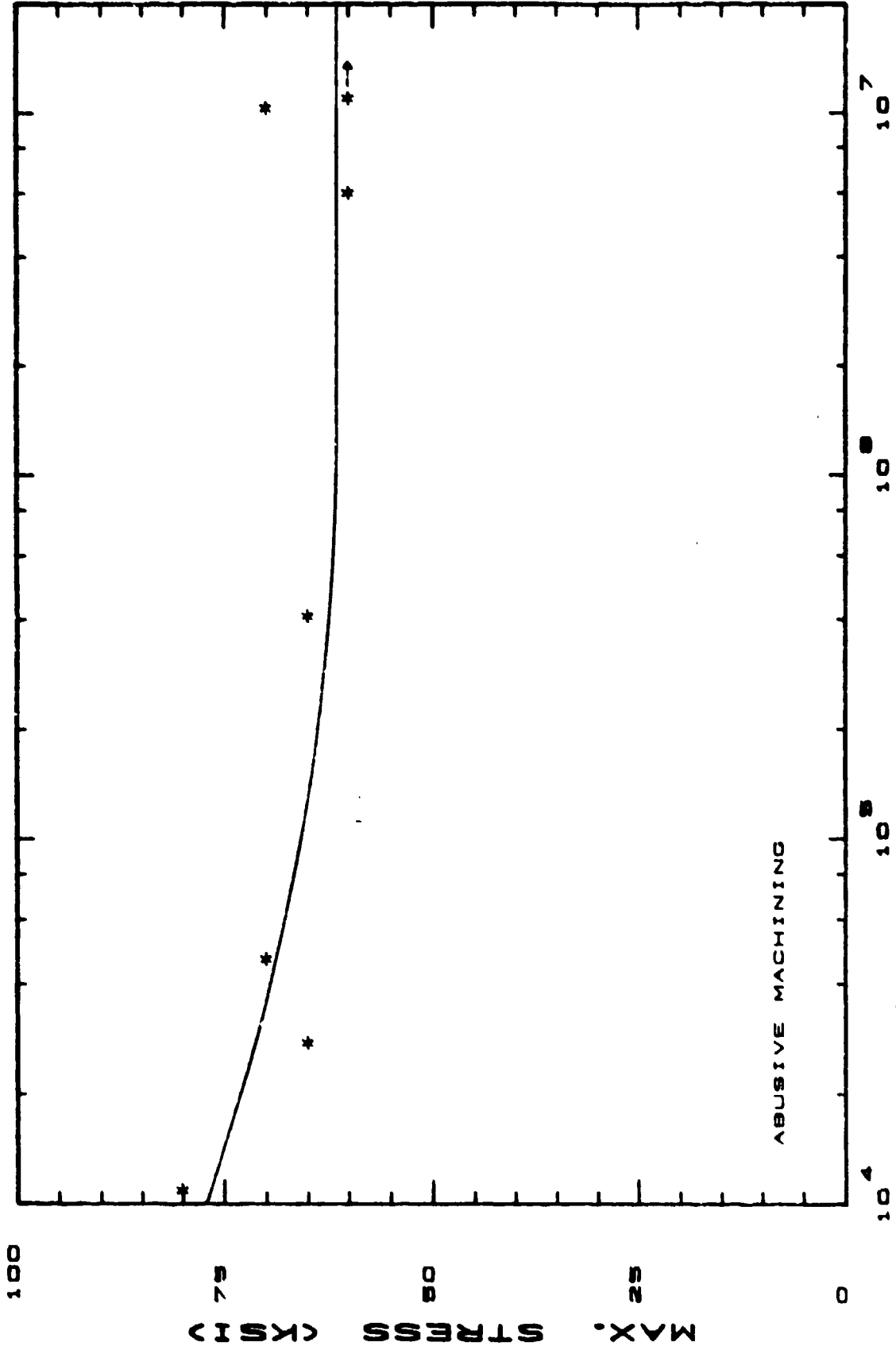
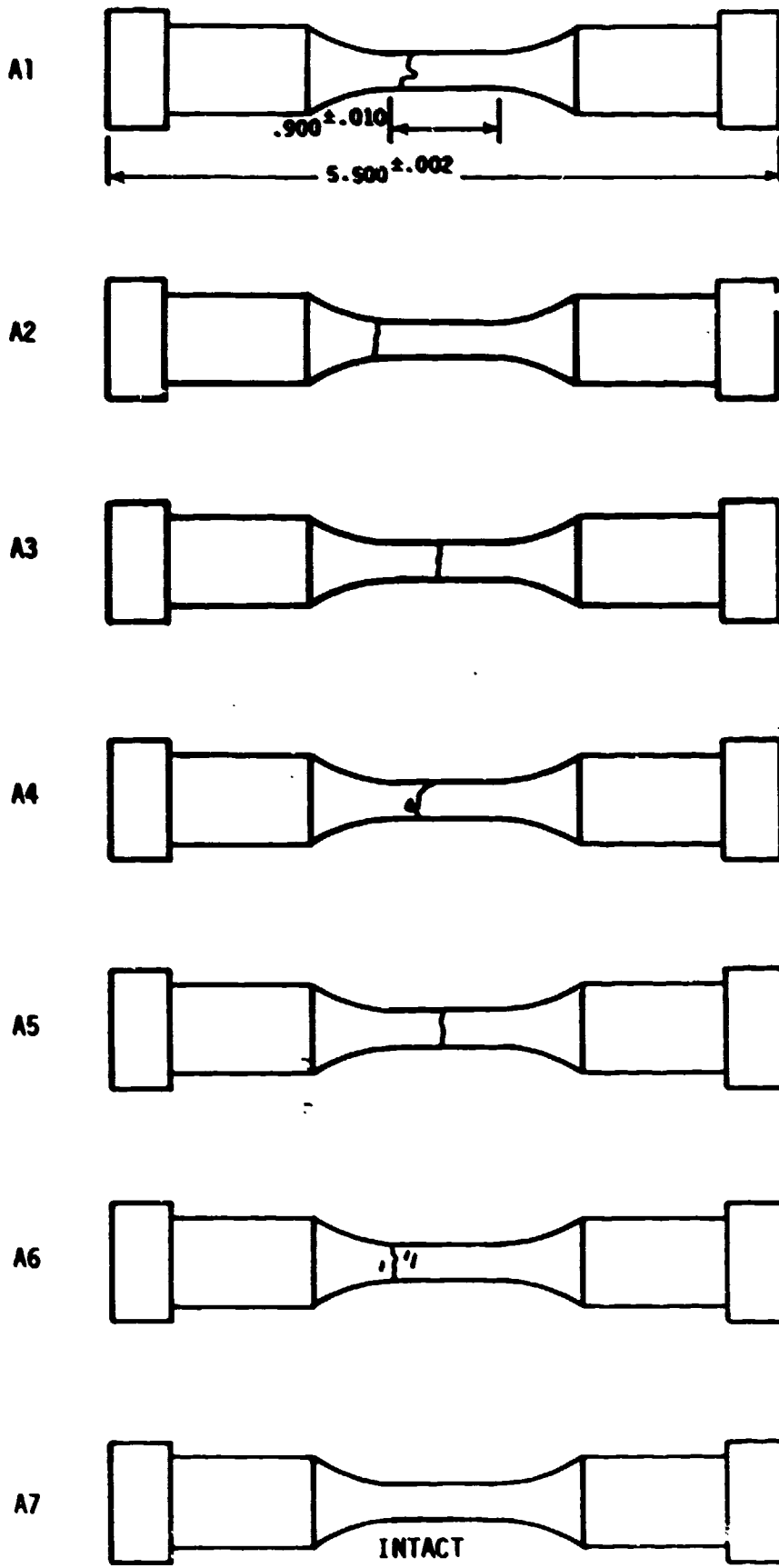
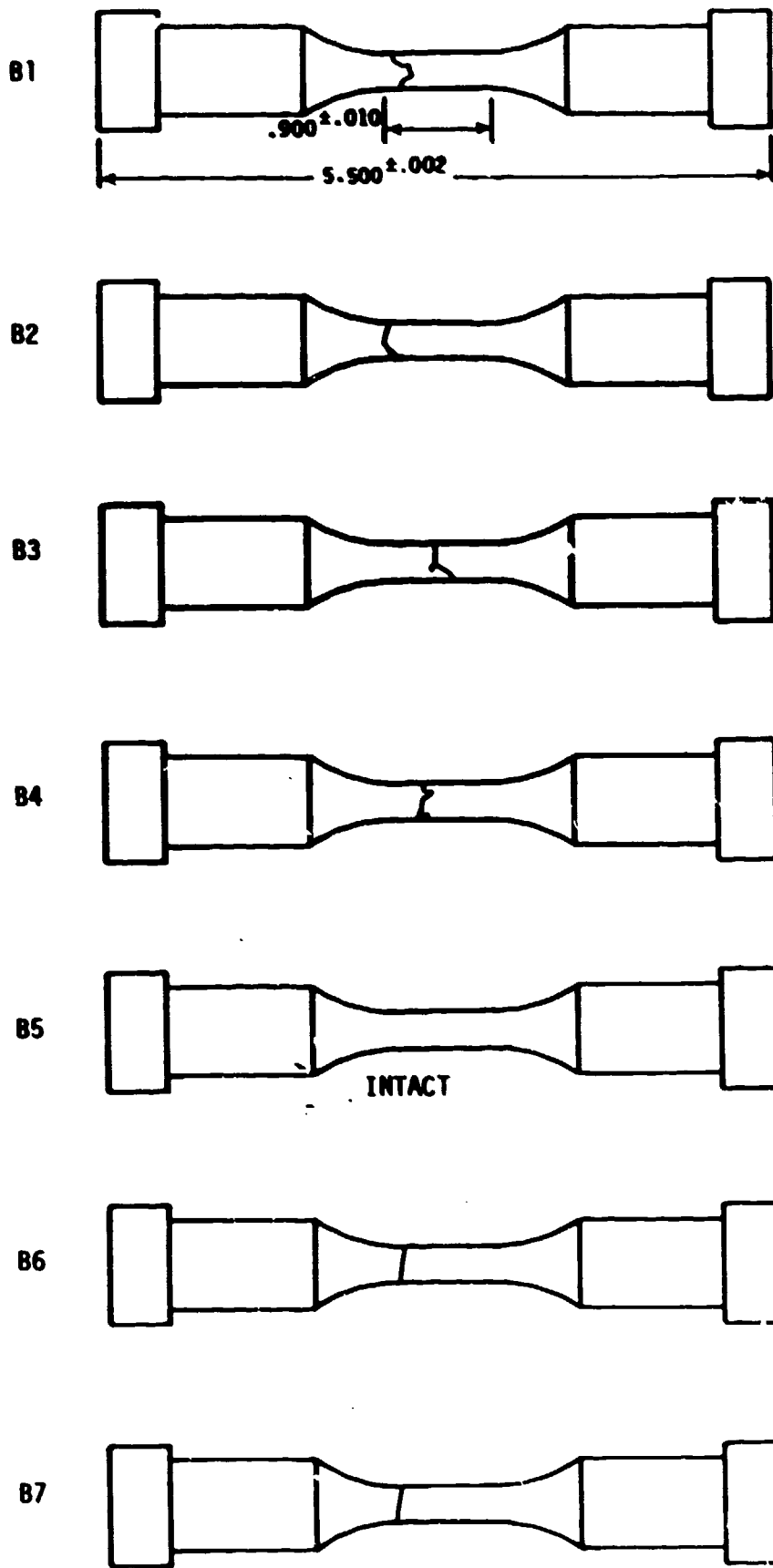


Figure 3-3
S/N Curves for Abusive Machining Samples



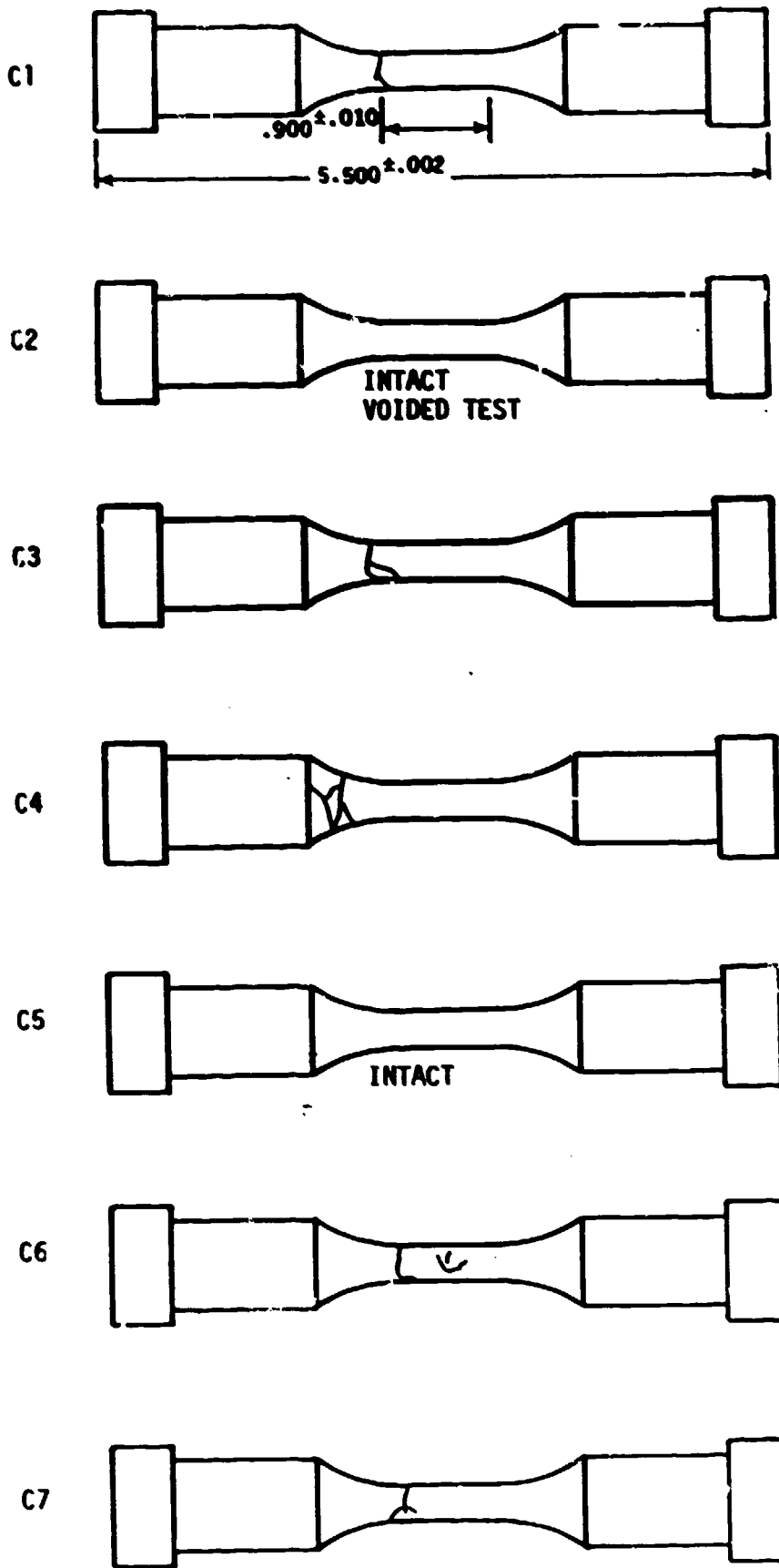
32121A18

Figure 3-38
Failure Locations for Group A



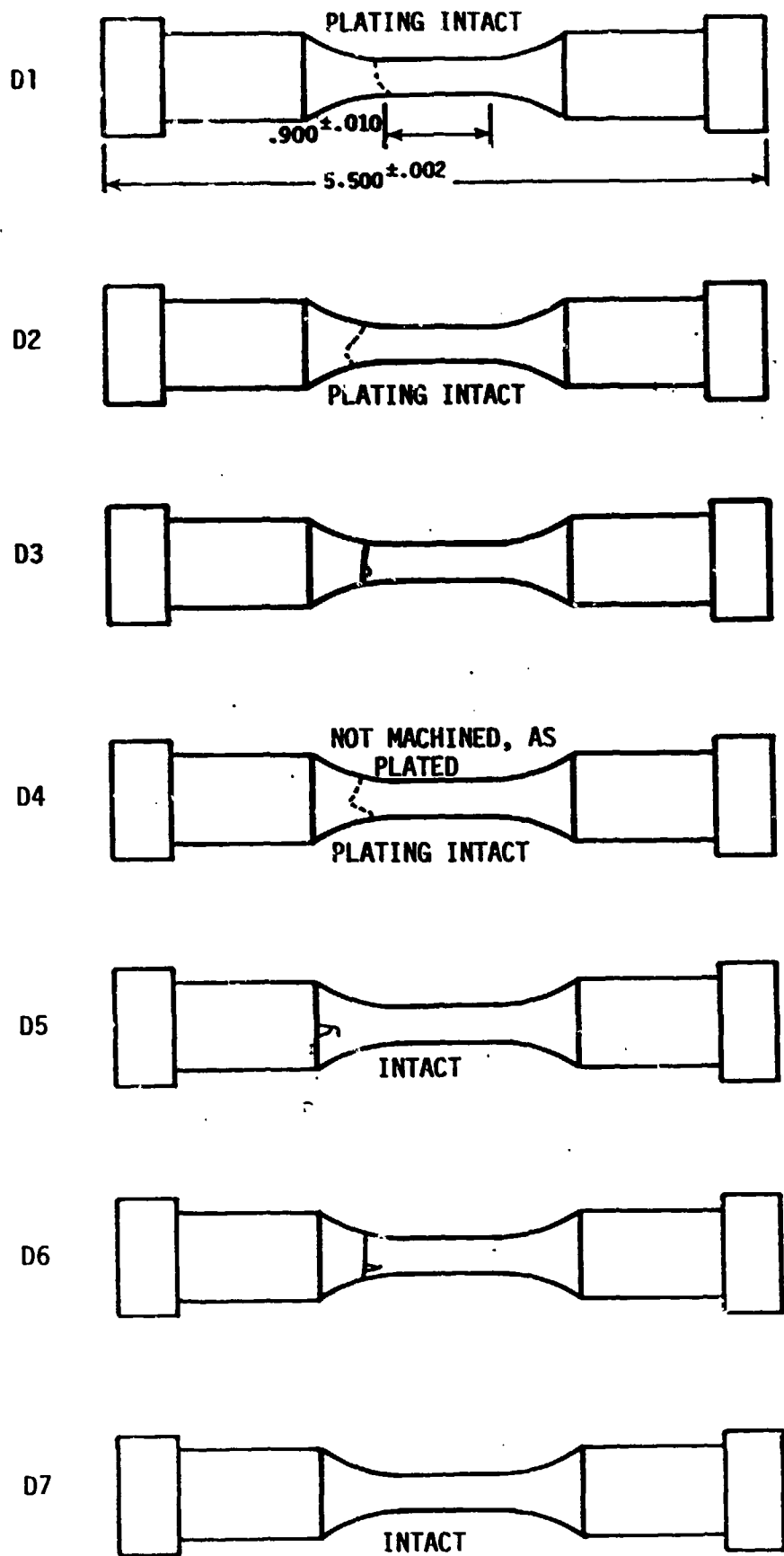
32121A18

Figure 3-39
Failure Locations for Group B



32121A18

Figure 3-40
Failure Locations for Group C



32121A18

Figure 3-41
Failure Locations for Group D

stresses. Additionally, there was no overall difference in stress levels before and after fatigue testing. All of the abusively ground and machined samples (Groups B and D) had the same stress level within one sigma error bar before and after fatigue testing. Half of the standard grinding and machining samples (Groups A and C) had the same stress levels within one sigma error bar before and after fatigue. The remaining samples all agreed within two sigma error bars except for sample C5. In this case, the pre-fatigue test stress was -53 ± 9 ksi while the post-fatigue test stress was -88 ± 4 ksi, which are the same values only within a three sigma error bar. This result indicates fatigue testing under the controlled conditions used did not affect the residual stress level.

Table 3-21 also lists the diffraction peak width at half of its maximum intensity (FWHM). The FWHM indicates the relative amount of cold working in the sample surface. As expected, the general trend showed a slightly larger FWHM (more cold working) in the samples after fatigue testing.

Fatigue testing indicated the standard and abusively machined samples had a higher fatigue resistance compared to the standard and abusively ground samples. Since unplated samples were not tested, it is not known what effects, if any, the plating had on the fatigue properties of the 4340 base material. The surface residual stress affects the fatigue performance of a component. Case histories of such effects can be found in such publications as the ASTM Special Technical Publication, STP-776, "Residual Stress Effects in Fatigue."

In general, compressive stresses improve fatigue life. This generality does depend upon the type of cyclic load encountered. The standard and abusively machined samples which had the compressive residual stresses did show an improved fatigue life compared to the ground samples.

3.5.4 Conclusions

The machined samples had an improved fatigue life compared to the ground samples. This improvement was attributed to the compressive residual stresses measured in the machined samples.

There was no apparent difference in the standard versus abusive processing based on the residual stress levels. Furthermore, residual stress levels did not change significantly as a result of fatigue testing.

4.0 TASK 3 - ANALYTICAL SYSTEMS

It had been envisioned that this task would use the measurement results from Task 2 to develop analytical tools that might be used to predict failures in components such as landing gears. This was to be accomplished by relating residual stress data to service history. Also to be included in Task 3 was any other tools that would aid in the analysis of acquired data.

As we discussed in Section 3.0, we were not successful in relating residual stress measurements to service life so that a useful predictive tool could be obtained. However, an effort was made to further the understanding of the effect of surface curvature and other focusing errors on the accuracy of residual stress measurement. An analysis of the problem was conducted and the results showed how the residual stress measurement error varied as a function of the deviation of the sample surface from the focusing circle. The results are presented in detail in Section 4.3.

4.1 THE EFFECT OF FOCUSING ERRORS AND OTHER SAMPLE MISALIGNMENTS ON THE ACCURACY OF RESIDUAL STRESS AS DETERMINED BY X-RAY DIFFRACTION

4.1.1. Introduction

A problem of concern in the Phase I work was an understanding of the effect of surface curvature on the accuracy of the residual stress measurements. This was of particular concern since many of the components studied had complex shapes and it was desired to know the state of stress near corners or in fillets. It was the objective of this part of the Phase II project to quantitatively address this problem.

The most thorough study of the effect of focusing errors on the accuracy of x-ray residual stress measurements is that of James¹ and James and Cohen.² A detailed examination of their derivation indicates that, although finite source, sample and detector sizes were considered, it was assumed that the sample was always on the focusing circle.

In the analysis presented below, the effect of deviations of the sample surface from the focusing circle will be considered. It is assumed that the x-ray source is a point source, that the detector has perfect resolution (but is not necessarily on the focusing circle), and that all vertical divergences of the beam can be ignored. Two cases are addressed: a flat sample and a curved sample of radius r_s . In both cases, it is assumed that the sample surface is coincident with the center of the diffractometer circle and that the incident beam has an angular divergence 2α .

4.1.2 Flat Sample

Under the assumptions stated above, the geometry of the diffractometer is as shown in Figure 4-1. The flat sample is tangential to the focusing circle; all other regions of the sample are not on the focusing circle. The radius of the focusing circle, r_{fC} which is by definition tangential to the sample and passes through the focal spot, is related to the radius of the goniometer circle, r_{gC} , by

-
1. M. R. James, An Examination of Experimental Techniques in X-Ray Stress Analysis, Ph.D. Thesis, Northwestern University, Evanston, Illinois (June 1977).
 2. M. R. James and J. B. Cohen, J. Appl. Crystallogr. 12, 339-445, (1979).

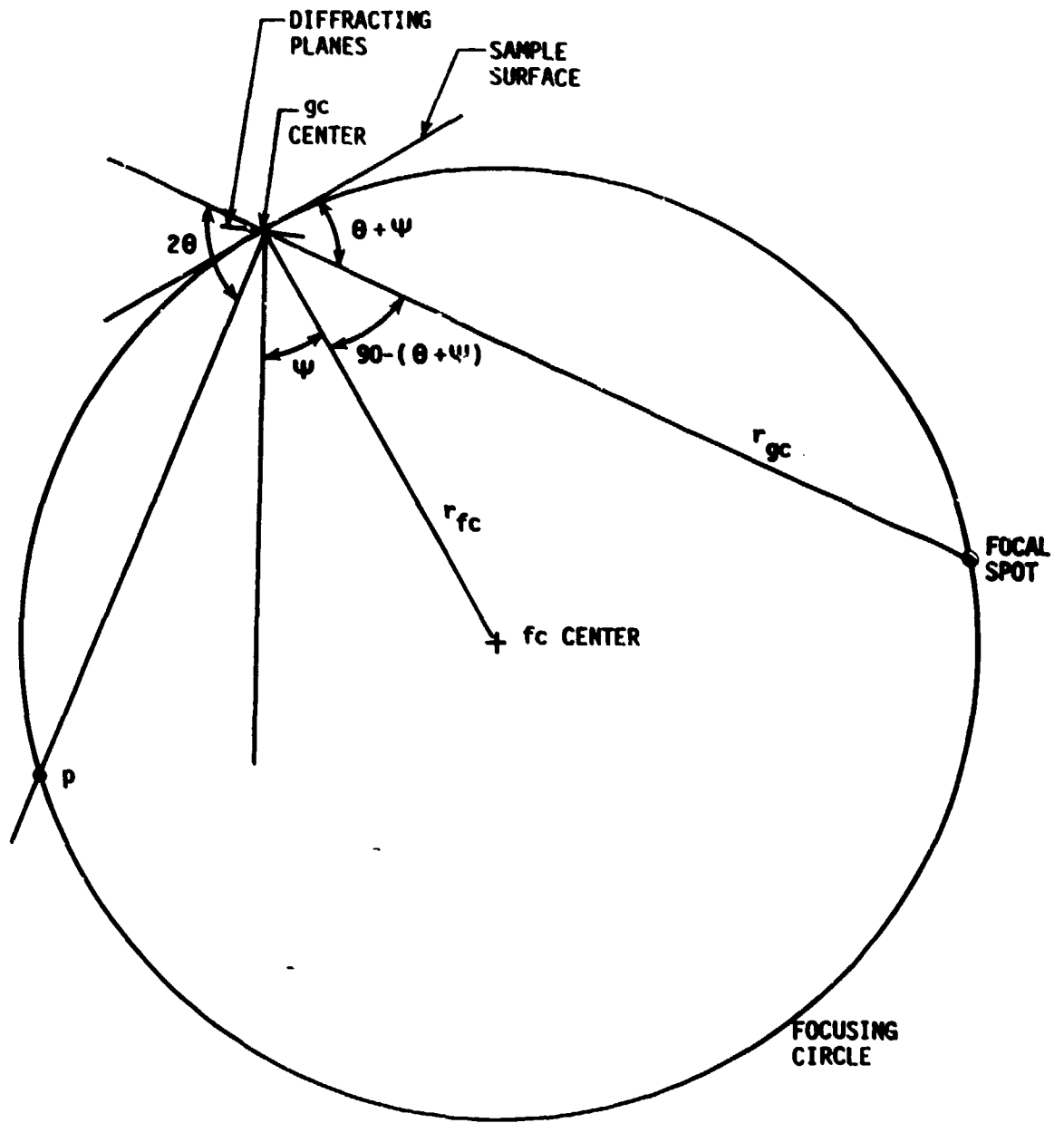


Figure 4-1
Geometry of Diffractometer

32121A12

$$r_{fc} = \frac{r_{gc}}{2 \sin(\theta + \psi)} \quad (1)$$

The goniometer circle is a circle of radius r_{gc} centered on the point where the x-ray beam strikes the sample and passes through the x-ray tube focal spot. In the symmetric θ - θ geometry, the goniometer circle also passes through the point p where the diffracted beam intersects the focusing circle. However, if the sample is tilted at any non-zero ψ angle, the focus point, which defines the best resolution of the diffracted beam, is no longer on the goniometer circle. The distance from the center of the goniometer circle to the intersection of the diffracted x-ray beam and the focusing circle, r_p , is

$$r_p = r_{gc} \frac{\sin(\theta - \psi)}{\sin(\theta + \psi)} \quad (2)$$

It is a property of the focusing circle that all rays diffracted on the focusing circle at an angle 2θ from incident rays originating at a point source will pass through the point p on the focusing circle.

Consider now a beam (Figure 4-2) which makes an angle α with respect to the central ray from the x-ray focal spot to the sample (this ray represents any one of the rays emanating from a point x-ray source through a finite collimator of angular divergence 2α). The perpendicular distance x_1 (Figure 4-2) from the intersection of this ray with the focusing circle and the sample surface is

$$x_1 = r_{fc} (1 - \cos 2\alpha) \quad (3a)$$

or, since 2α is usually a small angle,

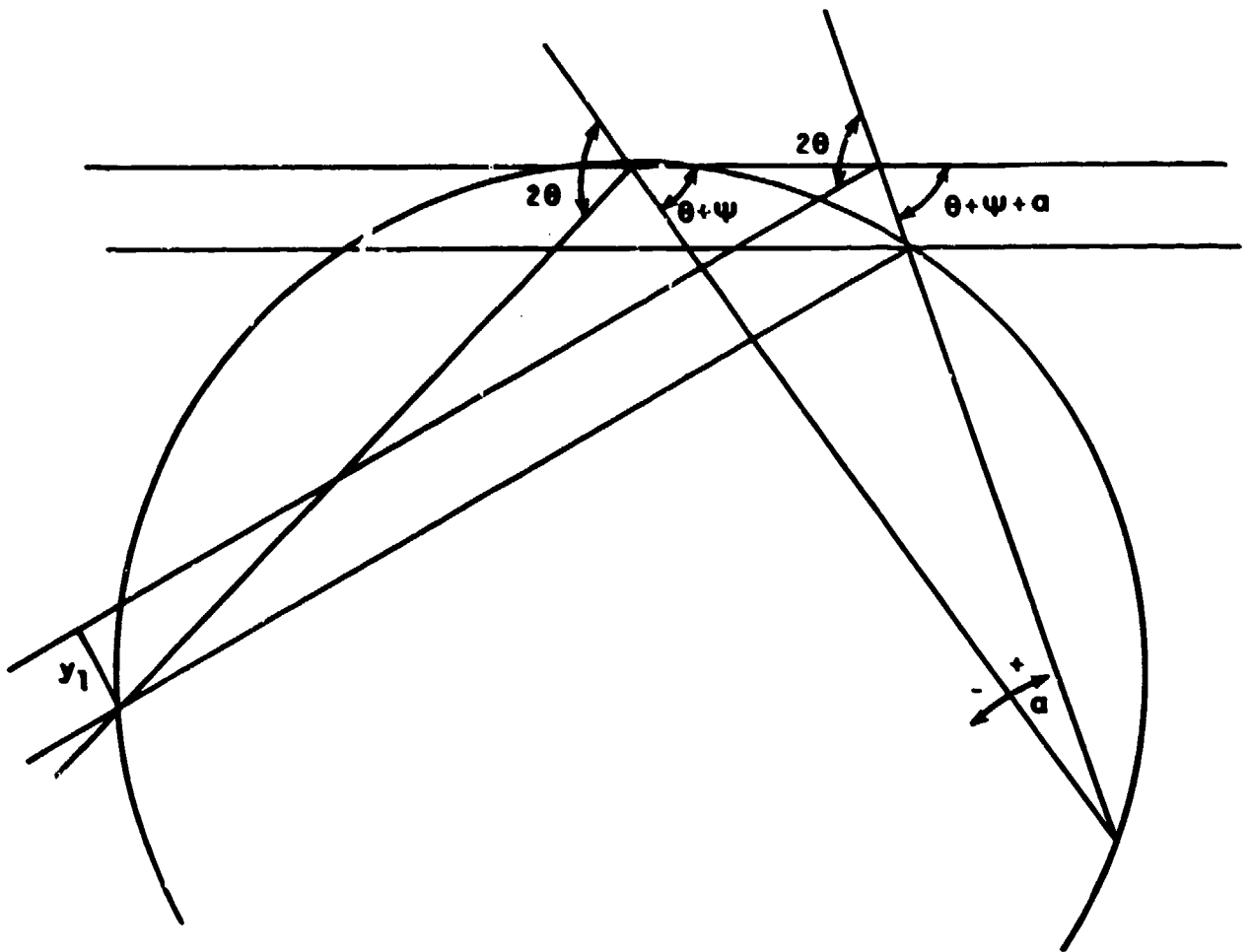
$$x_1 \approx r_{fc} \frac{(2\alpha)^2}{2!} \quad (3b)$$

Rays diffracted from a flat sample tangential to the focusing circle at the center of the goniometer circle will be parallel to but displaced from the central ray towards lower 2θ angles, by an amount y_1 (Figure 4-3), where

$$\begin{aligned} y_1 &= \frac{x_1 \sin 2\theta}{\sin (\theta + \psi + \alpha)} \\ &= \frac{r_{fc}(1 - \cos 2\alpha) \sin 2\theta}{\sin (\theta + \psi + \alpha)} \end{aligned} \quad (4)$$

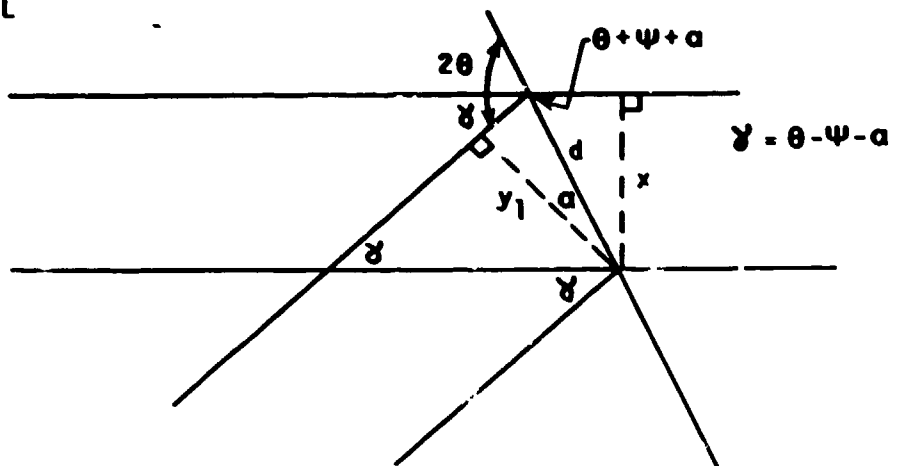
Note that although x_1 is symmetric in α , y_1 is not. This results from the small differences in direction of the diffracted rays at plus and minus α .

These results show that the central ray, which passes from the x-ray focal point through the center of the diffractometer circle and the focusing point on the focusing circle, does not move as the ψ angle is changed. However, all other rays are displaced by varying degrees to smaller 2θ values. Thus, the "mean" 2θ angle for the diffraction peak will shift with the ψ angle.



$$\gamma = (180 - 2\theta) + \theta + \psi + a = 180$$

DETAIL



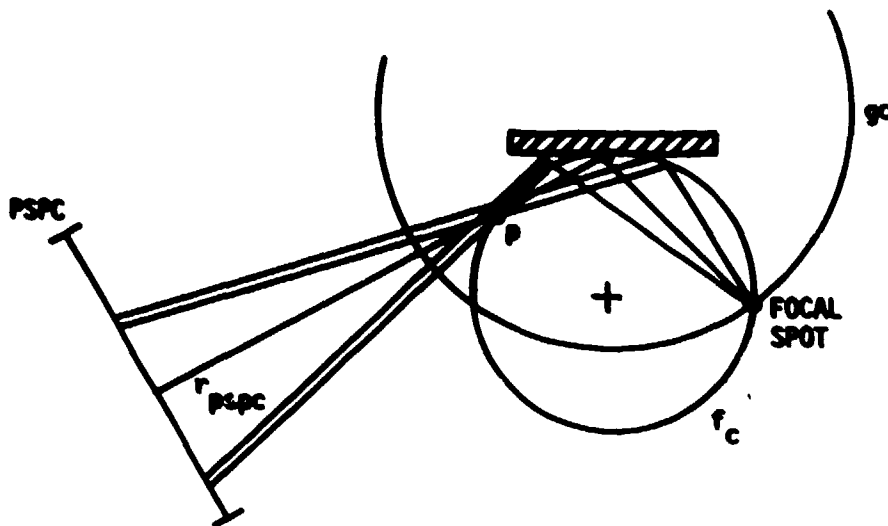
32121A14

Figure 4-3
Rays Diffracted by Amount y_1

In order to calculate the amount of peak shift rigorously, it is necessary to know the variation in intensity of the incident beam as a function of α , the mosaic spread of the sample, and the efficiency of diffraction of the sample as a function of mosaic spread. None of these parameters can be computed from first principles, and the latter two are sample-dependent, thus precluding a rigorous solution for all samples. It is known that the diffracted intensity for the two extreme rays (those making the largest possible angles with respect to the central ray) is essentially zero. The maximum intensity should occur for the central ray. Thus, following James^{1,2}, we assume the diffracted intensity at the detector is triangular in shape. As shown in Equation 4, for small angular divergences of the incident beam (small α), the shift in the end points of both sides of the beam is essentially the same. Note that this shift is also independent of the position of the detector; it need not be on the focusing circle. Under these assumptions it is straightforward to show that the shift in the centroid of the assumed triangular peak is

$$\Delta y_c = \frac{-2y_1}{3} . \quad (5)$$

If the detector is parallel to a tangent of the goniometer circle, but is at a distance r_{spec} from the center of the goniometer (Figure 4-4), then the shift in the 2θ position of the peak centroid is



32121A15

Figure 4-4
 Distance r_{pspc} from Center of Goniometer

$$\Delta 2\theta = - \frac{2 y_1}{3 r_{pspc}}$$

$$= - \frac{1 r_{gc}}{3 r_{pspc}} \frac{(1-\cos 2\alpha)\sin 2\theta}{\sin(\theta + \psi) \sin(\theta + \psi + \alpha)} \quad (5a)$$

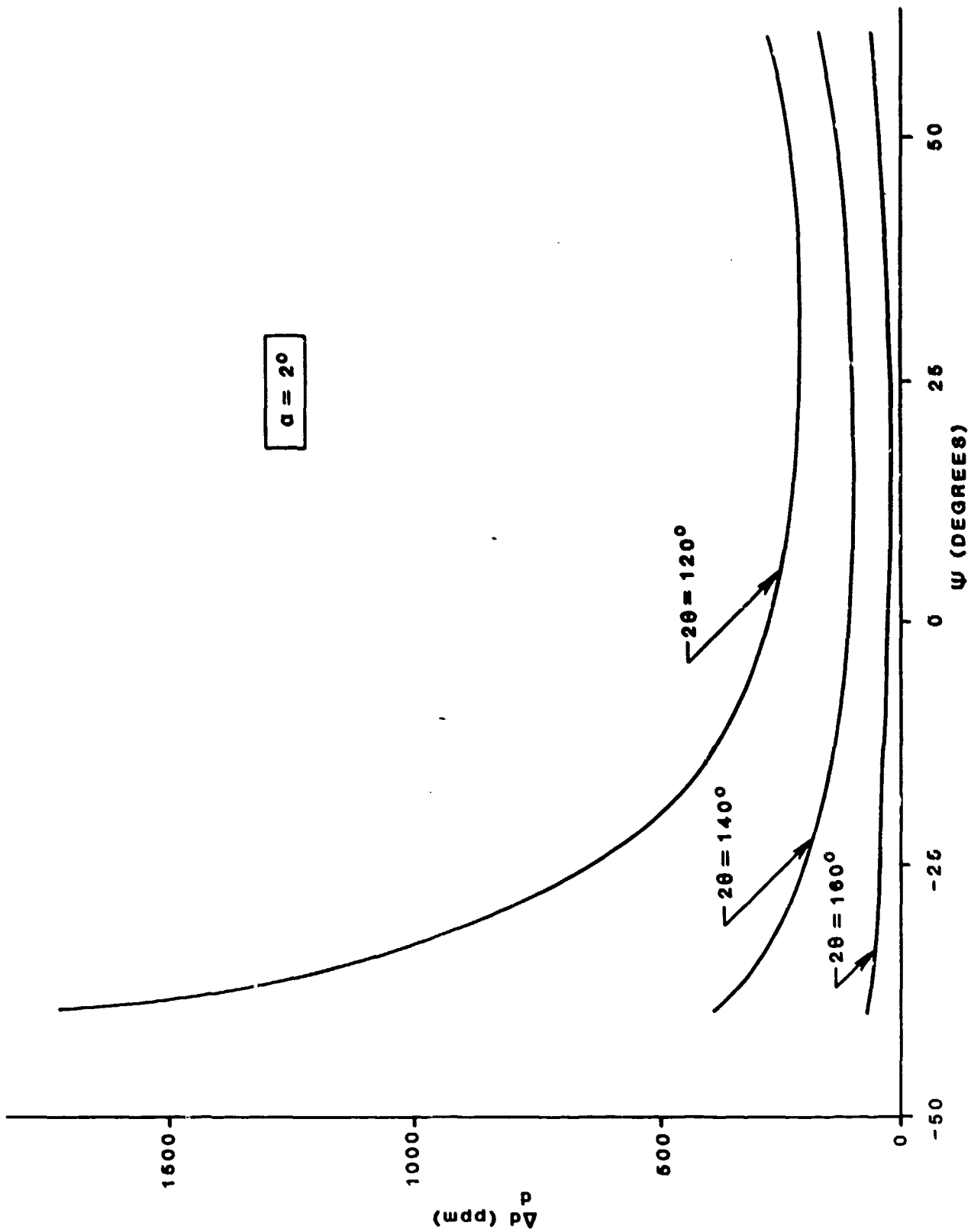
$$= - \frac{1 r_{gc}}{3 r_{pspc}} \frac{(2\alpha)^2}{2!} \frac{\sin 2\theta}{\sin^2(\theta + \psi)} \quad (5b)$$

Of course, if $\theta + \psi$ is quite small, which occurs when ψ is a large negative angle, then it may not be valid to approximate $\sin(\theta + \psi + \alpha)$ by $\sin(\theta + \psi)$ even for small slit divergences α . Under these conditions, a more rigorous calculation of the peak centroid will be required.

By differentiating Bragg's Law and substituting Equation (5), we find the error in the d-spacing which results from the finite divergence of the beam incident upon a flat sample is given by

$$\frac{\Delta d}{d} = \frac{2 r_{gc}}{3 r_{pspc}} \frac{\alpha^2 \cos^2 \theta}{\sin^2(\theta + \psi)} \quad (6)$$

This result is consistent with intuitive reasoning; it is quadratically dependent on the angular divergence of the incident beam; it decreases quadratically as θ approaches 90° ; and it increases with both increasing and decreasing ψ angle. A plot of $\Delta d/d$ for typical residual stress diffractometer conditions is shown in Figure 4-5.



32121A17

Figure 4-5
Plot of $\Delta d/d$

4.1.3 Curved Sample

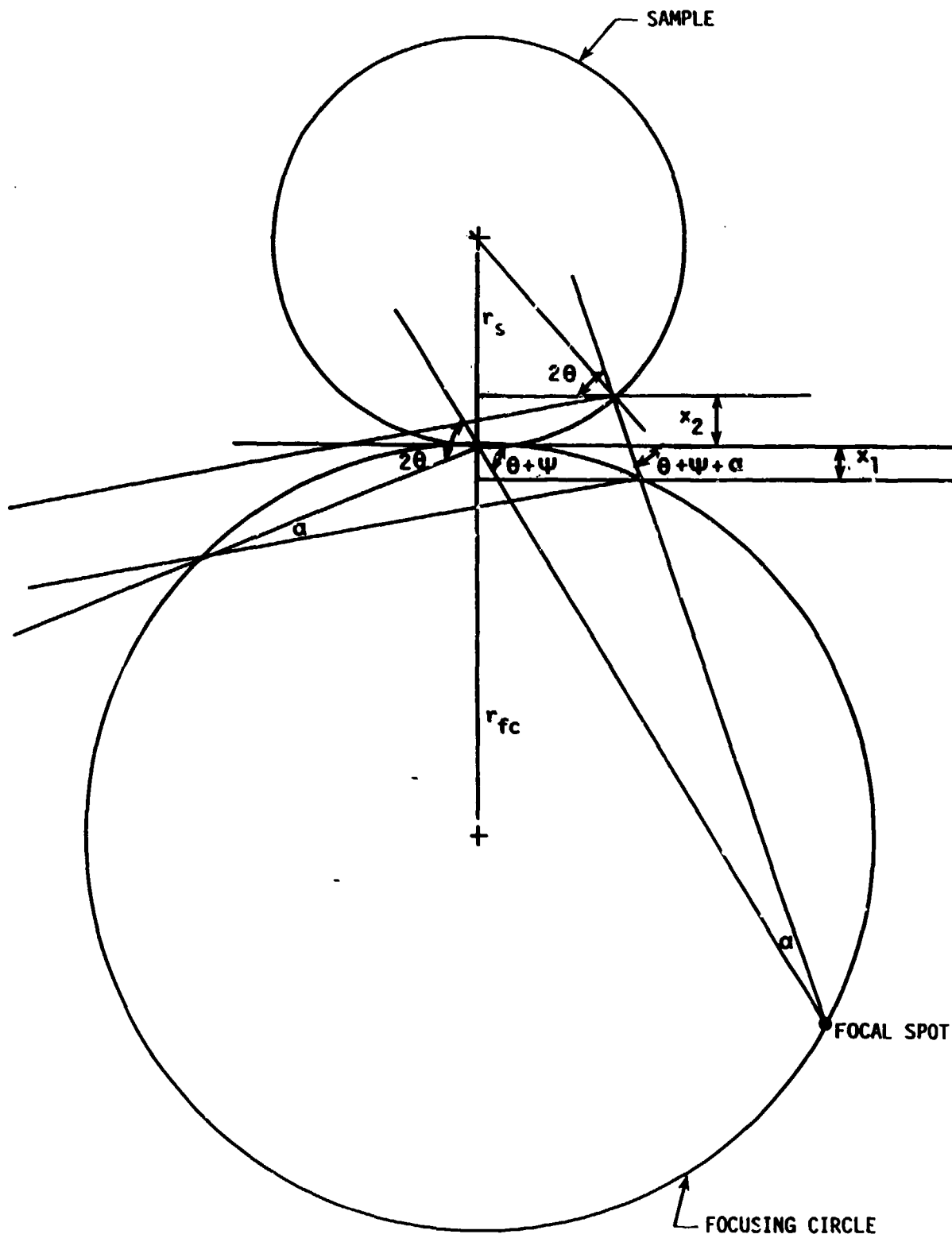
Consider now a sample with a radius curvature r_s as depicted in Figure 4-6. The sample radius, r_s , is defined to be positive if the center of curvature is on the side of the sample surface opposite the center of the focusing circle. When the two centers are on the same side of the sample surface, the radius of curvature is taken to be negative. Let us further assume that the angular divergence of the incident beam, α , is sufficiently small that, regardless of the Bragg angle, θ , both extrema beams diffract from the sample into the detector. This means that the combination of ψ , θ and r_s cannot be such that at positive α , the diffracted beam is absorbed by the sample or at negative α , the incident beam misses the sample. If such conditions exist, then a new, effective α must be computed for those rays which just meet the aforementioned conditions. It is beyond the scope of this work to perform these calculations here.

Given the above assumptions, the curved surface is an additional distance x_2 away from the focusing circle, where x_2 is given by the pair of simultaneous equations

$$x_2 = (r_{fc} \sin 2\alpha - y^2) \tan(\theta + \psi + \alpha) - x_1 \quad (7a)$$

$$\text{and } y_1^2 = 2r_s x_2 - x_2^2 \quad (7b)$$

After some tedious geometric substitutions and by making the small α approximation, it may be shown that



32121A16

Figure 4-6
Sample Curvature

$$x_2 \approx \frac{2\alpha^2 r_{gc}^2 (1-\alpha)^2}{r_s} \quad (8)$$

The additional shift in the peak position becomes

$$y_2 = \frac{x^2 \sin 2\theta}{\sin(\theta + \psi + \alpha)} \quad (9)$$

and, when combined with the previous results, shows that the total shift in the centroid of the diffraction peak is

$$\Delta 2\theta = - \frac{2 r_{gc}}{3 r_{pspc}} \frac{(\alpha)^2 \sin 2\theta}{\sin^2(\theta + \psi)} \left[1 + \frac{r_{gc}(1-\alpha)^2}{2r_s \sin(\theta + \psi)} \right] \quad (10)$$

The resulting error in the d-spacing is then

$$\frac{\Delta d}{d} = \frac{2}{3} \alpha^2 \frac{r_{gc}}{r_{pspc}} \frac{\cos^2 \theta}{\sin^2(\theta + \psi)} \left[1 + \frac{r_{gc}(1-\alpha)^2}{2r_s \sin(\theta + \psi)} \right] \quad (11)$$

Equations (8), (10) and (11) show that the shift in peak position and, hence the resulting shift in the d-spacing involve an additional term which is inversely proportional to the radius of curvature of the sample. Since most diffractometers have fairly large radii ($r_{gc} \approx 200\text{mm}$ is typical), the second term can become, for many real-world samples, the dominant term. In these cases,

$$\frac{\Delta d}{d} = \frac{2}{3} \alpha^2 (1-\alpha)^2 \frac{r_{gc}^2}{r_s r_{pspc}} \frac{\cos^2 \theta}{\sin^3(\theta + \psi)} \quad (12)$$

Equation (12) is valid for both convex ($r_s > 0$) and concave ($r_s < 0$) samples and shows that the peak shift is to a higher Bragg angle for concave samples.

As a test of the correctness of Equation (11) consider the situation where $r_s=r_{fc}$. Under these conditions, the peak shift at the focusing circle should be zero. Substitution of $r_s=r_{fc}$ and Equation (1) in Equation (11) shows that the last term of (11), in square brackets, reduces to 2α and that

$$\frac{\Delta d}{d} = \frac{(2\alpha)^3}{3} \frac{r_{fc} \cos^2 \theta}{r_{pspc}} \quad (13)$$

Thus it is seen that, rather than being identically zero, the predicted error varies as $(2\alpha)^3$. Since, in the solution of Equation (7) only linear terms in α were retained, it is to be expected that an error involving higher order powers of α will remain. It is comforting that the residual error expressed by Equation (13) depends on $(2\alpha)^3$. Thus, it is concluded that, within the approximations made, Equation (11) is a reasonable representation of the parametric dependencies of $\Delta d/d$ on the various instrumental and sample variables.

4.1.4 Conclusions

The analysis presented here shows that deviations of the sample surface from the focusing circle can lead to errors in the measured location of the centroid of the Bragg peak. These deviations depend on the ψ -angle, and thus will lead to errors in the determination of the residual stress. The magnitude of the effect varies quadratically with the angular divergence of the incident beams, increases as the Bragg angle deviates from perfect back reflection and varies inversely as the radius of curvature for curved samples. Simple calculations show that these effects can account for the deviations from zero stress which are commonly observed in the measurement of stress-free samples.

4.2 PRACTICAL APPLICATIONS OF THE ANALYTICAL STUDY OF FOCUSING ERRORS

The analytical study of focusing errors has been supported by several of the measurements performed in the Task 2 work. Put in practical terms, the focusing errors are a major factor in using Cr K β radiation instead of Cr K α radiation for nickel-plating. The Cr K β radiation diffracts from nickel at a higher back-reflection angle, thus reducing the error due to deviation from the focusing circle. Should the use of Cr K α radiation on nickel be desired, this can be easily accomplished. The focusing errors are greater in the $-\psi$ direction (deviation from the focusing circle is greater than in the $+\psi$ direction) and minimal in the $+\psi$ direction even at the lower back-reflection angle ($\sim 135^\circ 20'$). Nickel stress measurements using Cr K α radiation should be performed with $+\psi$ angles only. If possible, the measurement should be repeated after rotating the sample 180° . This procedure results in data for positive and negative ψ angles and is necessary to check if shear stresses exist.

Comparison of the bearing results in Phase I and Phase II showed a $\sin^2\psi$ split that resulted from the bearing geometry. The $\sin^2\psi$ split was attributed to the use of a large collimator relative to the curvature of the bearing race and not shear stresses. A smaller collimator (2 mm diameter) reduced the effects of the geometric error as predicted by the focusing circle error analysis.

A short experiment was performed on stress-free powders after focusing errors were analyzed. The conclusion of the focusing circle study stated that deviations from the focusing circle produced errors in the stresses measured on stress-free powders. It should be noted that the majority of stress-free

analyses have given stresses between ± 4 ksi, and over half of these are between ± 2 ksi. An error of ± 2 ksi is acceptable and to be expected because of factors other than focusing circle error. Stresses outside the ± 2 ksi have been related to setup errors, bad sample preparation and preferred orientation of the grains. A measurement was made on a stress-free powder with a 4 mm diameter collimator. A second measurement was made without changing any parameters except the collimator. When a 1 mm diameter collimator was used, the stress value actually increased instead of decreasing as predicted by the focusing circle analysis. Considering these facts, it was concluded that the error seen in stress-free powders when it exceeds the acceptable limit of ± 2 ksi is due to factors other than focusing circle error.

Focusing circle errors can account for some of the phenomena seen during the Navy SBIR Phase I program. This error explains the results seen for nickel-plating and bearings. Errors in stress-free powders due to deviation from the focusing circle are probably minimal.

5.0 TASK 4 - COMMUNICATIONS LINK

5.1 OBJECTIVES

The principal objective of this task was to develop communication links between stress analysis instruments over the telephone to transmit measurement results from one facility to another for analysis and interpretation. This would permit depot facilities to consult with each other whenever the need occurred.

5.2 RESULTS

Several software packages were evaluated. The selected system was the communications package included in the RT-11 software that TEC provides with each stress analysis instrument. The use of this software, two programs written by TEC and a Hayes compatible modem enables transfer of files over standard phone lines. The choice of modem depends on the availability of a serial port in the computer. On earlier systems, which used a parallel printer, there is a spare serial port and the Hayes Smartmodem is recommended. On the prototype and later systems, which use a serial printer, there is no spare serial port; a commercially available Q-bus modem on a printed circuit board is used. The MICROTALK Q-bus modem from Technical Magic, Inc. was chosen for this application.

5.3 DISCUSSION

During the program, a comparison of two software packages was made, RT-11 DECnet and Polygon Associates, Poly-Com. The cost of the RT-11 DECnet is \$2,000 versus \$600 for the Poly-Com. RT-11 DECnet did not offer enough advantages to justify the higher price so the Poly-Com was purchased.

During the implementation of the Poly-Com system, documentation was discovered in the RT-11 System Release Notes which indicated that the standard RT-11 software included a simple communication package at no extra cost. This package proved to be the most economical solution once two TEC programs were written to augment the RT-11 package. The system is, however, limited to communicating with computers running the RT-11 operating system. Since this is the operating system used on all TEC stress analysis systems, this is not a limitation.

Because the Poly-Com had been obtained, it was also implemented because, unlike the RT-11 package, it can provide communication to a wide variety of computers such as IBM-PCs running the PC-DOS operating systems and DEC VAX machines running VMS as well as DEC PDP-11 machines running RT-11, RSTS and RSX-11M operating systems.

In comparison, both the DEC RT-11 and Poly-Com packages are cumbersome in the host mode. Both require the RT-11 console terminal port to be connected directly to the modem for the system to work. This creates a conflict while attempting to make the initial phone connection as well as restricting the terminal baud rate to 1200. This problem is solved by the use of two TEC written programs, MODEM and TERM, that transfer the console terminal port from the VT-640 to the modem port. The program called MODEM, transfers RT-11 terminal control from the VT-640 serial port to the modem serial port. Conversely, the program called TERM transfers control from the modem port back to the VT-640 port.

Use of the software in the local mode is similar and relatively straightforward for both packages. The RT-11 package compacts data areas containing zeros to reduce the number of bytes of data transmitted over the link. Therefore, a significant amount of transmit time may be saved on files having large blocks of zeros. A 59-block image required 5 minutes and 46 seconds to transfer. This corresponds to approximately 6 seconds per block of data. Consequently, a 20-block spectra file could be transferred in approximately 2 minutes.

The Poly-Com package required 10 minutes and 3 seconds to transfer the same 59-block image. This corresponds to approximately 10 seconds per block of data. Consequently, a 20 block spectra file would require approximately 3 minutes and 20 seconds.

Polygon provides a well written manual which thoroughly explains the software but does not explicitly discuss the host system hardware configuration. The RT-11 communication package operation is covered briefly in the System Release Notes for RT-11. The explanation of use is adequate, however, prior knowledge of RT-11 is a must to understand the documentation. Like the Poly-Com documentation, no explanation of the required hardware configuration is included.

The public telephone network provides the communication data medium. Access to the network requires only a desk telephone using standard modular connectors. Interface into the phone system is accomplished via a commercially available modem (MODulator DEModulator). The modem, in turn, is connected to the computer system via a RS-323-C cable to a serial port on the stress analyzer computer system. Refer to Figure 5-1. The communication software system

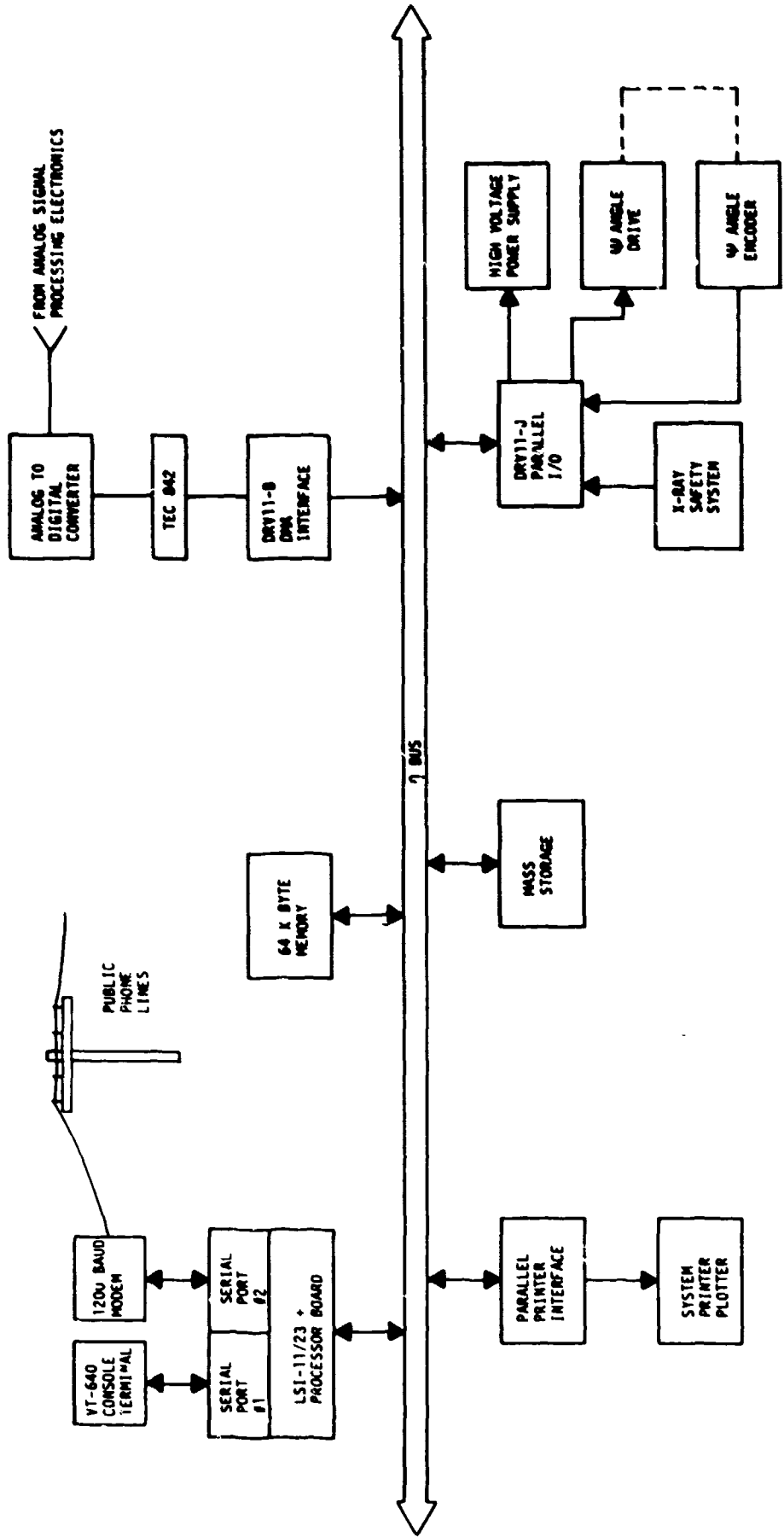


Figure 5-1
SBR STRESS ANALYZER HARDWARE CONFIGURATION

32121001

controls the transfer of data between systems. The Hayes modem was chosen since it is a tried and proven modem that is considered an industry standard.

During a transfer operation, one system is designated as the host system while the other is the local system. The "host" system is essentially a slave to the "local" system. Communication to the host system is accomplished through its console terminal port.

The "local" system essentially takes over the operational control of the "host" system. All operations are performed from the "local" system. Either system can be a local or host but not both. Given two systems referred to as System A located in Pensacola, Florida and System B located in Norfolk, Virginia. Should System A need data from System B, System A could request this data with all control operations occurring at the System A terminal. In this example, system A is the "local" system while system B is the "host" or slave system. On the other hand, if System B calls System A to transfer data from B to A, then System B would be the "local" system while System A is the "host." Programs are provided to obtain logical connection of the console terminal to the modem's serial port. This provides the mechanism for modem control as well as remote control of one stress analyzer from the terminal of another stress analyzer. This provides the capability to accomplish a number of interesting tasks such as the remote reviewing of data and the potential for trouble shooting a remote system. Probably one of the most useful features will be the ability to transfer raw spectra files from a remote site to a local site for local inspection or special analysis. If the Poly-Com system is used, a data base of files could be developed and stored on a mainframe system.

Both the RT-11 and Poly-Com systems were installed and tested. An operating guide was written for each system and checked out by several operators.

Both the Poly-Com and the RT-11 distributed communication package were installed and tested on stress analyzer systems at Technology for Energy Corporation facilities. Poly-Com is a viable package where communications must be accomplished between an RT-11-based machine and either a non-DEC system or a VAX. However, the performance and cost penalty for communications between two RT-11-based systems via Poly-Com is excessive.

The DEC RT-11 communications package, although a bit more complex from the user's standpoint than Poly-Com, provides fast, reliable communications between two RT-11-based stress analysis systems. This system would have a distinct advantage for RT-11 to RT-11 system communication.

Both communications packages may co-exist on the same operating system disk since the program and driver names are unique. Thus, the DEC RT-11 communication software system may be used where speed is needed and the Poly-Com software used when communication must be accomplished with a non-DEC system or a VAX.

5.4 COMMUNICATION PACKAGE OPERATING GUIDE

5.4.1 DEC RT-11 Communications Package

Refer to the DEC "System Release Notes" section 12 reference manual for a more detailed explanation of file transfer software. This sequence entails a minimal step-by-step technique for accomplishing simple file transfers.

1. Establish phone communication with the other end by dialing in the normal manner. The exact data transfer procedures and other items may be discussed with the person at the other end at this time.
2. Determine which system will be "Host" and which will be the "Local" system. Remember that the "Local" system has total control over the "Host" system, but data files may be transferred either to or from the "Host" system to the "Local" system.
3. On both systems, make sure the following RT-11 programs are on the system disk:

IL.SYS	- Serial device handler for the modem port
VTCOM.REL	- Virtual terminal program
TRANSF.SAV	- Transfer program
MODEN.SAV	- VT-640 to modem port transfer program
TERM.SAV	- Modem port to VT-640 transfer program
VTCOM.COM	- VTCOM.REL initiation command file

4. On both the "Host" and "Local" systems:
 - a. Turn on the modem power switch - located on the rear of the modem.
 - b. Initiate the virtual terminal program to allow control of the modem and establish data communications.

Type: @VTCOM <carriage return> - Initiate VTCOM program

^F (press and hold control key then press the "F" key)

- Directs terminal output to VTCOM

At this point on both systems, the terminal is logically connected directly to the modem. Therefore the modem may be controlled from the terminal.

5. This step requires close coordination to prevent the modem timing out before the data connection is made. People on both ends are still in voice communication with each other at this point. Both of these operations should be done concurrently.

On the "Host" system, type:

ata <carriage return> - Commands modem to answer phone

On the "Local" system, type:

atd <carriage return> - Commands modem to data mode

Operators at both systems should hear the carrier for a brief period while the modems establish the data link. Both terminals should then display "CONNECT" indicating their respective modem has established a connection. The phone on both ends will now sound dead since the modems have taken the line.

6. On the "Host" system, stop the virtual terminal program, and remove the virtual terminal and driver from memory by typing:

^P (press and hold control key then press the "P" key)

- Causes VTCOM to enter command mode

VTCOM will prompt with: TT::VTCOM>

EXIT <carriage return> - VTCOM exits and RT-11 prompts with

" B> "

UNLOAD XL,F <carriage return> - Unload driver and VTCOM

7. On the "Host" system, execute the MODEM program to transfer RT-11 console terminal control to the modem port by typing:

MODEM <carriage return>

The VT-640 on the "Host" system will be dead from this point on until control is restored by the "Local" system. One or two dots should appear on the "Local" terminal which indicate the "Local" terminal is logically connected to the "Host" system.

Commands may now be entered on the "Local" terminal to control the "Host" system exactly as if you were sitting at the console terminal at the "Host" system.

8. To transfer a file from the "Host" system to the "Local" system, use the following command construction.

(to Local) (from Host)

```
TRANSF < output file >/T=< input file >/W
```

To transfer a file from the "Local" system to the "Host" system, use the following command construction.

(to Host) (from Local)

```
TRANSF < output file >=< input file >/W/T
```

The /W causes TRANSF to output data transfer statistics while the /T switch indicates which file is on the "Local" system. Note that the direction of transfer is always from the <input> side of the "=" to the <output> side.

Examples:

To copy file SAMPL1.TXT from the "Host" system to the "Local" system use:

```
TRANSF SAMPL1.TXT/T=SAMPL1.TXT/W
```

To copy file SAMPL1.TXT from the "Local" system to the "Host" system use:

```
TRANSF SAMPL1.TXT=SAMPL1.TXT/T/W
```

9. On the "Local" system, after all files are transferred, and the link is to be terminated, transfer "Host" terminal control to the "Host" VT-640 by typing:

TERM <carriage return>

A dot will appear on the "Host" VT-640 - indicating RT-11 terminal control.

10. On the "Local system, disconnect the modem from the phone line by typing:

+++ <no carriage return> - Send escape code to modem

The modem responds with:

OK

ath <carriage return> - Command modem to hang up

The "Host" system modem will detect loss of carrier and hang up by itself. If both phones have been left off the hook, they will again be active - allowing voice communications again.

11. On the "Local system, stop the virtual terminal program, and remove the virtual terminal and driver from memory by typing:

^P (press and hold control key then press the "P" key)

- Causes VTCOM to enter command mode

VTCOM will prompt with: TT::VTCOM>

EXIT <carriage return> - VTCOM exits and RT-11 prompts with

" B> ".

UNLOAD XL,F <carriage return> - Unload driver and VTCOM